# 論文 / 著書情報
# Article / Book Information

| | |
|---|---|
| 題目(和文) | |
| Title(English) | Study on structure-simplified resonant-tunneling-diode terahertz oscillators |
| 著者(和文) | MAIVAN TA |
| Author(English) | Van Ta Mai |
| 出典(和文) | 学位:博士(工学),<br>学位授与機関:東京工業大学,<br>報告番号:甲第12381号,<br>授与年月日:2023年3月26日,<br>学位の種別:課程博士,<br>審査員:鈴木 左文,小山 二三夫,宮本 恭幸,若林 整,渡辺 正裕,前澤 宏一 |
| Citation(English) | Degree:Doctor (Engineering),<br>Conferring organization: Tokyo Institute of Technology,<br>Report number:甲第12381号,<br>Conferred date:2023/3/26,<br>Degree Type:Course doctor,<br>Examiner:,,,,, |
| 学位種別(和文) | 博士論文 |
| Type(English) | Doctoral Thesis |

Tokyo Institute of Technology
Doctor Thesis

# Study on structure-simplified resonant-tunneling-diode terahertz oscillators.

February 2023

Directed by Professor Safumi Suzuki

Department of Electrical and Electronic Engineering

Mai Van Ta

# Contents

# Chapter 1
# Introduction

# 1.1 Introduction

Terahertz (THz) waves lie between the millimeter wave and infrared light having a frequency range from 100 GHz up to 10 THz. Although millimeter waves and infrared light were well developed and commercialized for a number of applications. THz frequency range is still undeveloped, therefore that frequency range is sometimes called the THz gap. However, THz waves have several uniquely attractive advantages including extremely wide available bandwidth, the ability to penetrate through non-conducting materials and exhibiting fingerprints to numerous organic cells and substances. Originating from those features, THz waves are expected to be used for promising applications such as ultra-high data rate wireless communications, high-resolution imaging, as well as spectroscopy and sensing.

In this work, resonant tunneling diode (RTD) oscillators, which have a simplified structure, are studied. Those RTD oscillators have the unique advantage of a simple fabrication process and short fabrication time compared to that of reported common RTD oscillators. Based on the structure-simplified RTD oscillator, array configurations were proposed for coherent power combination using a new coupling method called “resistor-coupled” one.

This chapter introduces THz frequency range and their promising applications followed by discussing possible candidates for THz sources. The advantages of RTD THz oscillators are pointed out. Next, the motivations of my study are presented followed by specifying the purpose of my study. Then, the structure of my thesis is given at the end of this chapter.

## 1.2 Terahertz frequency range

The THz frequency range refers to electromagnetic waves having frequency from approximately 100 GHz to 10 THz [1.1-1.6]. Such frequency range corresponds to wavelength of from 3 mm to 30 μm. In the radio electromagnetic spectrum, THz waves lie between millimeter waves and infrared light. Because most THz waves have a frequency below 1 mm, they sometimes are called submillimeter-wave. While the upper edge of the THz frequency band is also called far-infrared.

Another term is also applied for THz waves is T-ray. While the X-ray has a photon energy level from 100 eV to several tens keV, the T-ray has a photon energy level merely from 0.4 to 40 meV [1.7]. Such low photon energy level does not cause ionization so THz waves are safe for humans. Moreover, low photon energy level makes them useful for non-destructive and non-invasive inspection applications.

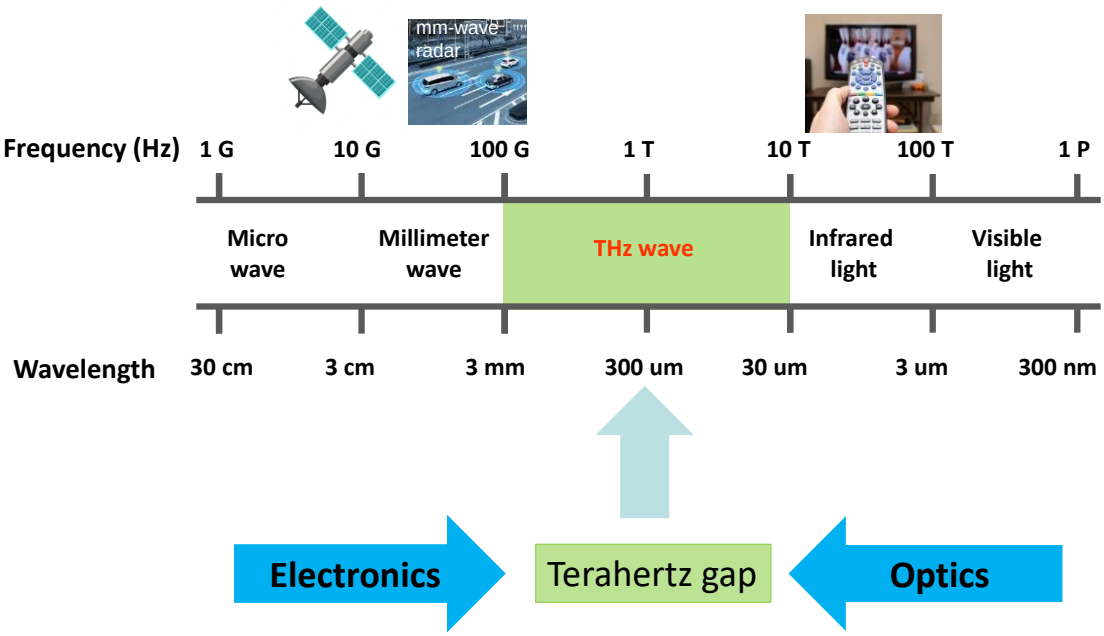


Fig. 1.2.1 Terahertz frequency range.

Another unique feature of THz waves is their interaction with molecules [1.8, 1.9]. THz electric fields strongly interact with polar molecules such as $H_2O_2$, $CO_2$, $O_2$, and $N_2$. While they do not have interaction with non-polar materials such as papers, clothes, plastic, etc., hence THz waves can penetrate through such non-polar materials. Strong interaction with polar molecules, especially water molecules, on the one hand, causes strong atmospheric attenuation of THz waves during free space propagation. The frequency dependence of atmospheric attenuation of THz waves is given in Fig. 1.2.2 based on data released by the National Institute of Information and Communications (NICT, Japan). Due to strong atmospheric attenuation, THz waves are suitable for short-range to medium-range applications [1.10-1.11]. However, on the other hand, that feature is a useful one of THz waves that can be used for spectroscopy applications owing to fingers prints exhibited in the absorption spectra of inspected samples when illuminated by THz sources [1.12-1.13].

The ability of THz waves to penetrate through various non-conducting materials such as papers, clothes, plastics, etc., paves the way for THz imaging [1.14-1.16]. Because of the shorter wavelength compared to that of microwave and millimeter waves, THz waves offer a higher spatial resolution. Hence, THz imaging is expected to deliver a resolution higher than that of millimeter waves. As mentioned above, owing to low photon energy, THz waves are safe for human use, therefore, THz imaging finds to be useful for various body-check-related applications such as medical diagnostics and security body scanning.

Another promising feature of THz waves is the ability to provide extremely large available bandwidth while being used as a carrier wave for wireless communications applications. Large bandwidth of several tens GHz is an excellent feature to achieve ultrahigh data rate transmission of several tens to hundreds Gbps [1.17-1.18]. Moving

toward higher carrier frequencies seems an unavoidable approach to achieving high data rate wireless communications. This is because the approach to increasing the data rate by using high-order modulation techniques, which are usually employed in microwave and millimeter wave bands, is limited by very high SNR requirements [1.19].

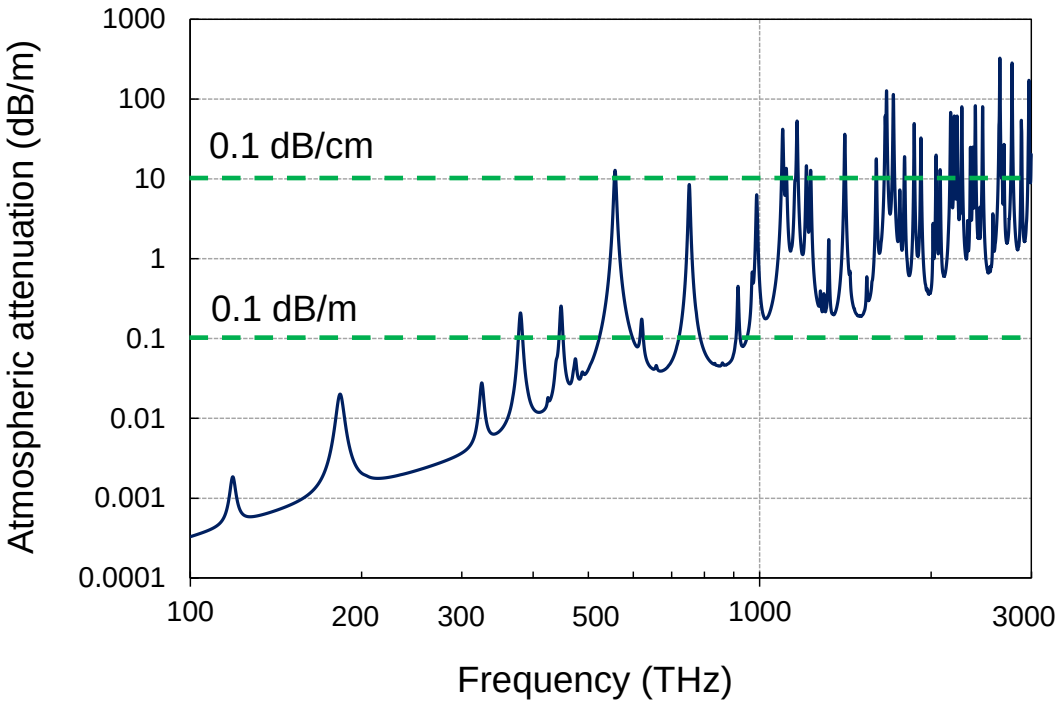


Fig. 1.2.2 Atmospheric loss in the THz frequency range.

Typical promising applications of THz waves will be introduced in the next section of this chapter.

# 1.3 Promising terahertz applications

Originating from attractive characteristics of THz waves, various promising applications of THz waves have been investigated including ultra-high data rate wireless communications, high-resolution THz imaging, spectroscopy, and sensing.

■ **Terahertz high data rate wireless communications**

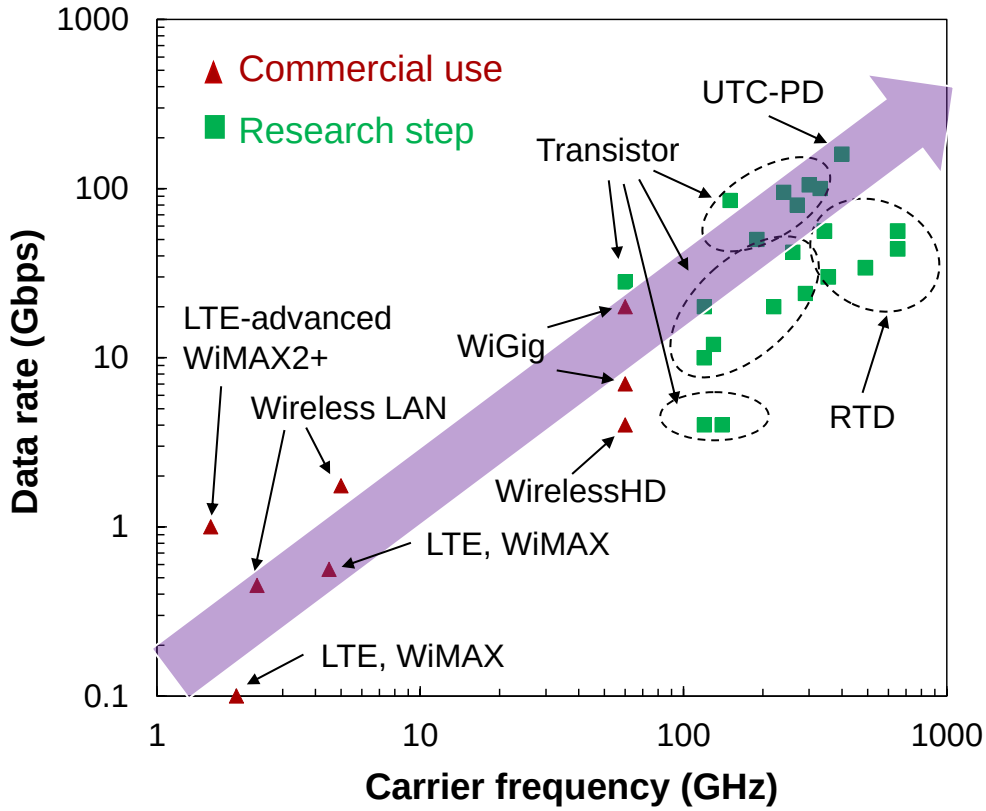


Fig. 1.3.1 Data rate vs carrier frequency.

From the Shannon formula, it is possible to achieve high data rate capacity by using a wide bandwidth

$$C = Blog_2\left(1 + \frac{S}{N}\right) \tag{1.1}$$

where $C$ is the theoretical highest data rate of the wireless communications channel, $B$ is the bandwidth of the channel, and $S/N$ is the signal-to-noise ratio at the receiver, respectively. A wide channel bandwidth could be achieved with using high carrier frequencies. Therefore, there is a proportional relationship between data rate and carrier

frequency, which is illustrated in Fig. 1.3.1. From that figure, it is expected that a data rate of several hundred Gbps can be achieved by using carrier frequency ~ 1 THz.

First THz wireless communications systems were enabled by photonic technologies using optical devices such as laser diodes, modulators, photo-diodes, and optical fiber cables [1.20-1.21]. In those systems the THz frequency carrier wave was generated by a photo-diode such as uni-traveling carrier photodiode (UTC-PD). A data rate of ~ 10 Gbps was obtained with carrier frequency of ~ 120 GHz. Then high data transmission rates of 100 Gbps and beyond were achieved by photonic-based THz wireless communications systems [1.22-1.27]. These results were impressive, proving the huge potential of THz waves for high-capacity wireless communications. However, those systems were still complex because of bulky optical devices, making them difficult to be integrated into portable terminals.

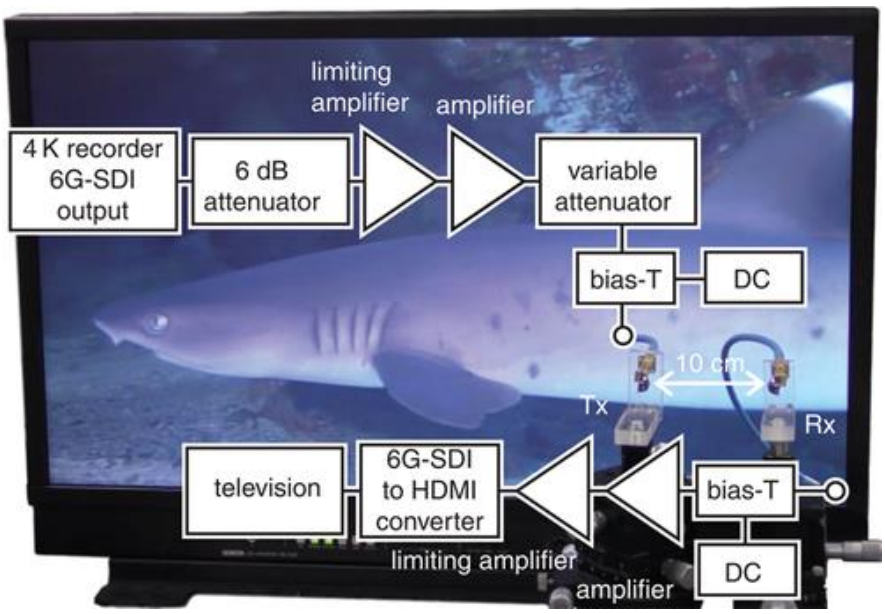


Fig. 1.3.2 Transmission of 4K video signal. (adopted from S. Diebold *et al.*, *Elec.letter*, 52, 24, pp. 1999-2001, 2016. [41]).

The electronic approach could solve that issue owing to the compactness of electronic devices. In recent years, high-capacity wireless communications based on solid-state electronic sources have been investigated intensively using new-generation-transistor-based transmitters [1.28-1.35] and RTD-based transmitters [1.36-1.41]. In Ref. 41, the transmission of an uncompressed 4K video signal was demonstrated in a THz wireless communication system where RTDs were employed in both the transmitter and the receiver. The setup of that THz wireless transmission is shown in Fig. 1.3.2.

- **Terahertz high resolution imaging**

Until now there are two methods to see through the human body, they are ultrasonic and X-ray imaging. Ultrasonic systems require a special medium such as water to feed ultrasonic signals to the scanning object, making their use complicated. While X-ray systems expose health risks for human use because of high-energy photons. Owing to the ability to penetrate through various materials such as clothes, papers, and plastics, THz waves can become another alternative for imaging applications to see through the human body. Because of the shorter wavelength THz imaging feature superior spatial resolution than that of millimeter waves [1.42]. Moreover, because of the non-ionizing characteristics THz imaging is expected useful for non-invasive and non-destructive inspection. The first studies on THz imaging were inspired by advances in femtosecond optoelectronics in the 1990’s decade [1.43-1.44]. Then, with the progress in generating and detecting THz waves, plenty of THz imaging demonstrations have been conducted for food inspection [1.45-1.52], mail envelope checking [1.53-1.56], security body scanning [1.14, 1.57-1.60] and medical diagnostics [1.61-1.62]. Fig.1.3.3 illustrates a THz imaging application for security body scanning, where dangerous weapons hidden

inside clothes or papers will be exposed. Fig.1.3.4 shows an application of THz imaging for medical diagnostics of tooth decay, where a cavity inside the tooth was clearly seen in the THz imaging.

Fig. 1.3.3 Demonstration of security body scanning using THz imaging (adopted from D. Clery, *Science*, vol. 297, 763, 2002. [1.14]).

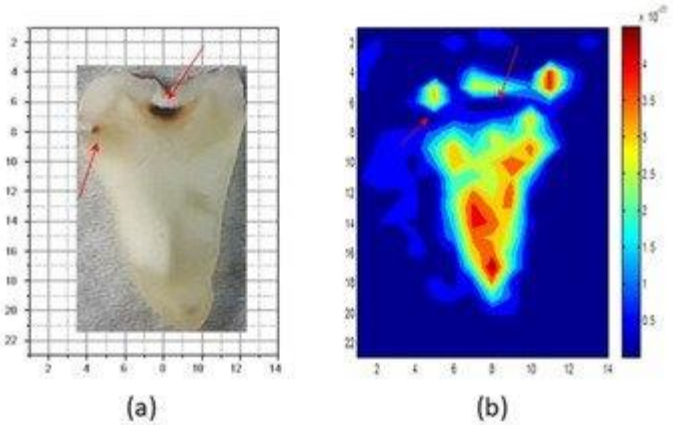


Fig. 1.3.4 (a) Visible and (b) THz imaging of a tooth cavity (adopted from K. Kamburoglu *et al*, *Dentomaxillofac Radiol*, vol. 48, no. 2, 2018 [1.61]).

In recent years, several companies have been developing commercial THz imaging systems for food quality inspection, public security, and medical diagnostics. However, to promote commercial use of THz imaging, plenty of improvements needed to be done including increasing the output power of THz sources and sensitivity of THz detectors, advanced signal processing, real-time imaging, and cost-effectiveness, etc.

- **Terahertz spectroscopy and sensing**

Many living tissues and chemical substances demonstrate a unique absorption spectrum after being illuminated by a THz light source. Such property is the origin for THz spectroscopy and sensing that are expected useful for non-invasive inspection applications. In a typical THz spectroscopy system, a THz source with frequency tunability is employed to illuminate the inspected sample. The absorption coefficient of the THz signal is then measured by a THz detector for each frequency. From the measured absorption coefficient, one can understand what is the inspected sample by comparing measured data with an existing database. Many demonstrations of THz spectroscopy for agriculture [1.63-1.66], biomedicine [1.67-1.69], gas detection [1.70-1.74], and drug detection [1.54, 1.75-1.76] were conducted.

Fig. 1.3.5 shows an example of the absorption coefficient of a highly flammable $CH_3CN$ gas, which was obtained by a THz spectroscopy system using a THz source operating at ~ 330 GHz [1.74]. Such studies could pave the way for future smart security systems. For example, a research group from NICT- Japan proposed an idea of an automatic sensing system of dangerous gases based on the THz spectroscopy technique as shown in Fig. 1.3.6 [1.77].

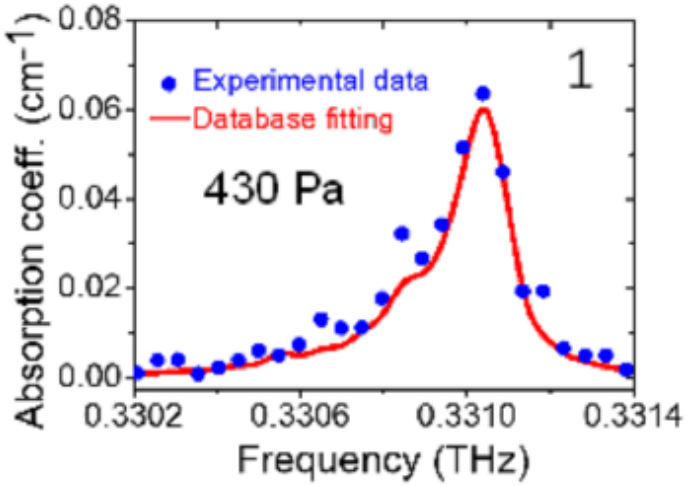


Fig. 1.3.5. Absorption spectra of highly flammable CH3CN gas obtained by a THz spectroscopy system. (Adopted from J. Chen *et al*., *Adv. Photon.* vol. 2, 036004, 2020 [1.74]).

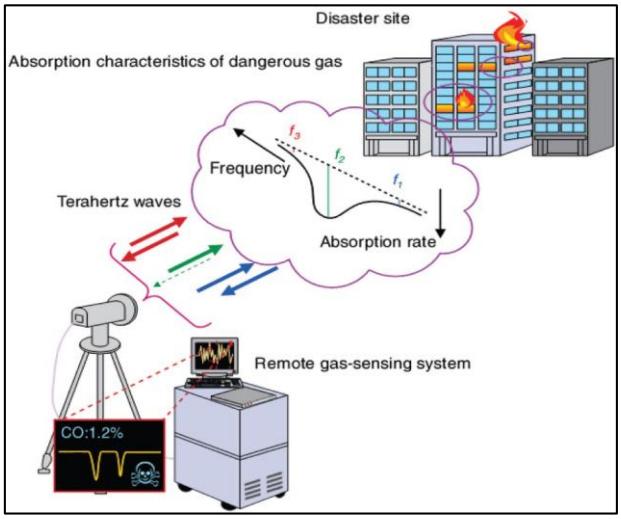


Fig. 1.3.6 Remote gas-sensing system (adopted from N. Shimizu *et al*, *NTT Tech. Rev.*, vol. 7, pp. 1–6, 2009 [1.77]).

To commercialize such systems, improvements of THz source, detector, and signal processing needs to be addressed. Additionally, adopting new progress in AI, and machine learning for signal processing in THz spectroscopy and sensing is a new trend

to develop such smart systems mention above [1.78-1.80].

## 1.4 Terahertz source candidates

In attempts to fill the THz gap, many THz source candidates have been studied and proposed. Because the THz range lies between infrared and millimeter waves, there are two approaches to generating THz waves. They are photonic-based and electronic-based approaches [1.17]. In their early stage of development, THz waves firstly were generated using photonic technologies. Photonic-based THz sources such as free electron lasers [1.81-1.82], gas lasers [1.83], gyrotrons [1.84-1.85], backward-wave oscillators [1.86-1.88], and uni-traveling carrier photodiodes (UTC-PD) [1.89-1.90] can deliver high output power. Those THz sources indeed promote studies of THz wave characteristics and proof-of-concept THz application demonstrations as well. However, they are relatively bulky and expensive, hindering their use in THz commercial applications.

Recently, semiconductor THz source candidates (both photonic-based and electronic-based) have been studied intensively owing to the advantage of compactness and easy massive production. The status of semiconductor THz source candidates is summarized in Fig.1.4.1.

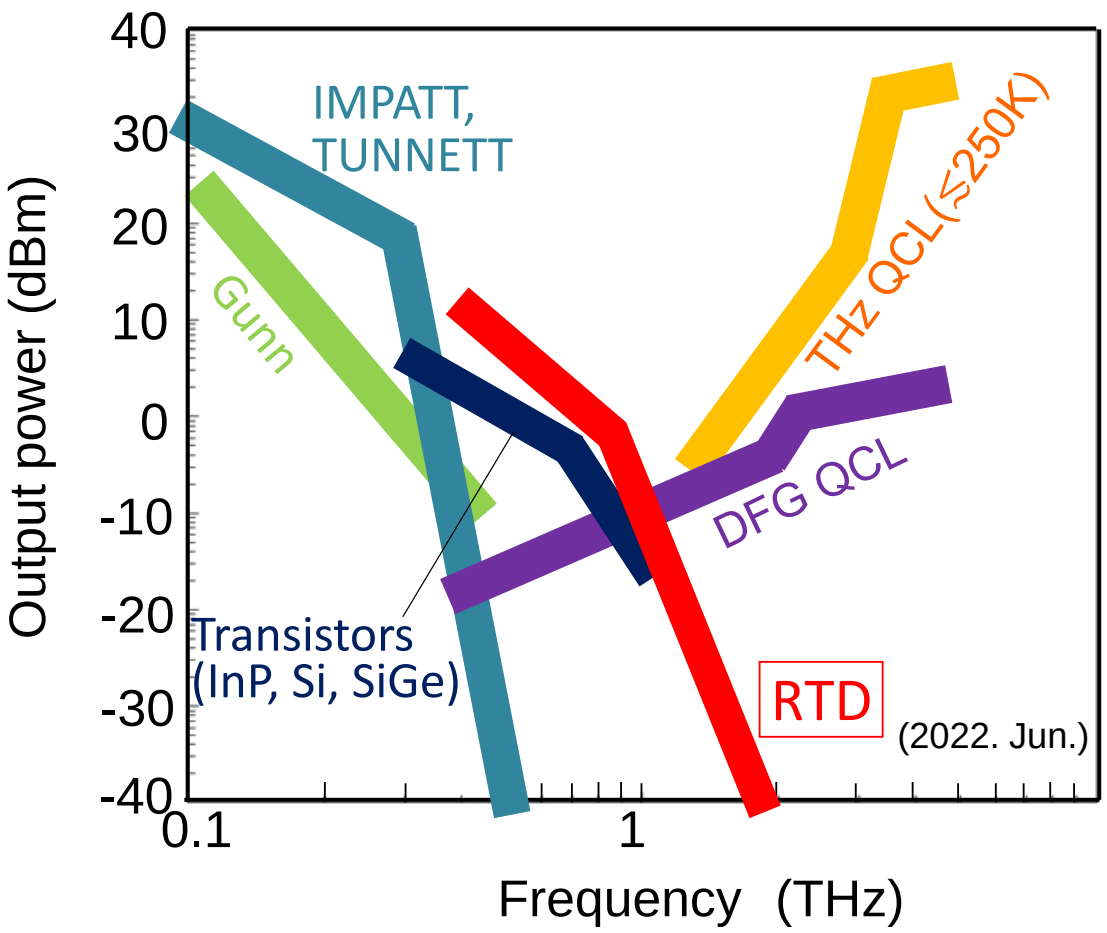


Fig. 1.4.1 Status of semiconductor THz sources.

■ **Quantum cascade lasers**

A promising candidate for THz sources in THz imaging systems is THz quantum cascade laser (QCL) [1.91-1.92]. THz QCL attracts interest from the research community owing to their high oscillation frequency (few THz) and high output power that could reach up to Watts level. Although the concept of the THz QCL was proposed in 1970 years of the previous century, the operation of the THz QCL was only validated in 2002 [1.93]. THz QCL is a periodic structure, each period comprises a thin quantum well sandwiched by two potential barriers [1.93-1.94]. The operation of the THz QCL is based

on a so-called intersubband transition [1.95], which is somewhat similar to lasers. However, in typical semiconductor lasers, the lasing mechanism is based on the interband transition when an electron in the conduction band recombines with a hole in the valence band. After recombination, that electron can no longer participate in another photon emission. While in a QCL, an electron that underwent an intersubband transition can move to the next intersubband again and again. Thus, a single electron can emit multiple photons, resulting in a high output power of THz QCL.

In the THz QCL, the energy gap between intersubbands is relatively similar to that of energy level at room temperature (~25.7 eV). At room temperature, THz transition easily becomes a bipolar process that is undesired for lasing. Therefore, the big challenge for THz QCL is the requirement of cryogenic or thermoelectrical cooling for operation [1.96-1.98]. Increasing the operating temperature of THz QCL close to room temperature is still a goal to achieve for research groups.

An alternative way to achieve THz oscillation at room temperature using THz QCL is to utilize intracavity difference-frequency generation (DFG) based on dual-wavelength mid-infrared QCL. The first DFG QCL was demonstrated in 2008 [1.99]. The THz generation was achieved by mixing two infrared wavelengths [1.100-1.102]. In a DFG QCL, by engineering active region large intersubband separations can be achieved, thus avoiding THz transition, and hence the room temperature operation can be obtained. Although continuous wave (CW) operation is highly desirable for all semiconductor THz sources, CW operation is still challenging for DFG QCLs because of the high amount of dissipated heat.

■ **IMPATT, TUNNETT and Gunn diodes**

From the electronic side, IMPATT, TUNNETT, and Gunn didoes were also studied for THz oscillation. IMPATT and Gunn diodes can provide very high output power in the sub-millimeter wave band. From IMPATT (Impact avalanche transit time) diodes, CW output powers of 980 mW at 100 GHz, and 50 mW at 220 GHz [1.103-1.104] were reported. In an IMPATT diode, the negative differential resistance combines with an external resonant circuit for THz oscillation. TUNNET (tunnel injection transit time) diodes are a variation of the IMPATT diode, which can operate at a higher frequency at the expense of output power. TUNNET diodes with output powers of 140 μW at 355 GHz [1.105], 0.8 nW at 655 GHz [1.106], and 0.2 nW at 701 GHz [1.107] were demonstrated [1.106]. GUNN diodes, which have been widely used in microwave oscillators, were also investigated for the generation of THz waves in the sub-millimeter frequency band [1.108-1.109]. Radiated output power was relatively high at more than 100 mW at ~100 GHz, but rapidly decreases in the frequency range of ~300 GHz.

Despite having high output power, those THz devices require an effective heatsink method for operation. Additionally, in general, those diodes have lower oscillation frequency compared to other THz electronic sources such as transistor-based oscillators and resonant tunneling diode oscillators.

■ **THz oscillator based on new generation transistors.**

The finding of semiconductor transistors in the last century has changed the world a great deal. In our daily life, transistors are found everywhere in various electronic devices. In the THz technology field, THz oscillators based on new-generation transistors have been also studied intensively. Such oscillators have an advantage of a mature fabrication

process for massive production. THz oscillations of several hundred GHz were reported with InP heterojunction bipolar transistors (HBT) [1.110-1.113], and SiGe HBT [1.114-1.115]. Moreover, THz amplifiers based on InP High electron mobility transistors (HEMT) were also demonstrated [1.116-1.117]. Oscillation frequency and output power of THz oscillators based on new-generation transistors are expected to be enhanced in the future, making them important candidates for commercial THz sources.

- **Resonant tunneling diode THz oscillators**

Among electronic devices, resonant tunneling diode (RTD) THz oscillators are a very promising candidate. Such oscillators have the highest oscillation frequency among electronic devices, which has reached close to 2 THz [1.118]. By using a low-loss resonator, RTD oscillators are expected to oscillate at a frequency beyond 2 THz [1.119]. RTD oscillators can operate at room temperature and have compact size [1.120-1.121]. The first RTD THz oscillator was proposed by Tsu-Esaki in 1973 [1.122]. After that, the development of RTD oscillators has been updated many times to reach 712 GHz operation over almost 20 years [1.123]. A new development era of RTD oscillators started in 2000 years. Oscillation frequency reached 831 GHz in 2009 [1.124] and above 1 THz in 2010 [1.125]. After that by structure optimization, the highest oscillation frequency is updated to 1.31 THz in [1.126], 1.46 THz in [1.127], 1.55 THz in [1.128], 1.92 THz in [1.129] and 1.98 THz in [1.118]. Additionally, the frequency tuning functionality of RTD oscillators was also investigated [1.125, 1.130-1.131].

In parallel with studies to increase oscillation frequency, many efforts tried to improve radiated output power including using offset-fed slots [1.132-1.133], rectangular cavity as a resonator [1.134-1.135], and array configurations [1.133, 1.136-1.138].

As RTD oscillators prove to be a promising candidate for THz sources, plenty of THz application demonstrations using RTD oscillators were conducted including wireless communications [1.36-1.41], imaging [1.139-1.140], radars [1.141-1.142] and spectroscopy [1.143].

To be able to integrate into mobile devices, along with low power consumption, high DC to RF conversion efficiency is a highly desired parameter of THz sources. Fig.1.4.2 shows a comparison of DC-to-RF conversion efficiency of room-temperature THz sources that are capable of working up to 1 THz and beyond. It can be seen that RTD oscillators tend to have better DC-to-RF conversion efficiency compared to THz oscillators based on transistors.

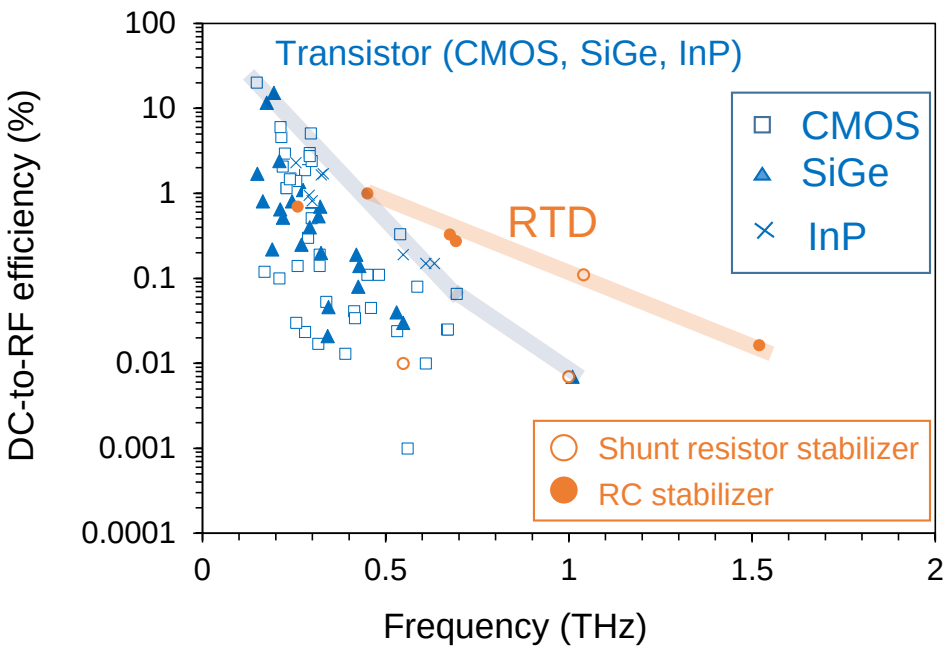


Fig. 1.4.2 Summary of DC-to-RF efficiency of THz sources.

It is highly desired to integrate a large number of elements into a small-sized chip. That ability a THz source can be estimated via a parameter called power density, which is defined by the ratio of the radiated output power to the chip area as

$$\text{Power density} = \frac{P_{\text{out}}}{A_c} \tag{1.2}$$

Where $P_{\text{out}}$ and $A_c$ are the radiated output power and the chip area of the THz source, respectively. Fig.1.4.3 shows a comparison of power density between the RTD oscillators, and the transistor-based oscillators. RTD THz oscillators exhibit high power density as can be seen in Fig.1.4.3. With a very high power density parameter, it is possible to arrange a large number of elements into a small chip area.

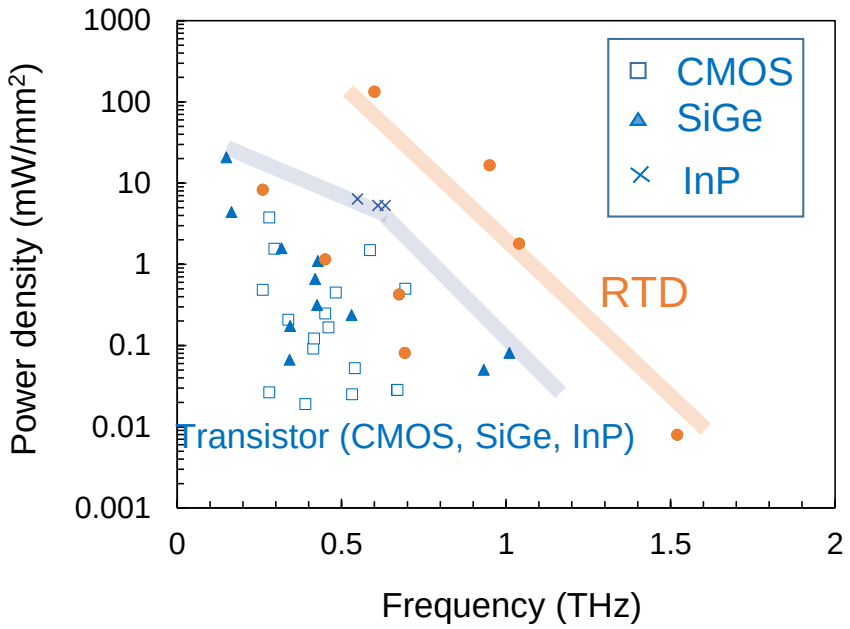


Fig. 1.4.3 Summary of power density of THz sources.

The reason RTD is capable of higher DC-to-RF efficiency and power density is attributed to higher cut-off frequency $f_c$. This is because RTD has very short electron

delay time and RTD has only two terminals instead of three as transistors. Quantitatively, the cut-off frequency $f_c$ of RTD is determined as $1/4\tau \approx 3$ THz, where $\tau$ is the RTD delay time [1.120]. While the cut-off frequency $f_c$ of CMOS [1.2], SiGe [1.2], and InP [1.117] transistors was reported at 0.4 THz, 0.7 THz, and 1.5 THz, respectively. Based on the above summaries, one can see RTD THz oscillators are promising candidates for commercial THz sources.

# 1.5 Purpose and outline of the thesis

**Table. 1.** Main fabrication process steps of common RTD THz oscillators.

| **Work** | | **Fabrication process step** | | | | Resonator - antenna type | Frequency | Output power |
|---|---|---|---|---|---|---|---|---|
| | | Exposure | Metal evaporation | Insulator passivation | Dry-etching | | | |
| [1.214] |  | 6 | 3 | 2 | 2 | Slot | 1.42 | 1 μW |
| [1.118] |  | 6 | 4 | 2 | 2 | Slot | 1.98 | < 1 μW |
| [1.215] |  | 7 | 4 | 1 | 1 | Cylindrical cavity-bowtie | 1.79 | < 1 μW |
| [1.134] |  | 7 | 4 | 1 | 1 | Rectangular cavity-bowtie | N/A | N/A |
| [1.216] |  | 3 | 2 | 2 | 1 | Patch | 0.5 THz | 50 μW |
| [1.217] |  | 5 | 3 | 2 | 1 | Patch | 1.1 THz | 9 μW |
| This work | 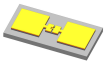 | 2 | 1 | 0 | 1 | Slot | 0.4~1 THz | ~ 10 μW |

Table 1 summarizes the main steps of the fabrication process including lithography exposures, vacuum metal evaporation, dielectric layer passivation, and dry-etching of reported common RTD THz oscillators. As can be seen, common RTD THz oscillators require a relatively complex fabrication process including multiple lithography exposure and vacuum metal deposition, as well as insulator layer passivation. The main reason contributing to the complex fabrication process is due to the existence of MIM capacitors that are used in RTD THz oscillators to separate the DC bias circuit from the THz circuit [1.126-1.129]. Therefore, eliminating MIM capacitors could simplify the fabrication process of RTD oscillators.

Moreover, single RTD oscillators also exhibit relatively low output power as can be seen in Table 1. Array configurations are a common method to enhance the output power of RTD oscillators by power combination [1.136-1.138]. Fig. 1.5.1 shows output power of single and arrayed RTD oscillators for various resonator types. It can be seen output powers of arrayed oscillators were effectively improved compared to that of single oscillators.

However, in coupled arrayed oscillators many operation modes exist, and it is difficult to understand the device's operation.

Therefore, the purpose of this study is to realize RTD THz oscillators with a simplified structure that can be easily fabricated in a short period of time. After that, a simple method to analyze the operation modes of arrayed oscillators is presented. Then new planar array configurations for coherent power combination based on the simplified structure are proposed and validated. Where power combination is obtained by angled arrangements of slot antennas. Additionally, in such array configurations, a new coupling method called

"resistor-coupled" is employed, which makes it easier to realize a stable operation mode of arrayed oscillators.

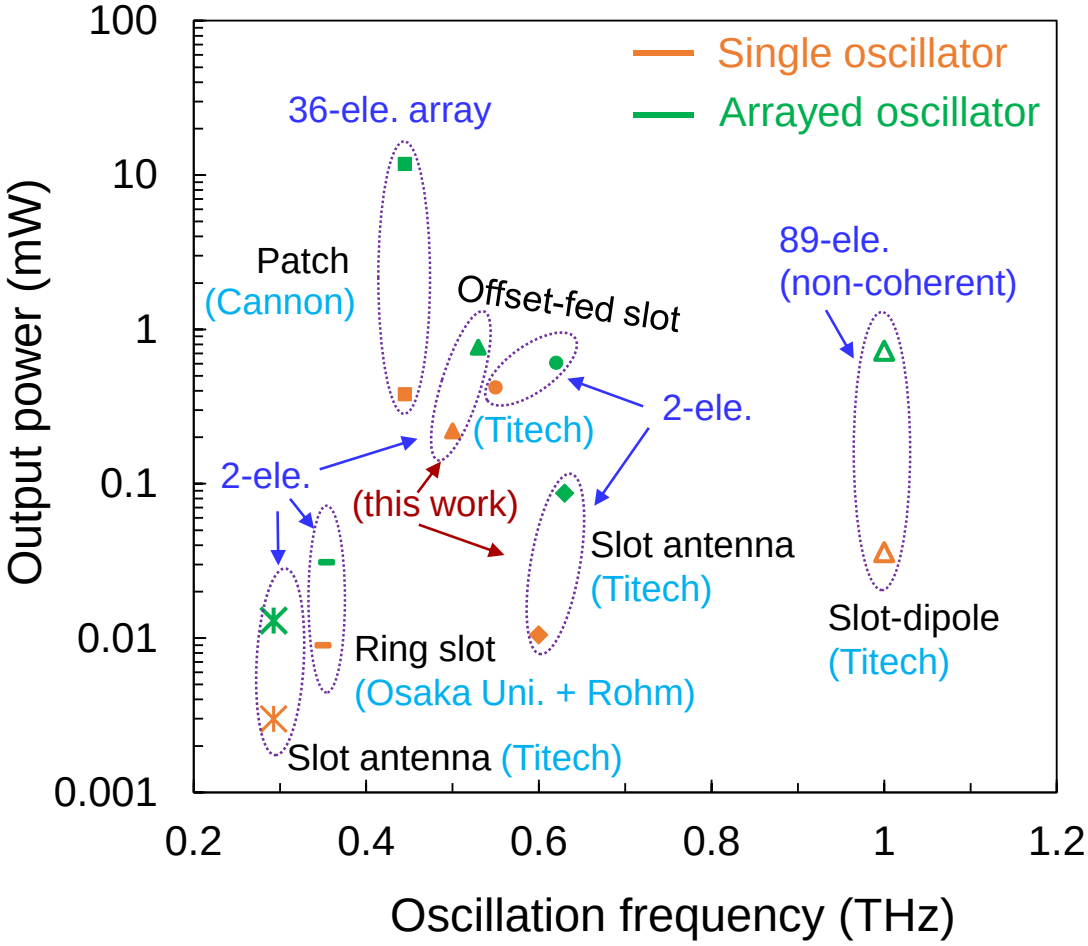


Fig. 1.5.1. Comparison of output power between arrayed and single RTD oscillators for various resonator types.

The outline of the thesis is displayed in Fig.1.5.2. Chapter 2 presents a structure-simplified RTD THz oscillator followed by analyzing its operation principle and fabrication process. Structure optimization for high output power and high frequency of the proposed RTD oscillator is carried out in Chapter 3. In that chapter, offset-fed slots

combined with coplanar stripline antennas are applied to the simplified RTD oscillator to obtain high output power performance. While optimally short slot antenna is investigated to achieve higher oscillation frequency. Chapter 4 investigates array configurations for coherent power combination based on the simplified RTD THz oscillator proposed in the previous chapter. In Chapter 5, the results of Chapter 3 and Chapter 4 are combined for achieving higher output power and high oscillation frequency. Finally, Chapter 6 gives the conclusion of my thesis.

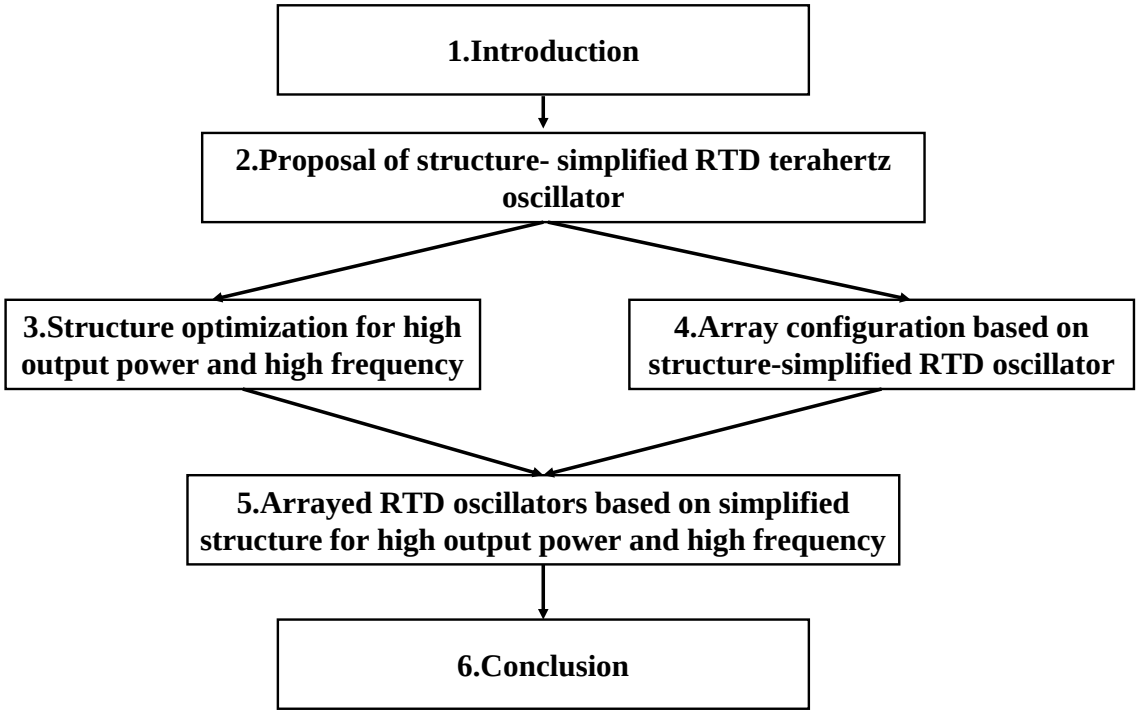


Fig.1.5.2. Outline of the thesis.

# Chapter 2

# Proposal of structure-simplified RTD terahertz oscillator

# 2.1 Introduction

Common RTD oscillators employ MIM capacitors to separate the DC bias circuit from the THz circuits. However, MIM capacitors make the structure and fabrication process of common RTD oscillators complex. In this chapter, the fabrication process of a conventional RTD oscillator is briefly reviewed. After that, a structure-simplified RTD oscillator without MIM capacitors is proposed. Then, the operation of the proposed RTD THz oscillator is explained using equivalent circuits. Next, its fabrication process is carefully described. Then, experimental results, which validate the operation of the structure-simplified RTD oscillator, are presented and analyzed.

# 2.2 Operation principle of RTD

RTD has a semiconductor heterostructure comprising a thin quantum well sandwiched between two potential barriers as illustrated in Fig. 2.2.1. Electrons trapped inside the quantum well have discrete energy levels called resonant levels. The dotted line inside the quantum well illustrates a resonant level. Electrons from the emitter can tunnel to the collector through the resonant level. That mechanism is called resonant tunneling. RTD exhibits a negative differential conductance (NDC) in the current-voltage characteristic as shown in Fig. 2.2.2. At a certain applied bias voltage, electrons have a kinetic energy $E_z$ in the direction perpendicular to the heterostructure. The triangle at the emitter represents the density of the incident electrons into unit area of the heterostructure from the emitter per unit time. The tunneling current is obtained by integration over $E_z$ of the product between the density of electrons incident into unit area of the heterostructure

per unit time, the resonant tunneling probability, and the electron charge. The blue curve inside the quantum well shows the shape of the resonant tunneling probability.

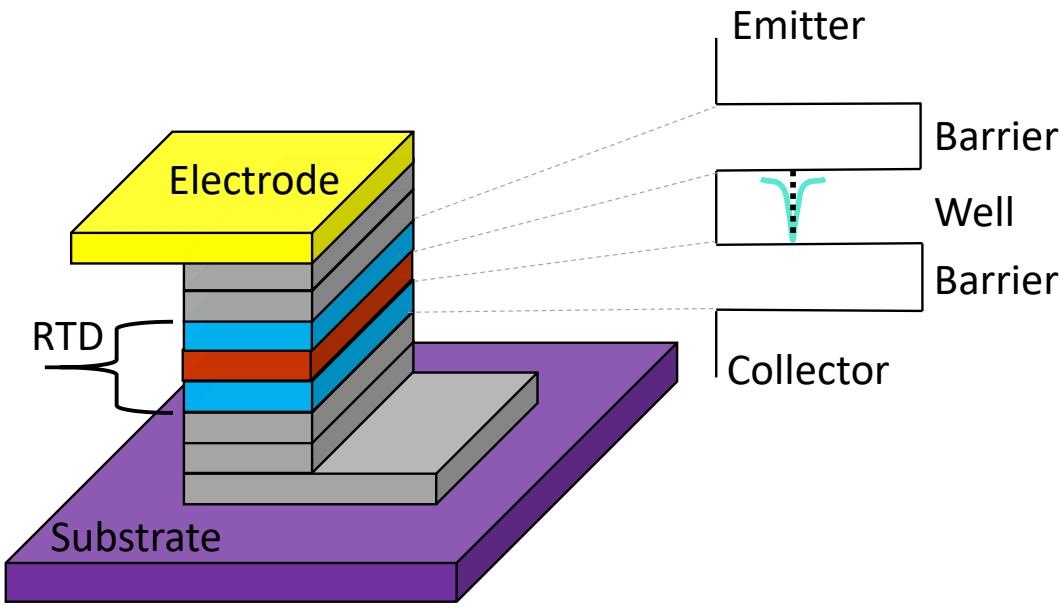


Fig. 2.2.1 RTD simple layer structure and band diagram. The dotted line within the well shows a resonant level of electron energy inside the well. The blue curve within the well shows the shape of the resonant tunneling probability.

At the zero bias, the Fermi level of the emitter is lower than the resonant level in the quantum well, so electrons can't travel from the emitter to the collector, resulting in zero tunneling current. As the applied voltage increases, electrons in the emitter acquire kinetic energy and move faster, resulting in increasing the density of incident electrons into unit area of the heterostructure per unit time. That leads to an increase in the tunneling current. The tunneling current gets maximum at the voltage $V_p$ when both the density of the incident electrons from the emitter and the tunneling probability get peaked. As the bias voltage further increases, because the conduction band edge of the emitter exceeds the

resonant level in the quantum well, the tunneling probability decreases, resulting in the reduction of the tunneling current. That region is called the negative differential resistance (NDR) region in the current-voltage characteristic of RTD. NDR is the key to the construction of RTD oscillators. The voltage width $\Delta V$ and current width $\Delta I$ of an RTD can be defined from the current-voltage characteristic as illustrated in Fig.2.1.2.

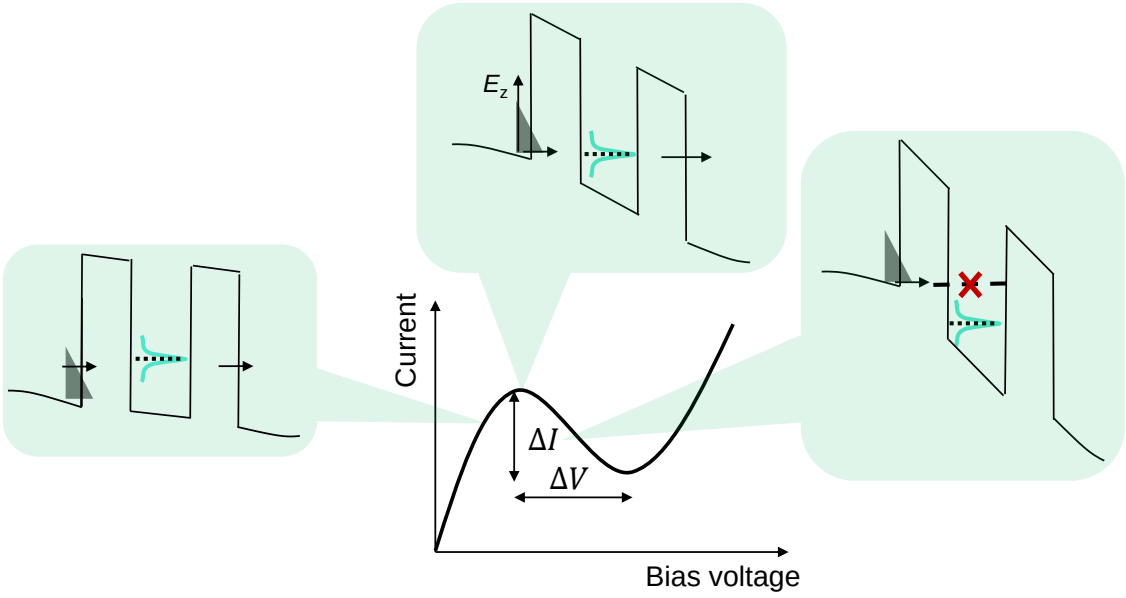


Fig. 2.2.2 RTD current-voltage characteristic.

The current-voltage characteristic of an RTD can be approximated by a third- order polynomial as

$$I_{\mathrm{dc}}(V_{\mathrm{dc}}) \cong \ -aV_{\mathrm{dc}} + bV_{\mathrm{dc}}^3 \tag{2.2.1}$$

Where $a$ and $b$ are approximately defined from current and voltage widths as $a \approx \frac{3}{2}\frac{\Delta I}{\Delta V}$ and $b \approx 2\frac{\Delta \mathrm{I}}{\Delta \mathrm{V}^3} \approx \frac{4}{3}\frac{a}{\Delta \mathrm{V}^2}$ [2.1], respectively. The origin of $V_{\mathrm{dc}}$ is the center of the NDR region.

## 2.3 Conventional RTD THz oscillator

Common RTD oscillators consist of an RTD mesa incorporated into a resonator [2.2-2.4]. RTD negative conductance compensates for the resonator losses for THz oscillation. The resonator inductance combines with RTD capacitance to form a resonant circuit that determines the oscillation frequency. A typical type of RTD THz oscillator is one that employs a slot resonator [2.2, 2.5-2.6]. Fig 2.3.1 shows a conventional RTD THz oscillator with a slot resonator that also acts as an antenna for radiating THz waves.

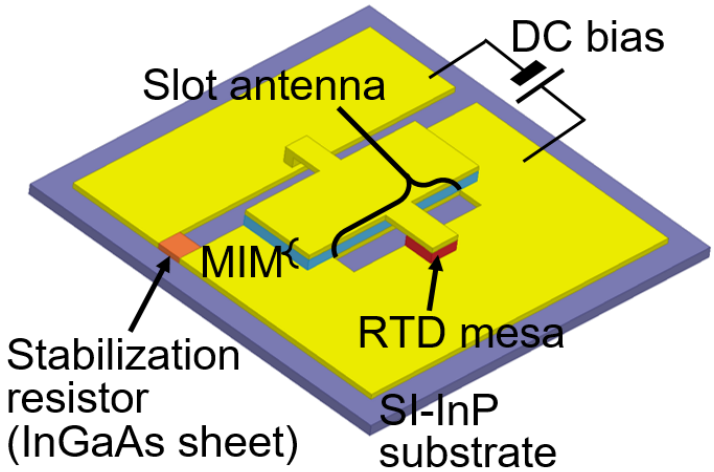


Fig. 2.3.1 Conventional RTD THz oscillator.

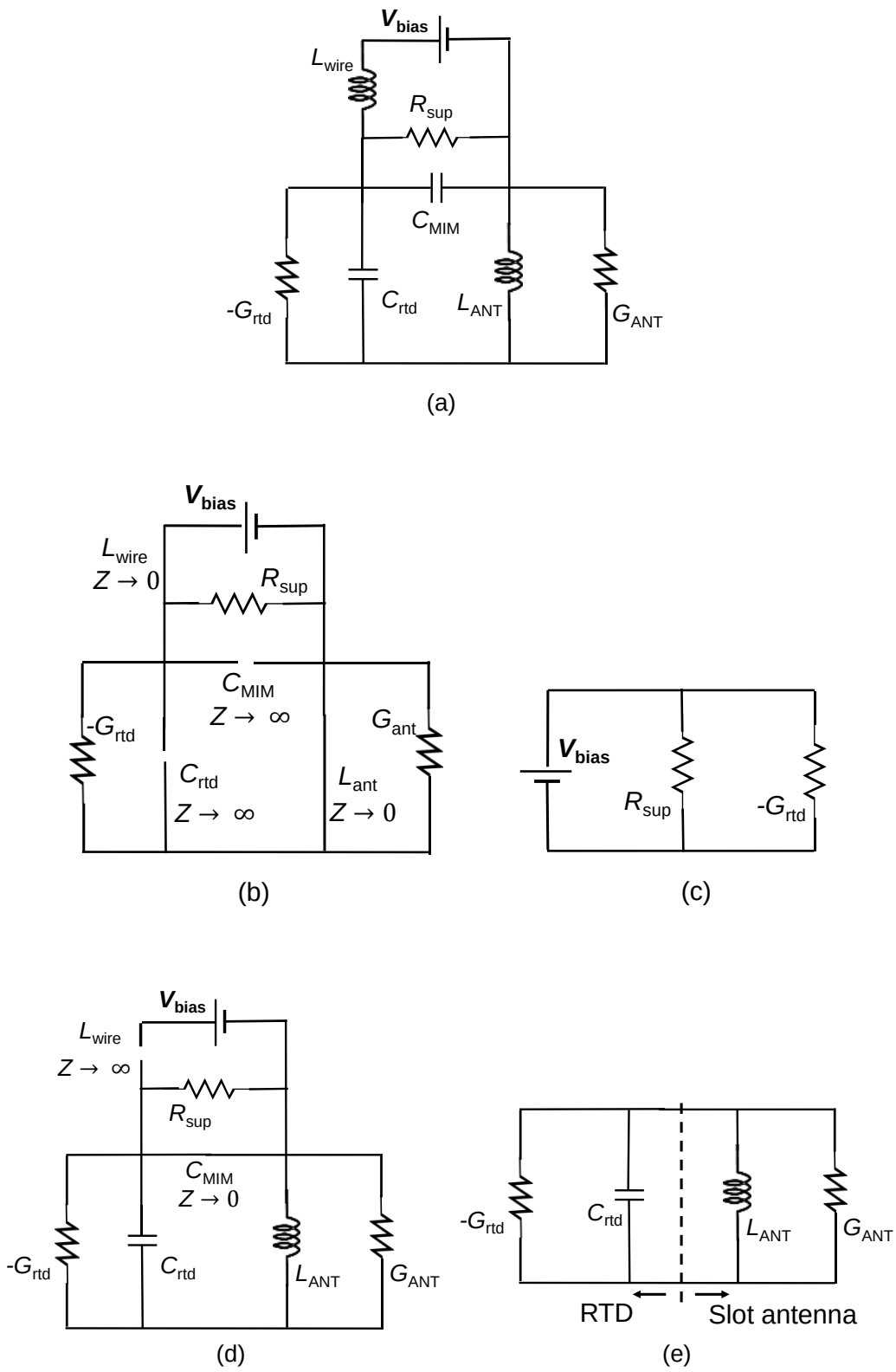


Fig. 2.3.2 Equivalent circuits of conventional RTD THz oscillator.

In this RTD oscillator, the RTD mesa is incorporated into a slot antenna. A MIM capacitor is employed to separate the DC bias circuit from the THz circuit which is discussed in more detail by the below equivalent circuits. A stabilization resistor connected in parallel with RTD to suppress low-frequency parasitic oscillation. The whole structure is grown on a semi-insulator indium phosphide (SI-InP) substrate. The operation principle of the conventional RTD THz oscillator shown in Fig.2.3.1 can be explained using its equivalent circuits.

The general equivalent circuit of the RTD oscillator shown in Fig.2.3.1 is displayed in Fig.2.3.2(a). Where, $-G_{rtd}$ and $C_{rtd}$ are RTD NDC and RTD capacitance, respectively. $R_{sup}$ is the stabilization resistor to suppress low-frequency parasitic oscillation. $L_{wire}$ is the inductance of the biasing wires. $L_{ANT}$ and $G_{ANT}$ are the inductance and conductance of the antenna structure, respectively. The latter includes two components called conduction loss $G_{loss}$ and radiation conductance $G_{rad}$, hence $G_{\mathrm{ANT}} = G_{\mathrm{rad}} + G_{\mathrm{loss}}$. In the low-frequency range, the RTD capacitor has a very large impedance and the antenna inductance has a very small impedance as shown in Fig.2.3.2(b). The equivalent circuit of the conventional RTD oscillator in the low-frequency range becomes the one shown in Fig.2.3.2(c). Thus, the stabilization resistor cancels RTD negative conductance to suppress low-frequency parasitic oscillations. In the THz frequency range, the MIM capacitor has a very small impedance, thus shorting the DC bias circuit. The equivalent circuit of the conventional RTD oscillator in the THz range is obtained as displayed in Fig. 2.3.2 (d, e). The left side part corresponds to the RTD and the right side part corresponds to the antenna structure. Hence, the oscillation condition of the RTD oscillator is that RTD negative conductance can compensate for the losses caused by antenna structure:

$$G_{\mathrm{rtd}} \geq G_{\mathrm{ANT}} \tag{2.3.1}$$

The oscillation frequency is determined by the resonance of the LC tank circuit including RTD capacitance and antenna inductance:

$$f_{\mathrm{osc}} = \frac{1}{2\pi\sqrt{L_{\mathrm{ANT}}C_{\mathrm{rtd}}}} \tag{2.3.2}$$

The voltage of the THz oscillation has form $v_{\mathrm{ac}}(t) = V_{\mathrm{ac}} cos 2\pi f_{\mathrm{osc}} t$, where $V_{ac}$ is the amplitude of the THz oscillation and $V_{\mathrm{ac}} = \sqrt{\frac{4}{3b}(a - G_{\mathrm{ANT}})}$ [2.1]. The output power, therefore, is calculated as

$$P_{\mathrm{out}} = \frac{1}{2} G_{\mathrm{rad}} {V_{\mathrm{ac}}}^2 = \frac{2}{3b} G_{\mathrm{rad}}(a - G_{\mathrm{ANT}}) \tag{2.3.3}$$

Substituting $b \approx \frac{4}{3}\frac{a}{\Delta V^2}$ and $G_{\mathrm{ANT}} = G_{\mathrm{rad}} + G_{\mathrm{loss}}$ into the above formula we obtain

$$P_{\mathrm{out}} \approx \frac{1}{2}\frac{G_{\mathrm{rad}}}{a}(a - G_{\mathrm{loss}} - G_{\mathrm{rad}})\Delta V^2 \tag{2.3.4}$$

The fabrication process of the conventional RTD THz oscillator shown in Fig.2.3.1 was described in Ref [2.7]. The fabrication sketch flow is summarized in Fig. 2.3.3.

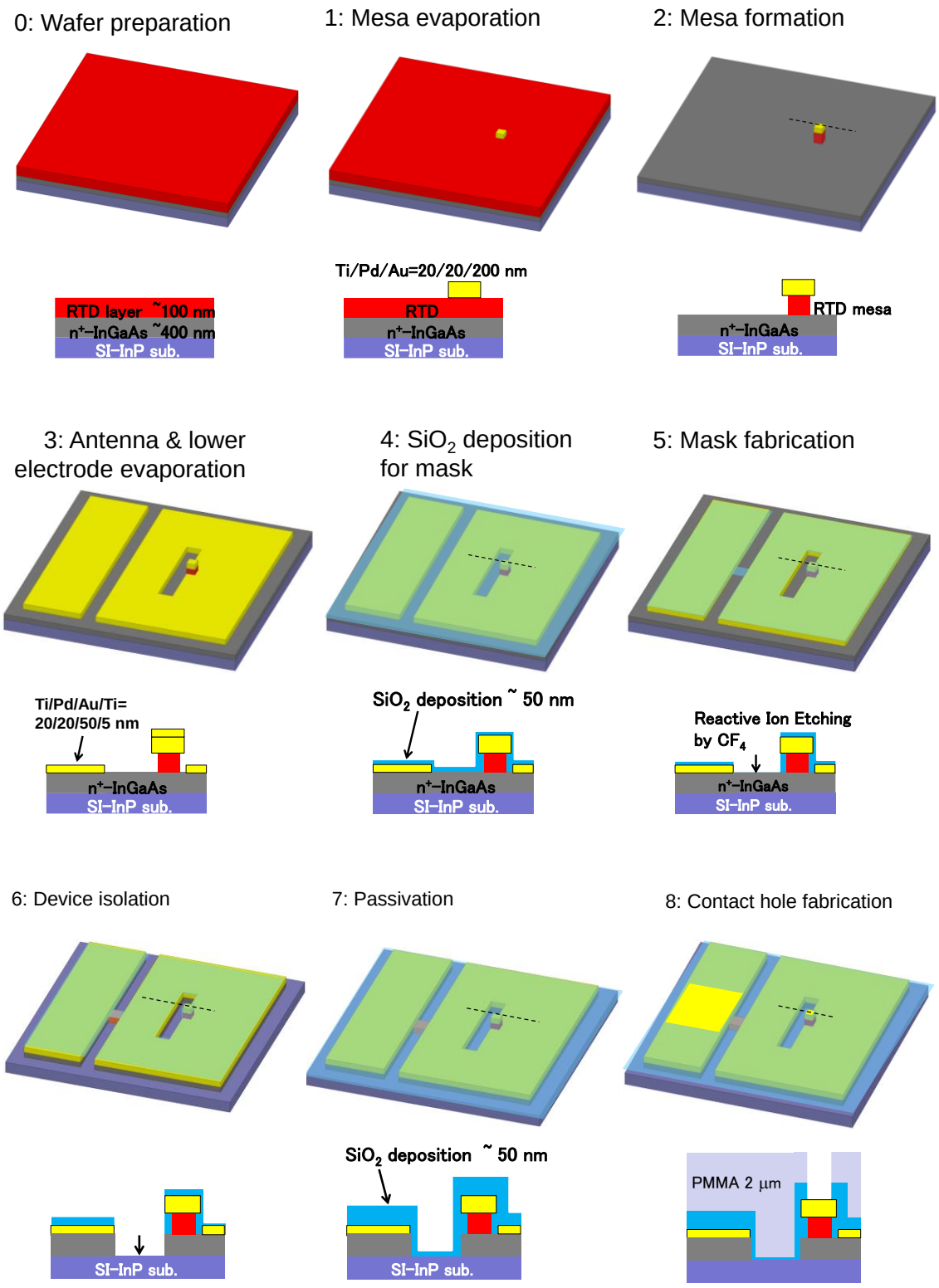
0: Wafer preparation
RTD layer ~100 nm
n+-InGaAs ~400 nm
SI-InP sub.
1: Mesa evaporation
Ti/Pd/Au=20/20/200 nm
RTD
n+-InGaAs
SI-InP sub.
2: Mesa formation
RTD mesa
n+-InGaAs
SI-InP sub.
3: Antenna & lower electrode evaporation
Ti/Pd/Au/Ti= 20/20/50/5 nm
n+-InGaAs
SI-InP sub.
4: SiO2 deposition for mask
SiO2 deposition ~ 50 nm
n+-InGaAs
SI-InP sub.
5: Mask fabrication
Reactive Ion Etching by CF4
n+-InGaAs
SI-InP sub.
6: Device isolation
SI-InP sub.
7: Passivation
SiO2 deposition ~ 50 nm
SI-InP sub.
8: Contact hole fabrication
PMMA 2 μm

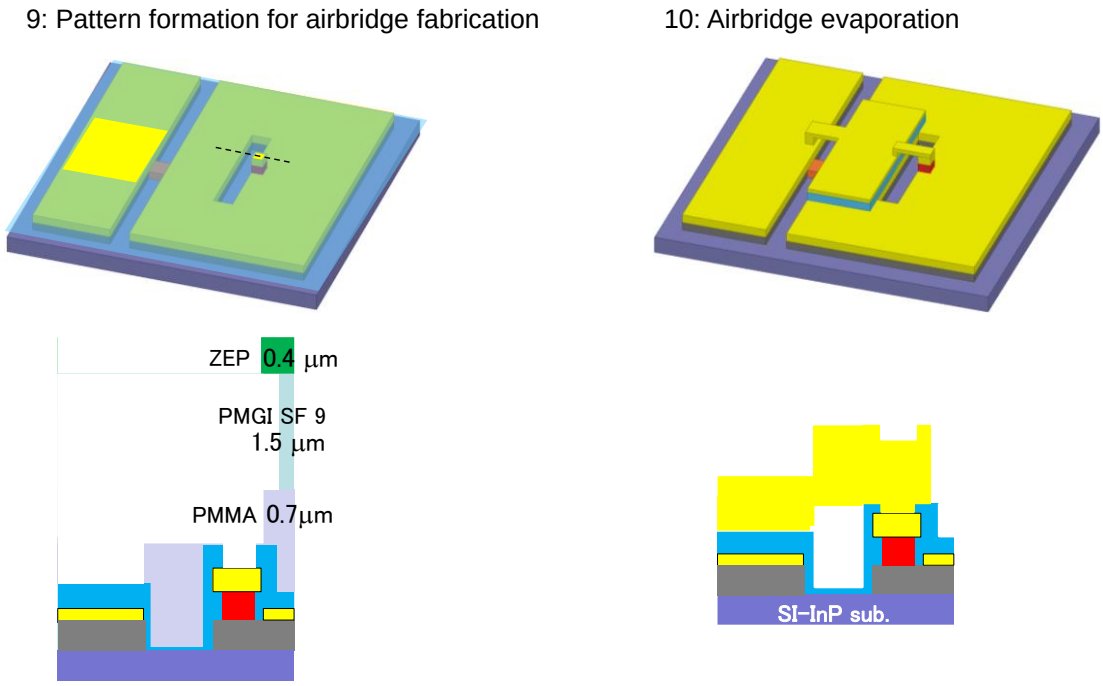


Fig. 2.3.3 Fabrication process flow of the conventional RTD THz oscillator.

Table 2.1

| Fabrication process step | Times |
|---|---|
| EB exposure | 6 |
| Resist coating | 5 |
| Development | 6 |
| Evaporation | 3 |
| $SiO_2$ passivation | 2 |
| RIE dry-etching | 2 |

In summary, it required six times electron-beam exposure, triple vacuum metal evaporation, twice insulator passivation, and twice RIE dry-etching. In addition to this, multiple times of resist coating and development were also required to fabricate the

conventional RTD THz oscillator. The main fabrication process steps of the conventional RTD oscillator are summarized in Table. 2.1.

The main reason contributing to the fabrication complexity of the conventional RTD oscillator is the existence of the MIM capacitor. In the next sections of this chapter, a structure-simplified RTD THz oscillator without MIM capacitors is proposed, fabricated, and validated by experimental results.

# 2.4 Proposal of structure-simplified RTD THz oscillator

### 2.4.1. Device structure and operation principle

The structure-simplified RTD THz oscillator without MIM capacitors is shown in Fig.2.4.1. In the proposed structure, an RTD mesa is still incorporated at the center of a slot antenna that acts both as a resonator for the formation of THz standing waves and as a radiator for radiating THz waves. In this structure-simplified RTD oscillator, MIM capacitors are eliminated. Additionally, to form the slot antenna, two stabilization resistors are formed at both ends of the slot. Those resistors also have the function of suppressing low-frequency parasitic oscillations. The RTD is biased through biasing pads. Similar to the conventional RTD oscillator in the previous section, the whole structure of the simplified RTD oscillator is also grown on a semi-insulator indium-phosphide (InP) substrate.

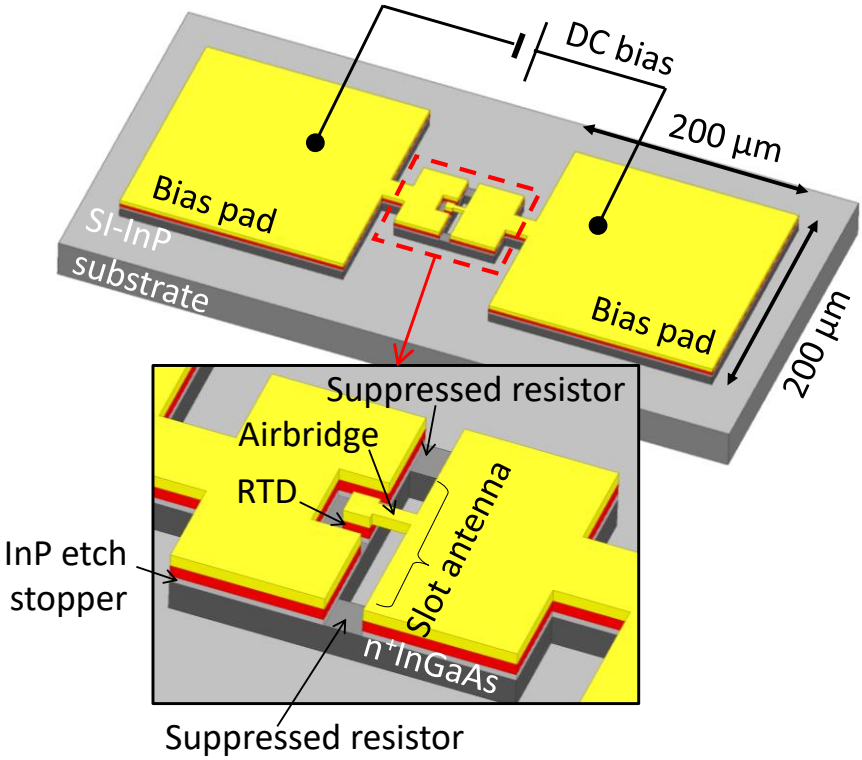


Fig. 2.4.1.1 Structure-simplified RTD THz oscillator.

The operation of the structure-simplified RTD oscillator is explained based on its equivalent circuit. Fig.2.4.1.2 shows the general equivalent circuit of the structure-simplified RTD oscillator. In this equivalent circuit, $L_{wire}$ and $L_{slot}$ are the inductances of the biasing wires and the slot antenna, respectively. $R_{sup}$ is the stabilization resistor. $C_p$ is the capacitance formed by the RTD upper electrode and the bottom $n^+$ InGaAs layer. $G_{rad}$ is the radiation conductance of the antenna structure.

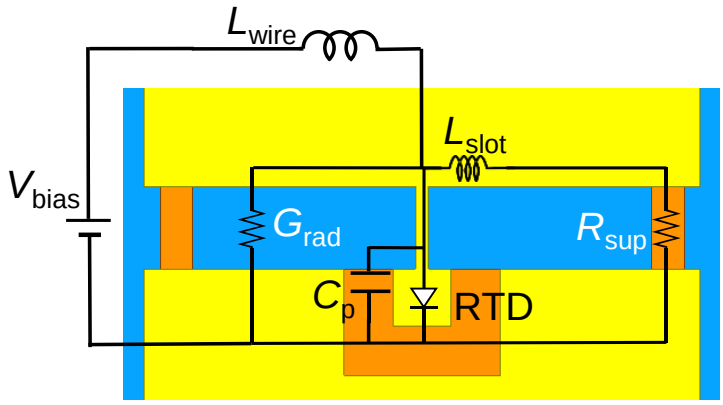


Fig. 2.4.1.2 General equivalent circuit of structure-simplified RTD THz oscillator.

In the low-frequency range, the impedances of $L_{wire}$ and $L_{slot}$ are small compared to the stabilization resistors; therefore, the inductances $L_{wire}$ and $L_{slot}$ can be neglected; the admittances of the parallel capacitors $C_{rtd}$ and $C_p$ are very low, therefore, the capacitors $C_{rtd}$ and $C_p$ can be ignored. Additionally, radiation conductance $G_{rad}$ is also very small in the low-frequency range. Thus, $Y$ contains only the real component $G' = 1/R_{sup}$. Fig. 2.4.1.3 shows the equivalent circuit in the low-frequency range. Consequently, the stabilization resistors cancel out $G_{rtd}$ to suppress the low-frequency parasitic oscillations.

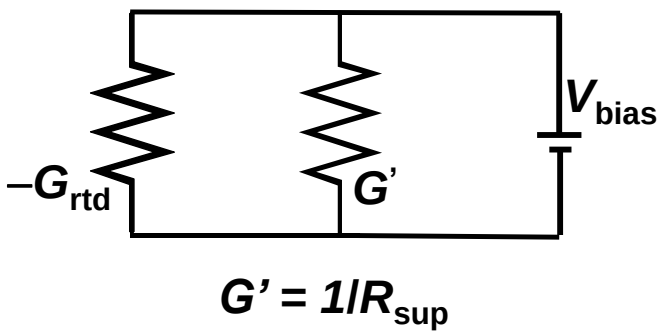


Fig. 2.4.1.3 Equivalent circuit of structure-simplified RTD oscillator in the low-frequency range.

In the THz frequency range, the impedances of $L_{wire}$ is very high. Therefore, $L_{wire}$ separates the DC bias circuit from the THz circuit. The equivalent circuit in the THz range of the structure-simplified RTD oscillator is obtained as in Fig.2.4.1.4. The total admittance $Y$ viewed from the RTD can be expressed as

$$Y = \frac{1}{R_{\mathrm{sup}} + j\omega L_{\mathrm{slot}}} + j\omega C_{\mathrm{p}} + G_{\mathrm{rad}}. \tag{2.4.1.1}$$

This admittance can be rewritten as

$$Y = \frac{R_{\mathrm{sup}}}{R_{\mathrm{sup}}^2 + \omega^2 L_{\mathrm{slot}}^2} + G_{\mathrm{rad}} + j\omega C_{\mathrm{p}} - \frac{j\omega L_{\mathrm{slot}}}{R_{\mathrm{sup}}^2 + \omega^2 L_{\mathrm{slot}}^2}. \tag{2.4.1.2}$$

The real part of $Y$ comprises a conduction loss $G_{loss}$ and a radiation conductance $G_{rad}$. The conduction loss $G_{loss}$ is expressed as $G_{loss} = R_{sup}/(R_{sup}^2 + \omega^2 L_{slot}^2)$. The admittance of the RTD is composed of a negative differential conductance $-G_{rtd}$ for the real part and a susceptance of the capacitance $j\omega C_{rtd}$ for the imaginary part.

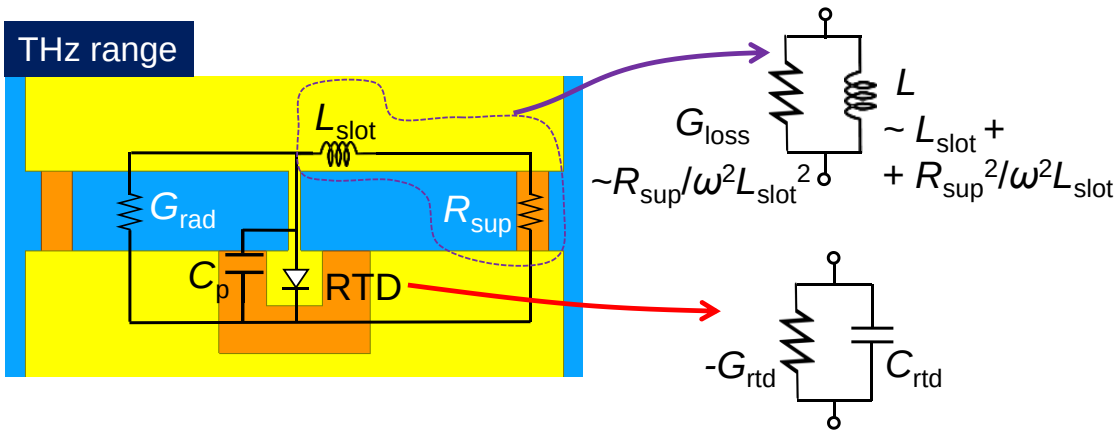


Fig. 2.4.1.4 Equivalent circuit of structure-simplified RTD THz oscillator in the THz frequency range.

As an electron travels from the emitter to the collector, it experiences a delay time

including the tunneling time $\tau_{\mathrm{RTD}}$ in the well and the transit time $\tau_{\mathrm{dep}}$ at the collector depletion layer [1.120]. The electron delay time is defined as $\tau = \tau_{\mathrm{RTD}} + \tau_{\mathrm{dep}}/2$. Due to the existence of RTD electron delay time, $G_{\mathrm{rtd}}$ changes with frequency as $-G_{\mathrm{rtd}} = -G_{\mathrm{rtd}}(0)\cdot\cos(\omega\tau)$, where $G_{\mathrm{rtd}}(0) = (3/2)\cdot(\Delta I/\Delta V)$ is the NDC of RTD at DC. RTD capacitance also includes a component caused by the electron delay time as $C_{\mathrm{rtd}} = C_0 + C_{\mathrm{rtd}}(\tau)$, where $C_0$ is the geometrical capacitance of RTD, and $C_{\mathrm{rtd}}(\tau)$ is the capacitance caused by the electron delay time. $C_{\mathrm{rtd}}(\tau)$ is equivalent to a negative quantum inductance and can be approximated as $C_{\mathrm{rtd}}(\tau) = \tau\cdot G_{\mathrm{rtd}}(0)$. In this study, $C_0$, $\tau_{\mathrm{RTD}}$, $\tau_{\mathrm{dep}}$, $G_{\mathrm{rtd}}(0)$ are extracted by fitting with experimental results.

The equivalent circuit in Fig. 2.4.1.4 can be converted in the form of a parallel circuit in the THz range of the structure-simplified RTD oscillator is obtained as in Fig.2.4.1.5. The left side part corresponds to the RTD and the right side one corresponds to the antenna structure.

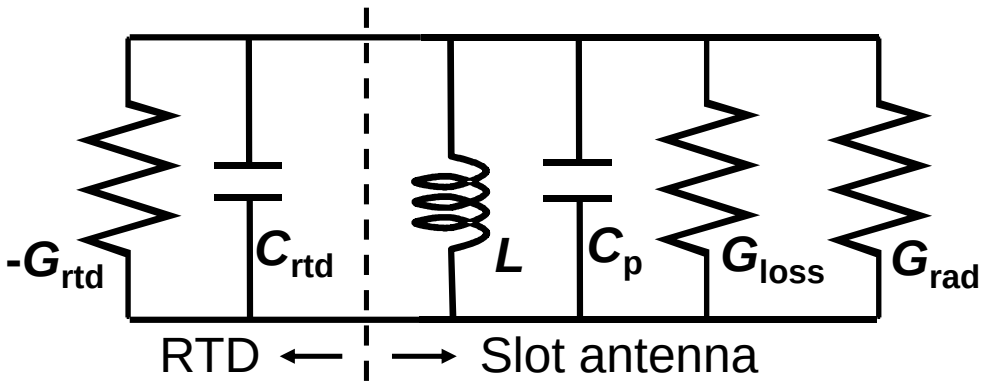


Fig. 2.4.1.5 Equivalent circuit of structure-simplified RTD THz oscillator in the THz frequency range in the form of a parallel circuit.

The equivalent circuit is validated by comparing the antenna admittance extracted from a 3D electromagnetic simulator (ANSYS HFSS) with the admittance calculated using the equivalent circuit. To determine the antenna admittance, in the HFSS simulation the RTD is replaced by a lumped port.

Fig. 2.4.1.6 shows the antenna admittance extracted from the HFSS simulation as indicated by solid lines, along with the antenna length and width and stabilization resistor width $w$ used in the simulation. The parameters of the equivalent circuit are estimated as follows. The imaginary part of the antenna admittance peaks at 175 GHz. At this frequency, the capacitor $C_p$ can be neglected because of the negligible admittance. Hence, the parameters of the equivalent circuit $L_{slot}$ and $R_{sup}$ can be estimated from the imaginary part at this frequency. The imaginary part crosses zero at 1.425 THz, based on which the $C_p$ value can be calculated. The radiation conductance $G_{rad}$ is estimated as the product of the antenna efficiency and the real part of the antenna admittance, which are obtained from HFSS simulation. It is found that the radiation conductance changes with frequency. The dashed lines in Fig. 2.4.1.6 indicate the admittance calculated from the equivalent circuit.

It should be noted that the admittances, shown in Fig. 2.4.1.6, do not account for the biasing wire inductance $L_{wire}$. Nevertheless, this does not affect the result because, in practice, the inductance of biasing wires is relatively high. The admittance extracted from the HFSS agrees well with that calculated from the equivalent circuit. The small series resonance at approximately 1.1 THz is attributed to a dipole resonance with the electrodes outside the slot antenna.

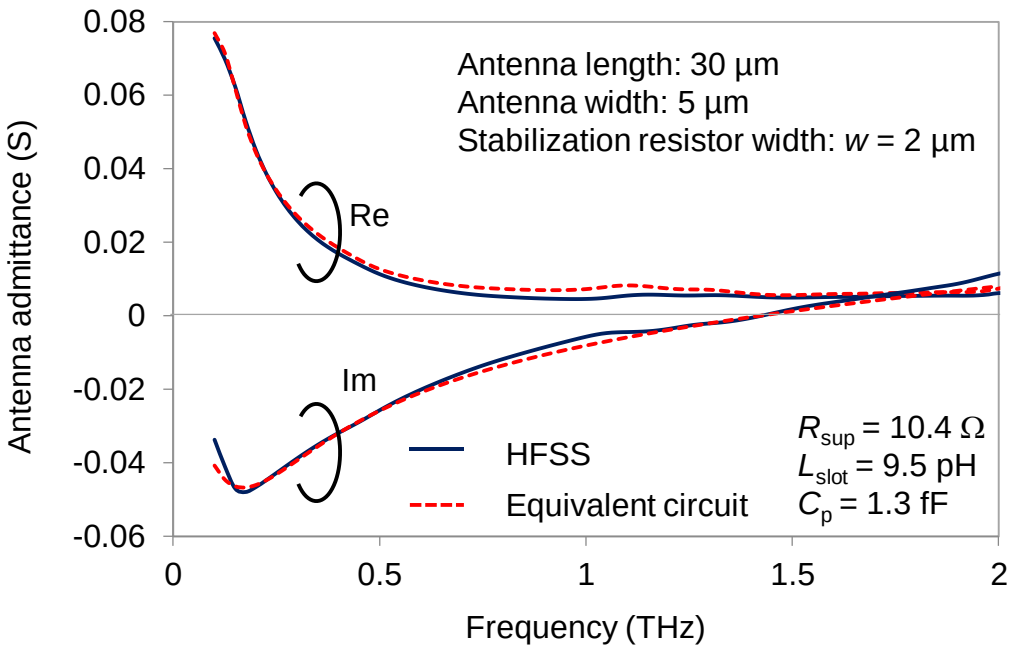


Fig. 2.4.1.6 Comparison of antenna admittances calculated from HFSS simulation and equivalent circuit.

The oscillation frequency $f_{osc}$ is the point at which the total susceptance of the RTD and antenna equals zero, and is obtained as

$$f_{\mathrm{osc}} = \frac{1}{2\pi}\sqrt{\frac{1}{L_{\mathrm{slot}}(C_{\mathrm{p}}+C_{\mathrm{rtd}})} - \frac{R_{\mathrm{sup}}^2}{L_{\mathrm{slot}}^2}}. \tag{2.4.1.4}$$

$f_{osc}$ is determined by the parallel resonance of $L_{slot}$, $C_p$, and $C_{rtd}$. However, it is also affected (decreases) by $R_{sup}$, which is validated by experimental result later in this chapter.

The output power of the structure-simplified RTD oscillator can be also calculated using the same formula (2.3.4) for the conventional RTD oscillator, which is $P_{\mathrm{out}} \approx \frac{1}{2}\frac{G_{\mathrm{rad}}}{a}(a - G_{\mathrm{loss}} - G_{\mathrm{rad}})\Delta V^2$. However, for the conventional RTD oscillator, the conduction loss $G_{loss}$ can be approximated as $G_{\mathrm{loss}} \approx (R_s + R_b)/(\omega L_{\mathrm{slot}})^2$ [2.6, 2.8]. Where $R_s$, $R_b$ are the resistance along the periphery of the slot and the resistance of the air-bridge structure, respectively. While for structure-simplified RTD oscillator, the

conduction loss is approximated as $G_{\mathrm{loss}} \approx (R_{\mathrm{sup}} + R_s + R_b)/(\omega^2 L_{\mathrm{slot}}^2)$. Due to the existence of $R_{\mathrm{sup}}$, the conduction loss of the simplified structure slightly increases. Fig. 2.4.1.7 shows the performance expectation of the proposed structure-simplified RTD oscillator. Because of the additional loss caused by $R_{\mathrm{sup}}$, the oscillation frequency limit and output power of the simplified structure slightly decrease. However, this effect is minor and THz oscillation still can be obtained.

Moreover, in Chapter 4, by utilizing the odd mode operation in an arrayed oscillator, the loss caused by stabilization resistors is mitigated. Then by optimizing the simplified structure as discussed in Chapter 5, the additional loss caused by $R_{\mathrm{sup}}$ is completely vanished and oscillation characteristics of the simplified structure become comparable to that of the conventional structure while the simplified structure can be realized in the much a shorter time than that of the conventional structure.

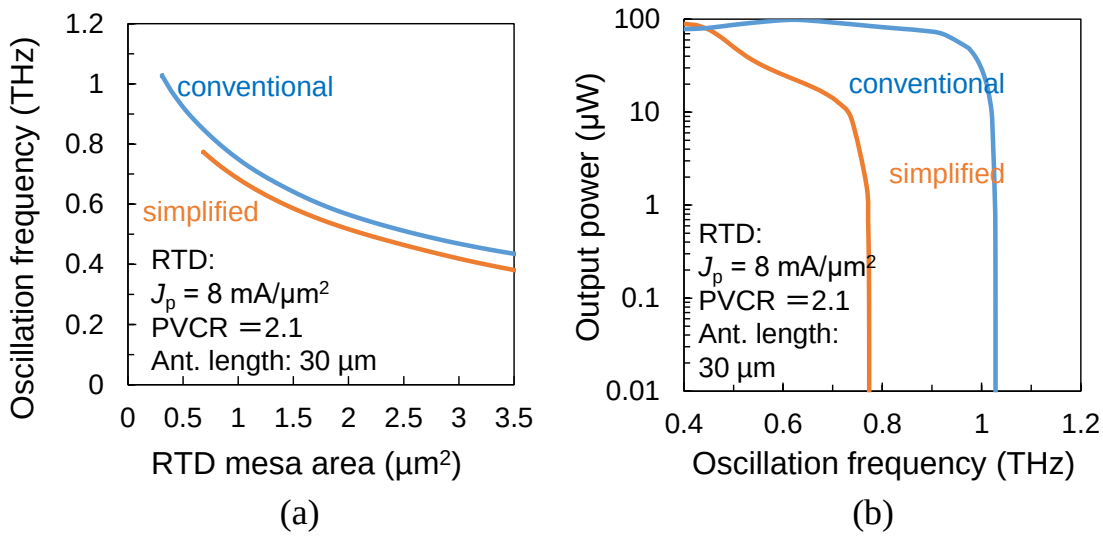


Fig. 2.4.1.7 Calculated oscillation frequency (a) and output power (b) of structure-simplified and conventional RTD oscillators.

### 2.4.2. Fabrication process of structure-simplified RTD THz oscillator

To fabricate the device, we utilized an RTD grown on a semi-insulator indium phosphide (InP) substrate. Fig. 2.4.2.1(a) shows the detailed epitaxial layer structure of the RTD. The main part of the RTD is formed by sandwiching a thin quantum well between two potential barriers. The thicknesses of the well and barriers are 3 and 1.2 nm, respectively. When a bias voltage is applied to an RTD, it exhibits a negative differential conductance. Fig. 2.4.2.1(b) shows the measured *J*–*V* characteristic of an RTD mesa with an area of ~1.2 μm$^2$. A unique feature of the RTD layer design is the incorporation of an etch-stopper layer, which is not employed in conventional RTDs. The purpose of this layer is to effectively control the chemical wet-etching process during mesa formation, which is described below. The sketch flow of the fabrication process of the structure-simplified RTD oscillator is depicted in Fig. 2.4.2.2 (a, b, c). The fabrication process is described as follows.

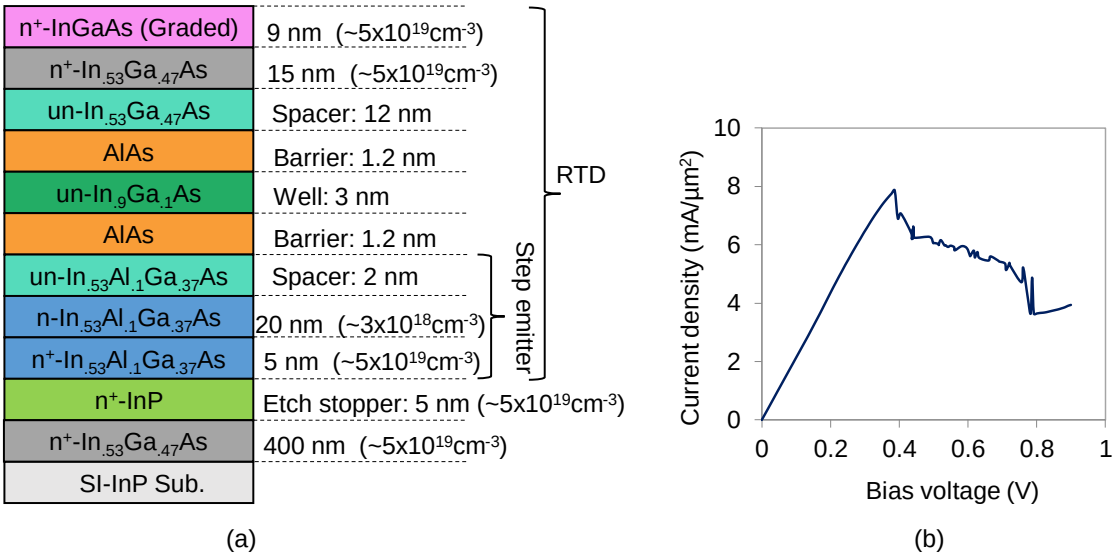


Fig. 2.4.2.1 Oscillation frequency as a function of RTD mesa area.

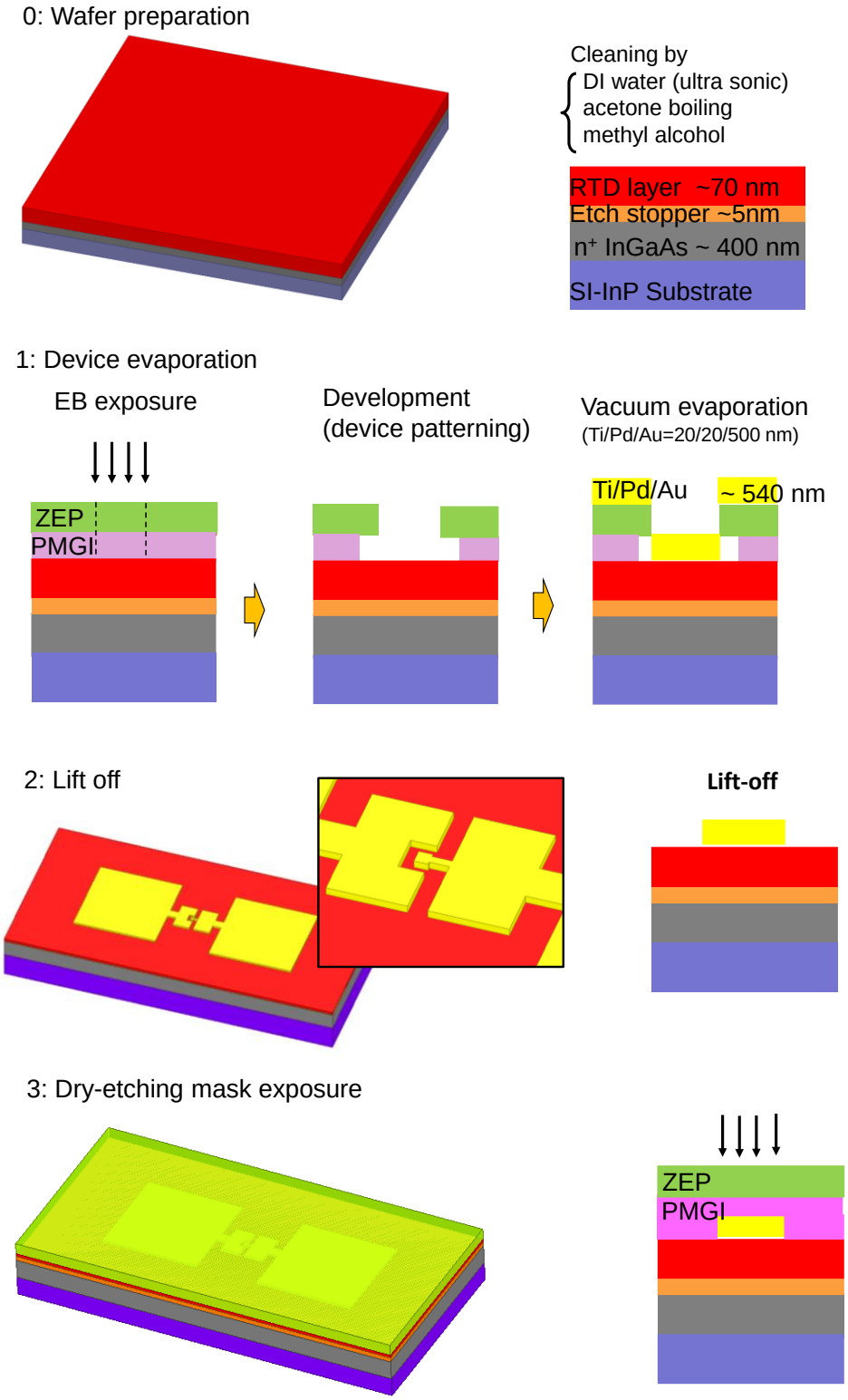


Fig. 2.4.2.2 (a) Fabrication process of the structure-simplified RTD oscillator.

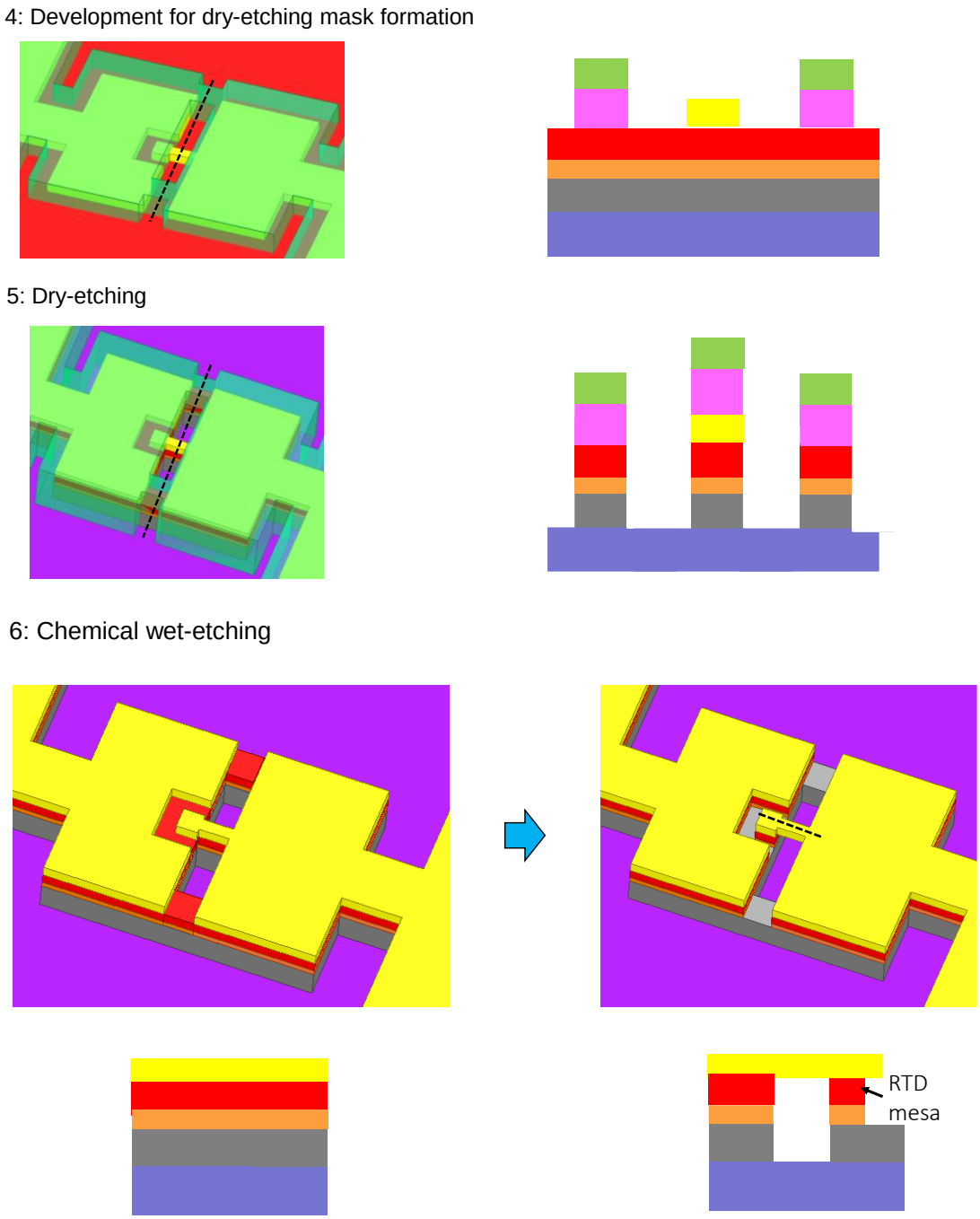


Fig. 2.4.2.2 (b) Fabrication process of the structure-simplified RTD oscillator.

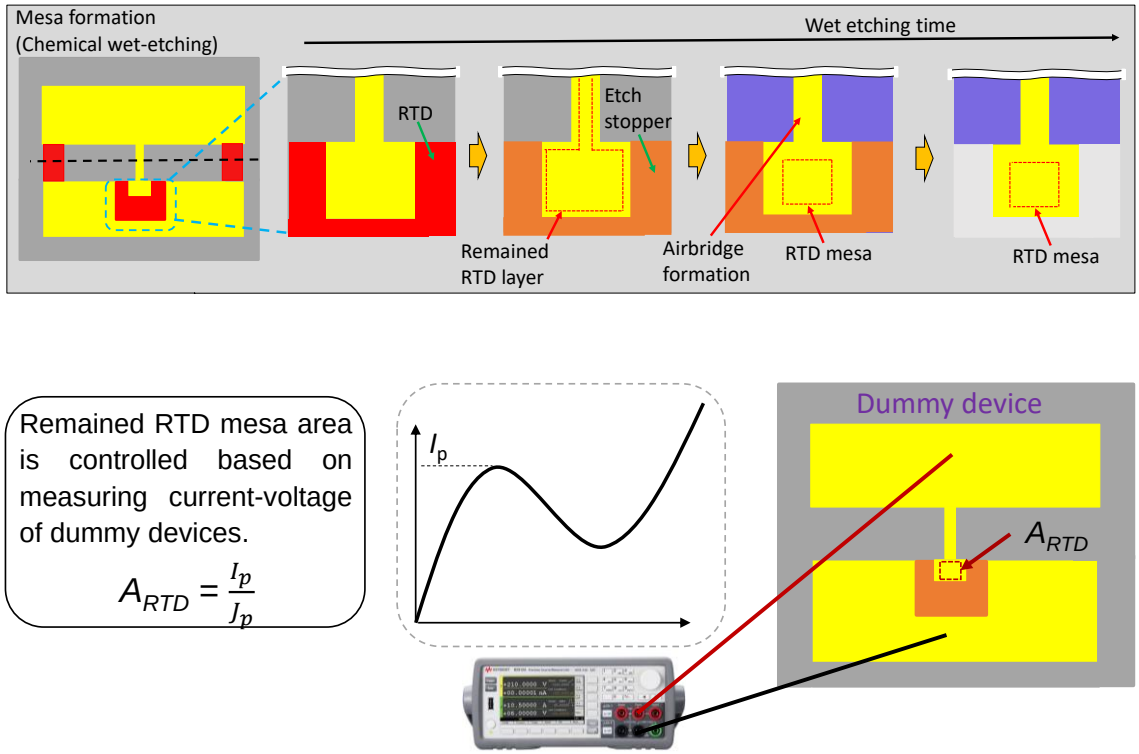


Fig. 2.4.2.2 (c) Fabrication process of the structure-simplified RTD oscillator.

A bi-layer resist stack was spin-coated on the surface of the well-cleaned RTD wafer. The resist stack consists of PMGI SF9 as the bottom layer and ZEP520 as the top layer with thicknesses of 650 and 500 nm, respectively. To obtain these thicknesses, the rotation speed and time were set to 2500 rpm and 60 s for the PMGI SF9 resist, and 2000 rpm and 60 s for the ZEP520 resist. The coated resists were then exposed using a JBX 6300 electron beam system (JEOL). The electron beam exposure was followed by the development to form the device pattern. The ZEP520 resist was developed using Xylene developer for 3 min; the PMGI SF9 resist was then developed using MFCD 26 developer for 45 s. Before vacuum evaporation, to obtain a good surface contact, the wafer surface was treated in HCl:$H_2O_2$ (1:5) for 2 min.

Vacuum evaporation was then conducted via Ti/Pd/Au (20/20/500 nm) multilayer metallization to obtain the RTD metal mask and electrodes. This type of metallization guarantees low contact resistance and good adhesion to the wafer surface. It should be noted that the upper electrode, lower electrode, and air-bridge were formed all at once. After vacuum evaporation, the resists were lifted off using a ZDMAC remover. As mentioned above, a bi-layer resist stack was employed to prevent the metal from depositing onto the sidewalls of the resist, thus facilitating the lift-off process.

After that, to form a resist mask for the dry-etching process, the second electron beam exposure was carried out followed by resist development. The resist mask for dry-etching was composed PMGI SF6 as the bottom layer and ZEP520 as the top layer with thicknesses of 350 and 500 nm, respectively. This time PMGI SF6 was employed instead of PMGI SF9 as the bottom layer for the small undercut that is desired the during dry-etching process.

Then, reactive-ion-etching (RIE) that is also called dry-etching (RIE-10NR, SAMCO, Japan) was employed to partly create the slot antenna and stabilization resistors. For dry-etching, $H_2$ and $CH_4$ gases were utilized. The detailed recipe for dry-etching is provided in the appendix. After the dry-etching process, the resist mask was removed using a ZDMAC remover. However, at this stage, the slot antenna still has not been completely formed yet because semiconductor layers under the air-bridge still remained.

Thus, in the next fabrication step, chemical wet-etching by a $H_2SO_4$: $H_2O_2$: $H_2O$ (1:1:80) etchant was employed. By using wet-etching, semiconductor layers under the air-bridge can be etched completely owing to lateral etching. In addition to this, the desired RTD mesa area was also obtained by wet-etching at the same time as removing

semiconductor layers under the air-bridge. For that purpose, the width of the RTD electrode was made wider than that of the air-bridge.

During the wet-etching process, the remaining area of the RTD mesa was controlled based on measuring currents flowing through dummy devices as illustrated in Fig.2.4.2.2 (c). For each design of an RTD mesa, four dummy devices, which have the same dimensions as that of a real RTD oscillator, were employed. The only difference is that stabilization resistors at both ends of the slot antenna were eliminated from the dummy devices. By measuring the current-voltage characteristic of the dummy devices, one can know the average value of the peak currents $I_p$ corresponding to the NDR region in the current-voltage characteristic of RTD. Thus, the remaining mesa area of the RTD is estimated as the ratio of the average peak current $I_p$ to the current density $J_p$. Moreover, the etch stopper layer ensures that the $n^+$ InGaAs layer is protected during mesa formation. Without an etch stopper layer, the $n^+$ InGaAs layer would be unexpectedly etched before obtaining the desired RTD mesa area.

In summary, it required twice electron beam exposure, once metal evaporation, and once dry-etching to fabricate the proposed RTD oscillator. Compared to the fabrication process of the conventional one described above in section 2.2, clearly, the fabrication process of the structure-simplified RTD THz oscillators is significantly simpler and less time-consuming.

The proposed structure-simplified RTD THz oscillator was fabricated successfully. The microphotograph and SEM image of a fabricated oscillator are shown in Fig. 2.4.2.3(a, b), respectively. As shown, there is no $n^+$ InGaAs layer under the air-bridge, and the slot antenna exhibits a good shape. Thus, although the fabrication process was simple, the proposed structure-simplified RTD THz oscillator was fabricated

successfully. Owing to the simple structure, the structure-simplified RTD oscillator can be easily expanded into various planar array configurations that could enable a wide range of THz applications.

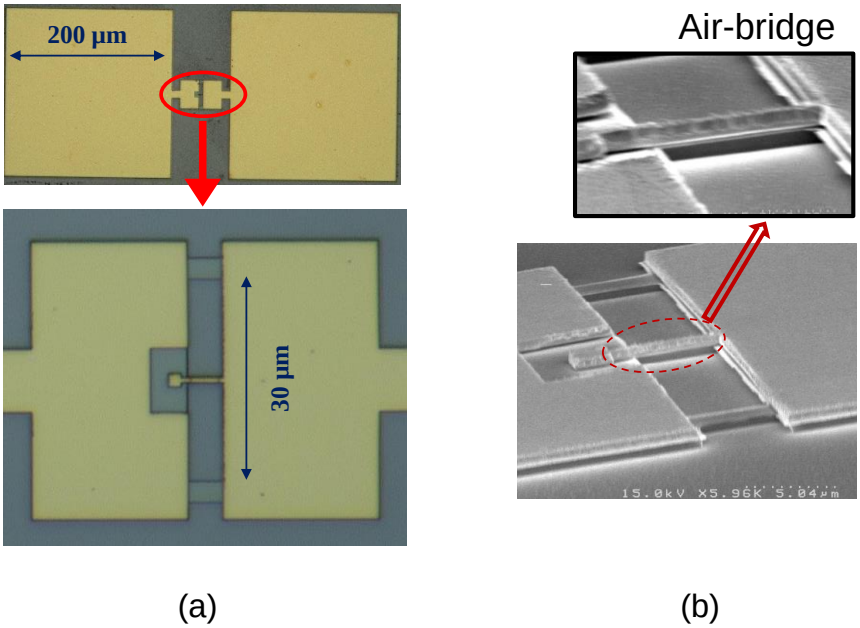


Fig. 2.4.2.3 (a) Microphotograph and (b) SEM image of a fabricated structure-simplified RTD THz oscillator.

# 2.5 Experimental results and discussions

In the initial experiment, the physical dimensions including the antenna length, slot antenna width, and stabilization resistor width were 30 μm, 5 μm and 2 μm, respectively. Such dimensions were also consistent with those used for structure simulation shown in Fig.2.4.1.3. The operation of the proposed structure-simplified RTD THz oscillator was validated by experimental results that are given below.

The oscillation frequency was measured using a Fourier transform infrared spectrometer with a liquid He-cooled bolometer as the detector. The lock-in measurement technique was used to reduce the surrounding noise. The RTD parameters for the theoretical calculations were estimated as follows. From the measured *J*–*V* characteristic shown in Fig. 2.4.2.1(b), the following RTD parameters were estimated: the peak current density $J_P$ = 8 mA/μm$^2$, peak-to-valley current density difference $\Delta J$ = 4.2 mA/μm$^2$, peak-to-valley voltage difference $\Delta V$ = 0.4 V, and peak-to-valley current ratio (*PVCR*) = 2.1. Based on the above parameters, the RTD negative differential conductance at the DC, can be estimated $G_{rtd}(0)$ = 10.5 mS/μm$^2$. Other parameters of the RTD were the geometrical capacitance $C_0$, transit time $\tau_{dep}$, and tunneling time $\tau_{RTD}$, their values are 3.3 fF/μm2, 25 fs, and 25 fs, respectively. These parameters were extracted by fitting the theoretical curve with the measured data.

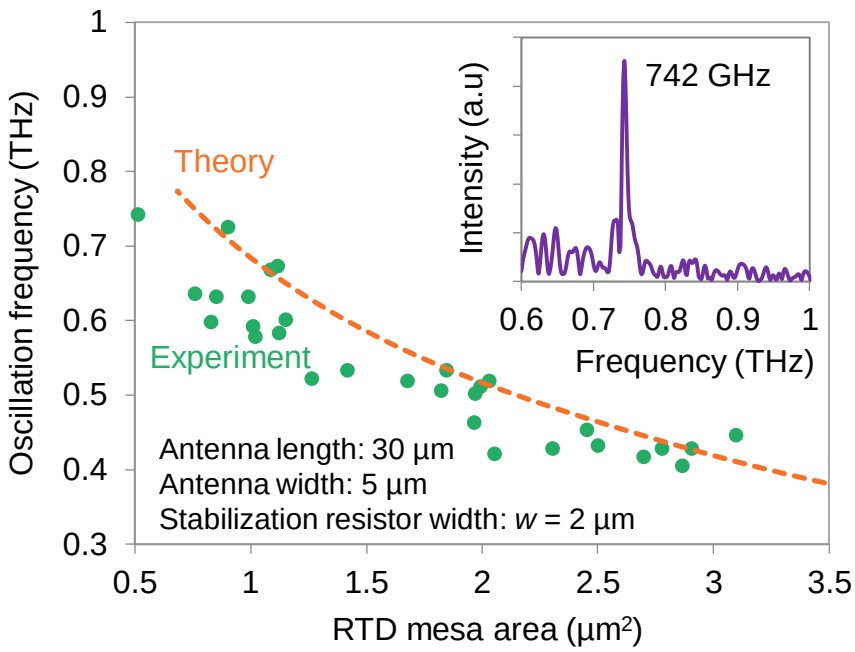


Fig. 2.5.1 Oscillation frequency as a function of RTD mesa area.

The oscillation frequency as a function of the RTD mesa area is shown in Fig.2.5.1. In the experiment, measured oscillation frequencies from 405 GHz up to 742 GHz were obtained. It can be seen that oscillation frequency increased with reducing RTD mesa area owing to the decrease in the RTD capacitance. The highest measured oscillation frequency of 742 GHz corresponded to an RTD mesa area of ~0.5 μm$^2$. The oscillation spectrum at 742 GHz is shown in the inset. Although measured results roughly agreed with theoretical calculations, a distribution of oscillation frequency was also observed. The possible reason for this is the variation of stabilization resistors. According to formula (2.3.4), an increase in stabilization resistor $R_{sup}$ causes a decrease in oscillation frequency.

To experimentally validate this effect, the RTD mesa and slot areas of a fabricated RTD oscillator were covered with a ma-N 1405 resist. The physical parts of the stabilization resistors were etched using chemical wet etching to increase the $R_{sup}$ value. Then the oscillation frequency change was measured at every wet-etching step while maintaining the RTD mesa area and antenna length. The method to estimate the $R_{sup}$ value is as follows. The current-voltage characteristic of the fabricated RTD oscillator was measured after each etching step. Finally, the stabilization resistors were completely etched, and the current-voltage characteristic of only the RTD was measured. Hence, one can derive the current flowing through the stabilization resistors and estimate the $R_{sup}$ value at each etching step by subtracting the current-voltage characteristic of only the RTD from that of each step. Fig. 2.5.2 shows the dependence of the oscillation frequency on $R_{sup}$. It can be seen that the oscillation frequency decreases with an increase in $R_{sup}$, and the experiment results are in good agreement with the theory. This result also implies that an increase in the oscillation frequency is possible using a small $R_{sup}$. However, as mentioned above in the previous section reducing $R_{sup}$ results in an increase in the DC

power consumption because of the large current. Such a trade-off between the oscillation frequency and power consumption should be considered during the design phase. Moreover, experiments reveal that heat destruction occurred with $R_{sup}$ ~ 6 Ω due to high DC current flowing. Thus, in this study, the stabilization resistor value was selected ~ 10 Ω for small degradation of oscillation frequency, and avoiding heat destruction.

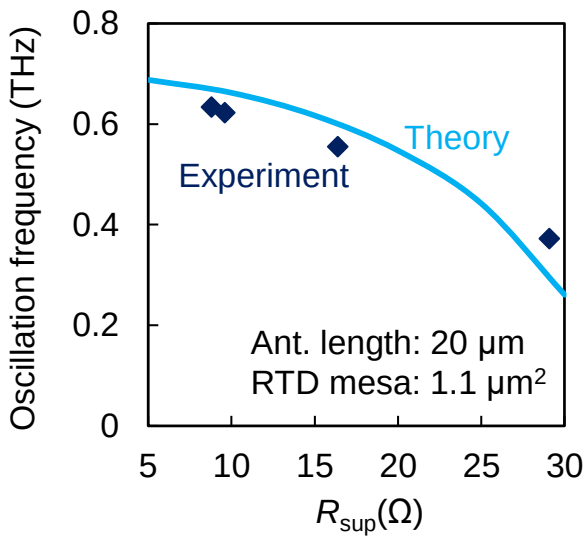


Fig. 2.5.2 Dependence of oscillation frequency on stabilization resistor.

To measure the output power, we placed the RTD device chip on a hemispherical Si lens (with a 30-mm diameter). The radiated THz wave of the RTD oscillator was collected using a parabolic mirror and converted into a collimated beam. The collimated THz wave was then reflected by another parabolic mirror and focused on the horn antenna of a PM5 power meter (Virginia Diodes). Because a relatively broad radiation pattern was obtained from the RTD device, it is obvious that only a certain portion of the output power was caught by the parabolic mirror. To estimate the ratio of radiated output power caught by the parabolic mirror, we simulated the radiation pattern for each frequency by HFSS and

calculated the integral of the radiation pattern by considering the collectable angle of the parabolic mirror. The propagation loss was mostly negligible in this setup because the propagation length in the measurement was short (< 20 cm). Fig. 2.5.3 shows the output power radiated from the RTD oscillator, which was corrected using the caught power ratio as a function of the oscillation frequency. The theoretical output power was calculated using Eq. (2.1.5). The tendency of measured output powers agreed well with the theoretical calculations.

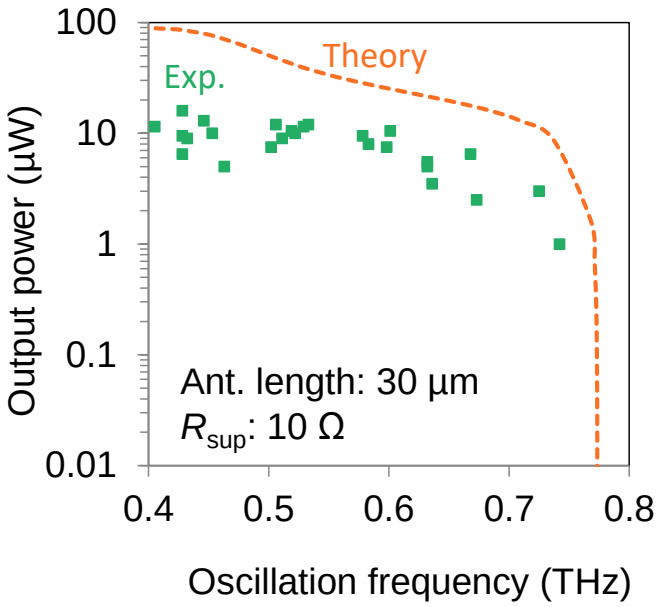


Fig. 2.5.3 Output power as a function of oscillation frequency.

Fig. 2.5.3 shows the output power radiated from the RTD oscillator as a function of the oscillation frequency. As shown, the measured output power is ~10 μW for frequencies up to ~600 GHz. It was reported that conventional RTD oscillators exhibited output powers of ~ 20 μW at the 600 GHz range [2.9]. Therefore, the output power level of the structure-simplified RTD oscillator can be considered comparable, although

slightly smaller, to that of the conventional RTD oscillator. The output power rapidly decreases as the oscillation frequency approaches the frequency limit because the RTD negative conductance cannot compensate for the antenna loss conductance. Although the tendency of the measured output power of the fabricated devices agreed well with the theoretical curve, the measured output powers were lower than the calculated ones. This could be due to several following reasons. The first one is the disagreement between the actual and assumed radiation patterns of the fabricated RTD oscillators. The second possible reason is caused by the misalignment of the optical measurement setup. The third one is the low conductivity of the actual deposited metal, which results in higher conduction loss and therefore lower output power. And last but not least, another possible one is the bad surface roughness of the actual deposited metal which also gives rise to the increase in the conduction loss.

## 2.6 Conclusions

A novel RTD oscillator was proposed and analyzed. The operation of the proposed device was experimentally validated. The proposed RTD oscillator has a structure simpler than that of the conventional RTD oscillator owing to eliminating MIM capacitors. An RTD epitaxial layer structure with an etch stopper layer, which is specifically employed for the easy formation of an air-bridge, was also presented. Novel RTD oscillators were successfully fabricated using a significantly simpler fabrication process compared to that of conventional RTD oscillators. The fabrication process was significantly simplified owing to the simple structure and introduction of the etch stopper layer. In the primary experiment, oscillation frequencies from 405 GHz to 742 GHz were obtained. The output

power was ~10 μW at frequencies up to ~600 GHz. The oscillation frequency and output power can be further enhanced by structure optimization which is carried out in the next chapter. Owing to the simplified fabrication process, the novel RTD oscillator structure is expected to be suitable for massive array configurations that could enable a wide range of practical THz applications.

# Chapter 3
# Structure optimization for high output power and high frequency

# 3.1 Introduction

In Chapter 2, a structure-simplified RTD THz oscillator was proposed and validated operation by experimental results. The proposed RTD THz oscillator eliminates the metal–insulator–metal (MIM) capacitor, which is typically used in conventional RTD oscillators for DC and RF separation. Such a simple RTD oscillator can be fabricated within a short period of time using a simple fabrication process, which results in small characteristic variations and high yields. In the primary experiment, the highest oscillation frequency and output power of these simple RTD oscillators were 742 GHz and ~10 μW, respectively.

In this chapter, the dependence of the oscillation characteristics on the device structure is examined. The effect of the resistance and inductance of the air-bridge is discussed. A further increase in the oscillation frequency of up to ~1 THz was obtained by optimizing the slot antenna length. By using split ring resonator(SRR) instead of the slot resonator, the highest oscillation frequency reached 1.22 THz owing to low loss characteristic of the SRR. Moreover, although an offset-fed slot antenna structure [3.1-3.3], which is usually employed in conventional RTD oscillators, is effective for a high output power owing to its high radiation conductance and efficiency, it has yet to be applied to simple RTD oscillators. Therefore, an offset-fed slot antenna is adopted for the structure-simplified RTD oscillator. Output power was significantly enhanced compared to that achieved with RTD oscillators in the previous chapter. The highest output power of ~220 μW was achieved at 500 GHz.

# 3.2 Effect of the air-bridge dimensions

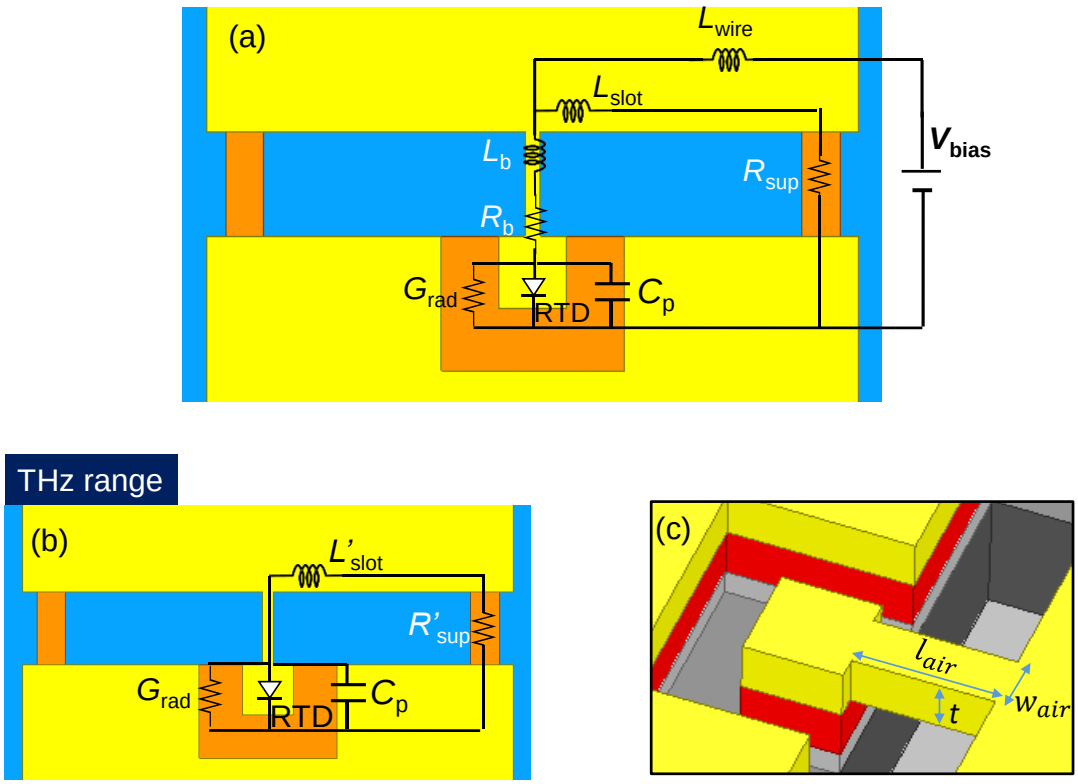


$L'_{slot}=L_{slot}+L_b$

$R'_{sup}=R_{sup}+R_b$

Fig. 3.2.1. (a) Detailed equivalent circuit including resistance and inductance of the air-bridge. (b) Equivalent circuit in the THz range. (c) Dimensions of the air-bridge.

In the equivalent circuits of the structure-simplified RTD oscillator shown in Fig.2.4.1.2 in Chapter 2, the resistance and inductance of the air-bridge were not shown for simplicity. The detailed equivalent circuit including the resistance and inductance of the air-bridge is shown in Fig.3.2.1(a). In the THz range, air-bridge resistance and inductance are connected in series with $L_{slot}$ and $R_{sup}$, and this equivalent circuit can be

transformed into a circuit shown in Fig.3.2.1(b), which has the similar form to the one shown in Fig.2.4.1.4. Where $L'_{\text{slot}} = L_{\text{slot}} + L_b$ and $R'_{\text{sup}} = R_{\text{sup}} + R_b$. This implies the resistance and inductance of the air-bridge lead to an increase in the resistance and inductance of the whole antenna structure. However, it is worth to emphasizing that the calculated results shown in Chapter 2 are not changed because that resistance and inductance were taken into account by HFSS simulation. Because the resistance and inductance of the air-bridge are determined by its dimensions, the effect of the air-bridge dimensions on the oscillation characteristics is discussed here.

Three dimensions of the air-bridge are length $l_{\text{air}}$, width $w_{\text{air}}$, and thickness $t$ as shown in Fig.3.2.1(c). The following formulas can be used to estimate the resistance and inductance [3.4] of the air-bridge

$$R_b = \frac{\rho . l_{\text{air}}}{t \cdot w_{\text{air}}} \tag{3.2.1}$$

$$L_b = 0.2 \cdot l_{\text{air}} \cdot \left( ln \frac{2 l_{\text{air}}}{w_{\text{air}} + t} + 0.5 + \frac{w_{\text{air}} + t}{3 l_{\text{air}}} \right) \ (\mu\text{H}) \tag{3.2.2}$$

Where $\rho \approx 2.44 \cdot 10^{-8} \Omega \cdot \text{m}$ is the resistivity of gold.

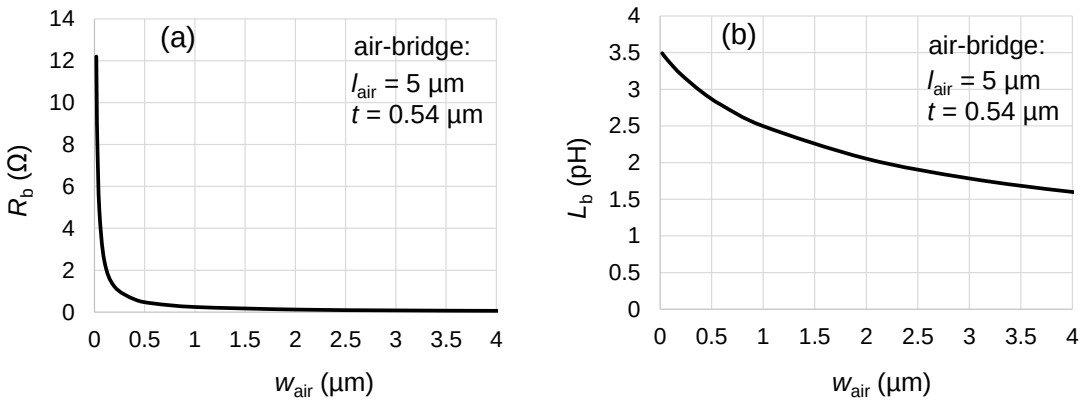


Fig. 3.2.2. Dependence of the (a) resistance and (b) inductance of the air-bridge on its width.

To easily form the air-bridge structure during wet-etching, the air-bridge width has to be small enough (that was 0.6 μm for fabricated oscillators). By reducing the air-bridge width, the resistance and inductance of the air-bridge will increase as illustrated in Fig. 3.2.2, which in turn could have effect on the oscillation characteristics of the RTD oscillator.

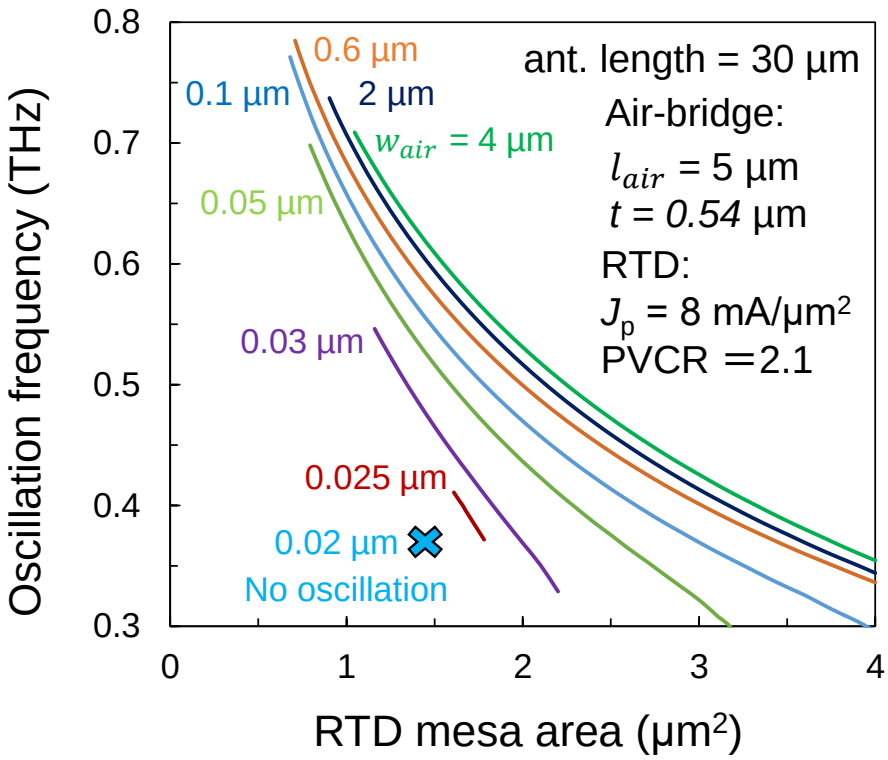


Fig. 3.2.3. Effect of the air-bridge width on oscillation frequency.

In order to understand how oscillation frequency is changed with the air-bridge width, oscillation frequency was calculated for various widths of the air-bridge as shown in Fig. 3.2.3. It is found that with reducing the width of the air-bridge, the oscillation frequency range becomes narrower. This is because $R_b$ and $L_b$ increase, resulting in higher inductance and consequently higher conduction loss of the whole antenna structure. When

the air-bridge width $w_{air}$ formally equals to 0.025 μm, the oscillation frequency range becomes very small. And no oscillation can be obtained with $w_{air}$ = 0.02 μm, which can be considered as the limit for the size of the air-bridge width. Fabricated oscillators employed air-bridge having length, width, and thickness of 5, 0.6, and 0.54 μm, respectively. Hence, the resistance and inductance of the air-bridge were estimated $R_b$ = 0.4 Ω, and $L_b$ = 2.7 pH, respectively. While the stabilization resistor $R'_{sup}$ and slot inductance $L'_{slot}$ were 10.4 Ω and 9.5 pH as extracted in the previous section, respectively. It is seen that with $w_{air}$ = 0.6 μm the resistance of air-bridge almost does not affect the resistance of the antenna structure, while the air-bridge inductance slightly increases the antenna inductance. Due to the increase in the antenna inductance, oscillation frequency is slightly smaller than that of the cases if a wide air-bridge of 2 or 4 μm is used. The air-bridge width $w_{air}$ = 0.6 μm was selected because of easy formation of the air-bridge, small decrease in oscillation frequency, and high oscillation frequency limit.

# 3.3 Structure optimization for high oscillation frequency

### 3.3.1. Optimum antenna length for high oscillation frequency

As derived in the previous chapter, oscillation occurs if the RTD negative conductance can compensate for the losses of the antenna structure

$$G_{\mathrm{rtd}} > G_{\mathrm{rad}} + G_{\mathrm{loss}} \tag{3.3.1}$$

The oscillation frequency of a simple RTD oscillator is determined through the resonance of the $LC$ tank, including $L$, $C_{rtd}$, and $C_p$, as follows:

$$f_{\mathrm{osc}} = \frac{1}{2\pi}\sqrt{\frac{1}{L_{\mathrm{slot}}(C_{\mathrm{p}}+C_{\mathrm{rtd}})} - \frac{R_{\mathrm{sup}}^2}{L_{\mathrm{slot}}^2}} \ . \tag{3.3.2}$$

Because the former component inside the square root is dominant and $C_{\mathrm{rtd}}$ is much larger than $C_{\mathrm{p}}$, the oscillation frequency is roughly determined by the $LC$ resonance of $C_{\mathrm{rtd}}$ and $L_{\mathrm{slot}}$, and an increase in frequency is possible using a short antenna with a small $L_{\mathrm{slot}}$.

RTD oscillators with antenna lengths of 15 and 20 μm, which were shorter than those used in the previous chapter (30 μm), were fabricated. The fabrication process of RTD oscillators in this experiment is similar to that of the ones described in the section 2.4 in the previous chapter. Fabricated devices were then characterized by measuring oscillation frequency. The measured result is shown below.

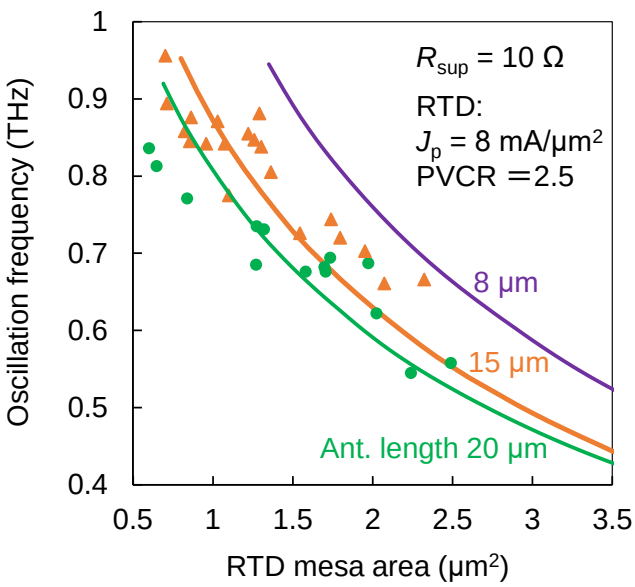


Fig. 3.3.1.1 Oscillation frequency as a function of RTD mesa area for various antenna lengths.

Fig. 3.3.1.1 shows the oscillation frequency as a function of the RTD mesa area for various antenna lengths. The peak current density, voltage width of NDC region $\Delta V$, and peak-to-valley current ratio (PVCR) of the RTD were 8 mA/μm$^2$, 0.45 V, and 2.5, respectively. The stabilization resistor, $R_{sup}$, was the same as that in the primary experiment and approximately 10 Ω. The measured results agreed well with the theoretical calculations. It can be seen that the oscillation frequency increases with a decrease in antenna length while maintaining the same RTD mesa area. The highest measured oscillation frequencies of 836 and 956 GHz were obtained with antenna lengths of 20 and 15 μm, respectively. The oscillation spectrum at the highest oscillation frequency is shown in Fig. 3.3.1.2.

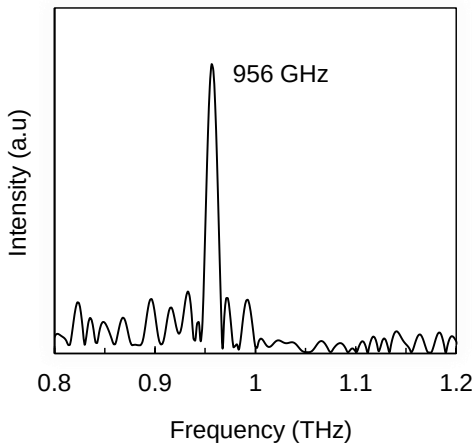


Fig. 3.3.1.2 Oscillation spectrum of a fabricated device oscillating at 956 GHz.

However, it is worth noting that the oscillation frequency cannot be infinitely increased by simply reducing the antenna length, as illustrated by the theoretical curve of the 8-μm long antenna, which has a smaller frequency limit, as shown in Fig. 3.3.1.1. The

reasons for this can be explained using the real part of oscillation condition Eq. (3.3.1) as follows. At around the frequency limit of ~1 THz, $\omega L_{slot}$ becomes large, and an approximation of $R_{sup} \ll \omega L_{slot}$ is roughly established. Using the approximation, the oscillation frequency is rewritten as $1/(2\pi\sqrt{L_{slot}C_{rtd}})$. Since the $L_{slot}$ is proportional to antenna length, by employing a short antenna length, a large $C_{rtd}$ due to increasing RTD area can be used while maintaining the oscillation frequency. Therefore, $G_{rtd}$ is inversely proportional to the antenna length under the fixed frequency condition. Using the approximation also for $G_{loss}$, $G_{loss} \approx R_{sup}/(\omega^2 L_{slot}^2)$, and thus $G_{loss}$ is inversely proportional to the square of the antenna length. It is also noted that $G_{rad}$ is proportional to the square of antenna length. Consequently, the oscillation margin, i.e. the left term of Eq. (3.3.1), is a convex upward function for the antenna length and has a maximum at a certain antenna length as illustrated in Fig.3.3.1.3(a). As can be seen, Eq. (3.3.1) is satisfied in a certain range for the antenna length.

With increasing oscillation frequency by reducing RTD area, although $G_{loss}$ decreases, $G_{rad}$ increases and $G_{rtd}$ decreases, resulting in a decrease in the oscillation margin $G_{rtd}$ - $G_{loss}$ - $G_{rad}$ as can be seen in Fig. 3.3.1.3(b). Hence, the convex upward function corresponding to the left term of the Eq. (3.3.1) goes down. As a result, the range for the antenna length satisfying Eq. (3.3.1) is reduced, the optimum antenna length for maximizing the oscillation margin still exists. With further increasing oscillation frequency, the range becomes very small and the optimum antenna length for the highest frequency limit is determined uniquely.

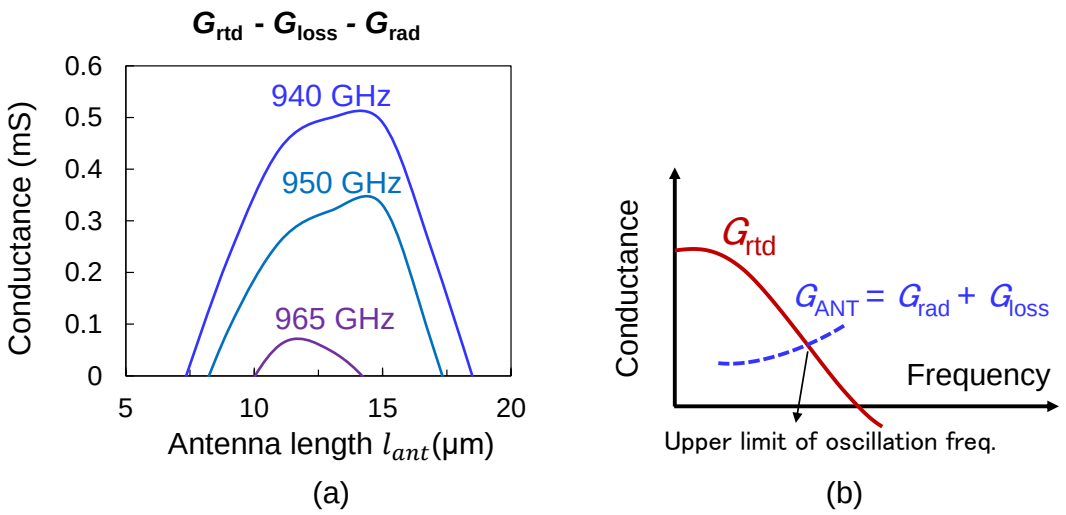


Fig. 3.3.1.3 (a) Illustration of oscillation margin for various oscillation frequencies. (b) Upper limit of oscillation frequency.

### 3.3.2. High oscillation frequency by using low loss split ring resonator

As mentioned above, the frequency limit can be enhanced by reducing the conduction loss $G_{loss}$. In this section, an increase in the frequency limit is demonstrated by using a low loss split ring resonator (SRR) instead of the slot resonator. The structure of the RTD oscillator integrated with a SRR is shown in Fig.3.3.2.1.

In this RTD oscillator, the RTD mesa is incorporated into the center of the SRR. It is found that a SRR exhibits lower loss than a slot resonator having the same perimeter. That can be explained by the electric field confinement as illustrated in Fig.3.3.2.2(a, b). The electric field is strongly confined at the center of the SRR. The electric field confinement area of the SRR is also smaller than that of the slot resonator.

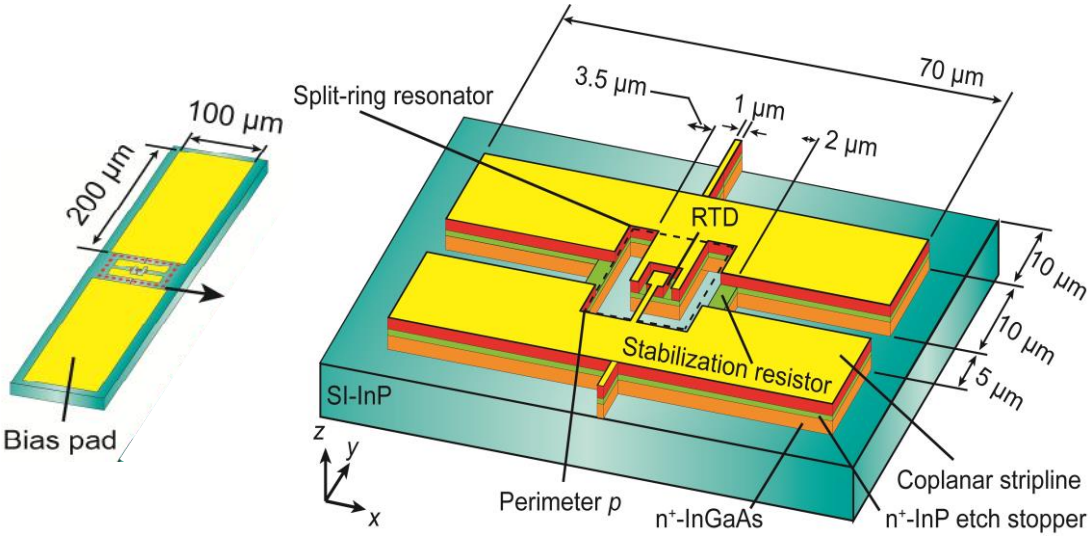


Fig. 3.3.2.1 RTD THz oscillator integrated with a split ring resonator.

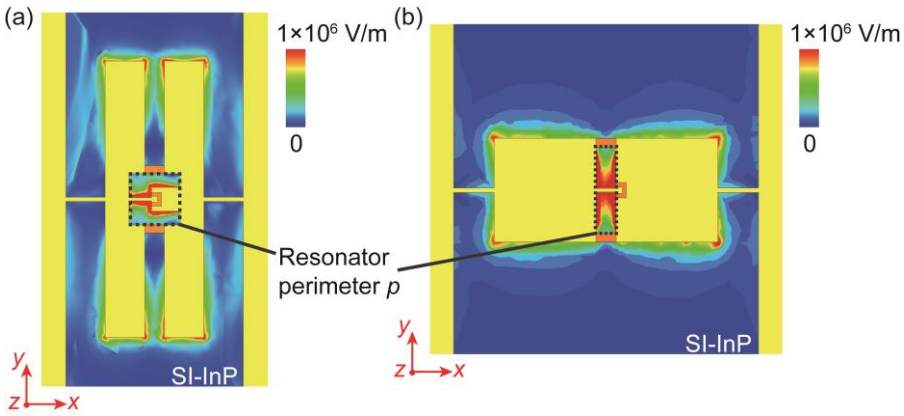


Fig.3.3.2.2. Electric field intensity distribution at 1 THz obtained for (a) SRR and (b) slot resonator.

This conclusion is consistent with the quantitative estimation of the quality factor for the SRR and the slot resonator as shown in Fig.3.3.2.3. In general, the SRR has greater Q factor than that of the slot resonator. Therefore, the SRR has smaller loss than the slot resonator. The RTD THz oscillator integrated with the SRR was fabricated successfully.

The microphotograph of a fabricated device is displayed in Fig.3.3.2.4(a). In this experiment, the highest oscillation frequency of 1.22 THz was achieved as shown in Fig, 3.3.2.4(b).

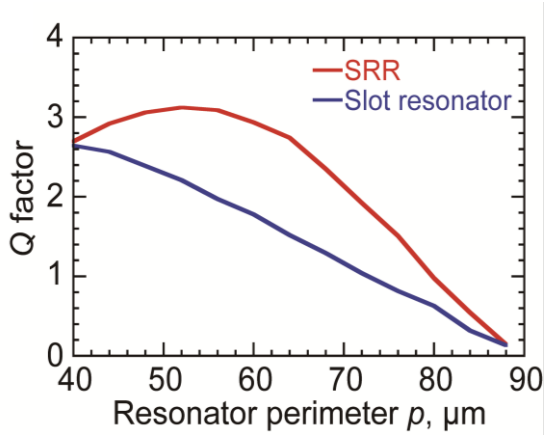


Fig.3.3.2.3. Calculator Q factor of SRR and slot resonator.

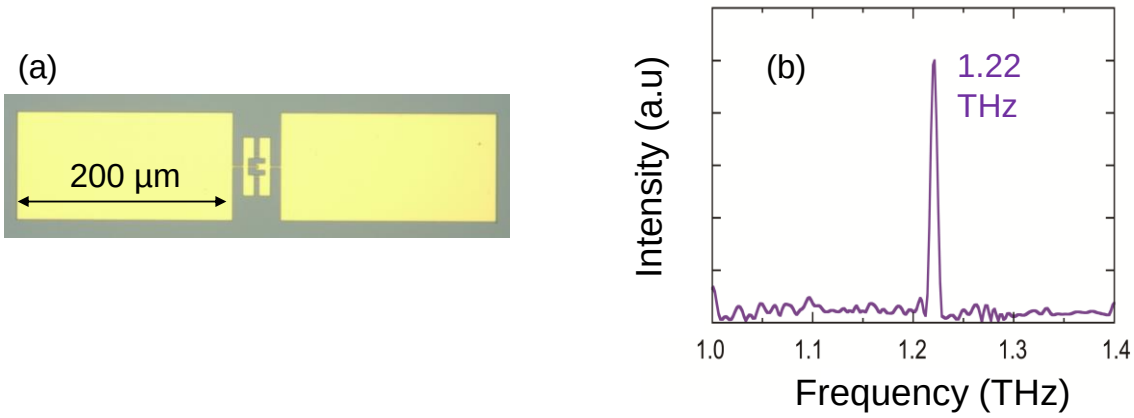


Fig.3.3.2.4. (a) Fabricated RTD THz oscillator integrated with SRR. (b) Oscillation spectrum at 1.22 THz.

# 3.4 Structure optimization for high output power

In Chapter 2, the formula for output power of an RTD oscillator was derived. It is given below again to make it easy to follow.

$$P_{\mathrm{out}} = \frac{1}{2}\frac{G_{\mathrm{rad}}}{a}(a - G_{\mathrm{loss}} - G_{\mathrm{rad}}) \cdot \Delta V^2. \tag{3.4.1}$$

From Eq. (3.5), the maximum output power $P_{\mathrm{out}}$ is satisfied under the condition of $G_{\mathrm{rad}} = (a - G_{\mathrm{loss}})/2$. Substituting the matching condition into Eq. (3.5), we get the maximum output power as

$$P_{\mathrm{out.max}} = \frac{1}{8}\frac{(a - G_{\mathrm{loss}})^2}{a} \cdot \Delta V^2. \tag{3.4.2}$$

According to Eqs. (3.3.1) and (3.4.2), under the matching condition, $G_{\mathrm{loss}}$ is the limiting factor for both the oscillation frequency and output power. In Chapter 2, fabricated structure-simplified RTD oscillators employed a structure called center-fed slot, where the RTD is incorporated into the center of the slot. To achieve oscillation in THz range, the inductance of the slot antenna has to small, thus slot antennas were kept relatively short compared to that of the wavelength of the radiated THz waves, resulting in a low radiation conductance $G_{\mathrm{rad}}$ of antenna structures. Hence, the center-fed RTD oscillator cannot satisfy the above matching condition due to the small radiation conductance $G_{\mathrm{rad}}$, which results in a low output power.

An approach to improve the output power is to enhance the radiation conductance $G_{\mathrm{rad}}$ using an offset-fed slot antenna, which is usually employed in conventional RTD oscillators for a high output power. In this section, an offset-fed slot for structure-simplified RTD oscillators is adopted. Moreover, coplanar stripline (CPS) antennas are

formed at the external ends of the stabilization resistors to further increase the radiation conductance [3.4]. Owing to the enhancement of the radiation conductance, increase in output power is expected for structure-simplified RTD oscillators employing offset-fed slot structure.

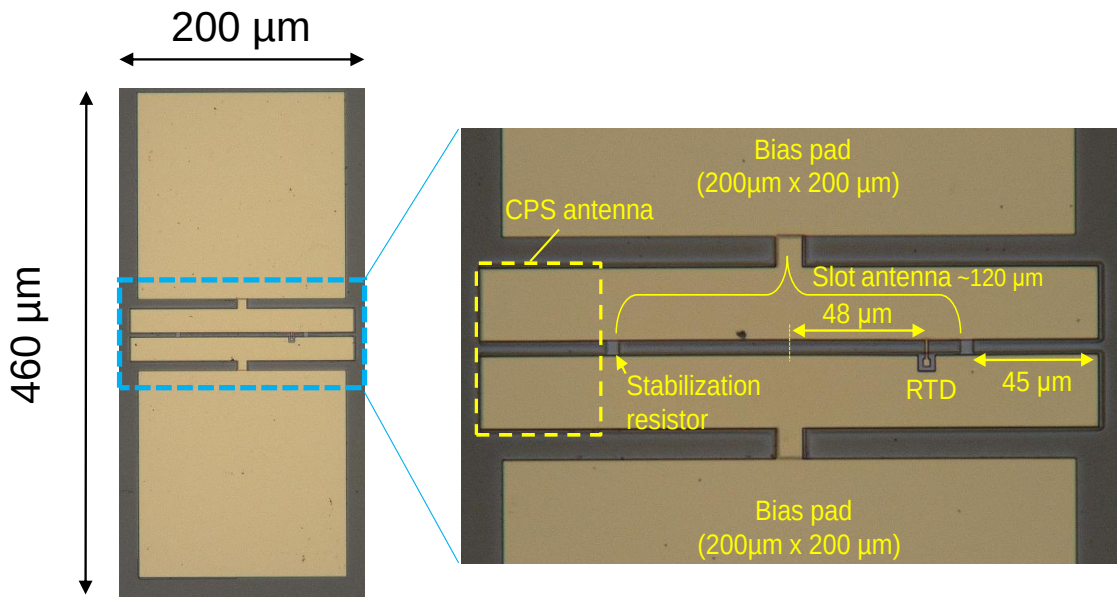


Fig. 3.4.1 Structure-simplified RTD oscillator with an offset-fed slot.

Fig. 3.4.1 shows a microphotograph of fabricated RTD oscillator with an offset-fed slot combined with CPS antennas. The RTD is shifted by 48 µm from the center of the slot antenna with a length of 120 µm.

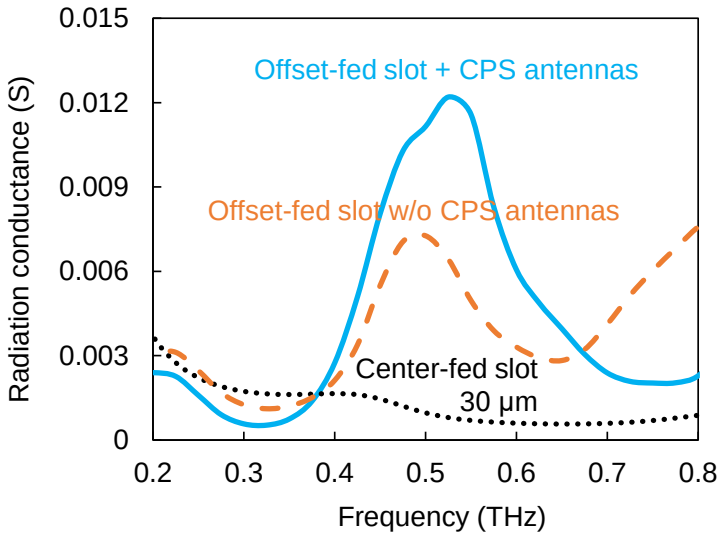


Fig. 3.4.2 Comparison of radiation conductance between offset-fed structure combined with CPS antennas, offset-fed structure without CPS antennas, and center-fed structure.

Fig. 3.4.2 shows the radiation conductance $G_{rad}$ of the antenna structure viewed from the RTD for the simple RTD oscillator for three cases. The dotted curve corresponds to the center-fed structure with an antenna length of 30 μm, used in the primary experiment. The radiation conductance of the offset-fed slot structure with and without CPS antennas are plotted by the solid and dashed lines, respectively. Those radiation conductances were calculated using a 3D electromagnetic simulator (Ansys HFSS), where the RTD is replaced by a lumped port. From Fig. 3.4.2, it can be seen that the radiation conductance of the offset-fed structure is several times higher than that of the center-fed one within the frequency range of approximately 500 GHz. By adding the CPS antennas, the radiation conductance is further increased. Thus, a higher output power in 500 GHz frequency range is expected for an RTD oscillator employing an offset-fed slot combined with CPS antennas. The CPS antennas have little effect on the oscillation frequency, because the susceptance of CPS antenna is much smaller than that of slot antenna [3.5].

By scaling the offset-fed and CPS designs, the radiation conductance peak shifts to higher frequency range, and increase in output power at high frequency is possible. However, approaching to the oscillation limit, the device structure becomes close to the normal center-fed structure. This is because this high-power structure enables achieving matching condition, but, at around the frequency limit, the oscillation margin becomes almost zero and increment in $G_{rad}$ cannot be adopted.

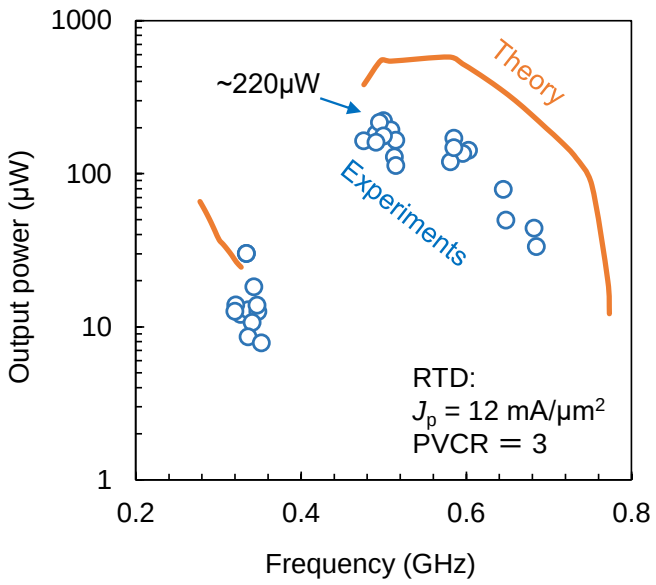


Fig. 3.4.3 Output power as a function of oscillation frequency of RTD oscillator with offset-fed structure combined with CPS antennas.

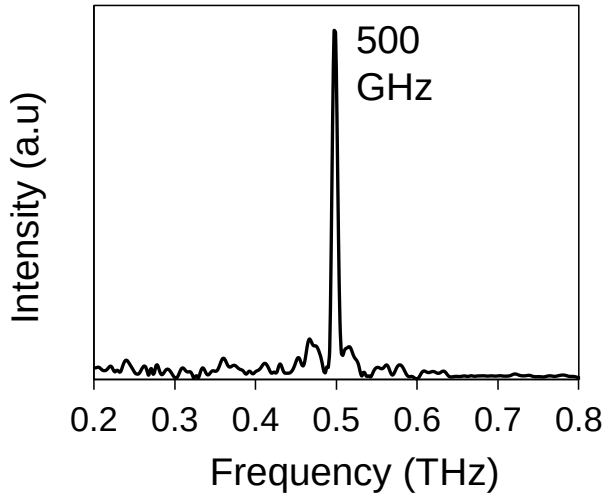


Fig. 3.4.4 Oscillation spectrum of a fabricated device.

In the experiment conducted on an offset-fed slot combined with CPS antennas, an RTD with a high peak current density $J_p$ was employed to increase the output power. The peak current density, voltage width, and PVCR of the RTD used in this experiment were 12 mA/μm$^2$, 0.45 V, and 3, respectively. The proposed structure was fabricated successfully. Fabricated devices were then characterized by the measurements of oscillation frequency and output power. The measurement setups were the same as those described in Chapter 2. Experimental results are discussed below.

Fig. 3.4.3 shows the output power radiated from the RTD oscillator, which was corrected using the caught power ratio as a function of the oscillation frequency. The theoretical output power was calculated using Eq. (3.4.1). The tendency of measured output powers agreed well with the theoretical calculations. The highest measured output power of ~220 μW was obtained at 500 GHz, which matches the peak of the simulated radiation conductance, as shown in Fig. 3.4.2. The oscillation spectrum of a fabricated oscillator is given in Fig.3.4.4. The dispersion in the experimental output power was likely

caused by the variations in the peak current density $J_p$, voltage width $\Delta V$, and PVCR in the current–voltage characteristics of each oscillator. These variations are attributed to the deviation of the thin spacers, barriers, and wells of the RTD during the epitaxial growth process. A non-oscillation gap at approximately 400 GHz was observed for both the measured and theoretical oscillation characteristics. The gap is caused by the double resonance of the slot and CPS antennas, and similar characteristics were obtained in a previous study [3.5].

# 3.5 Conclusions

In this chapter, oscillation characteristics of structure-simplified RTD oscillators were investigated. The oscillation frequency was increased up to 956 GHz with an optimized short antenna length of 15 μm. By using a low-loss split-ring-resonator instead of the slot antenna, the highest oscillation frequency of 1.22 THz was also obtained. In addition to this, offset-fed slot antenna combined with CPS antennas was applied for the structure-simplified RTD THz oscillator for enhancing radiation conductance. Owing to high radiation conductance, high output power operation was obtained. In the experiment, the highest output power of ~220 μW was achieved at 500 GHz.

# Chapter 4
# Array configuration based on structure-simplified RTD oscillator

# 4.1 Introduction

Generally, the output power of a single RTD oscillator is relatively small of few to several tens μW [4.1-4.8]. To increase the output power of a single oscillator, it is effective to increase the current and voltage width of the negative differential conductance (NDC) region for the RTD [4.9-4.10] and impedance matching with the load of the antenna [4.11-4.12]. In addition to these methods for the single oscillator, an array configuration is effective for increasing output power. Our group reported a high output power of 0.7 mW at ~ 1 THz by using an 89-element arrayed RTD oscillator [4.13]. However, the elements were uncoupled and operated incoherently. Various studies on coherent power combining for oscillators that integrate two RTDs have been conducted [4.8, 4.11, 4.14-4.15]. In the multi-element array, very recently, a very high output power of ~ 12 mW at 450 GHz by a 36-element coherent arrayed RTD oscillator was reported by the Canon group [4.16]. In this way, a coherent output combination using coupled array operation becomes more important in the future. However, in the array operation, there are as many operation modes as there are integrated RTDs, and understanding the array device operation is difficult [4.17].

In this chapter, a simple and general method is proposed for identifying operating modes in arrayed oscillators. In addition, resistor-coupled RTD arrayed oscillators is proposed. The operation mode is then carefully analyzed in the case of a two-element arrayed oscillator. It is found that the odd-mode operation, where adjacent oscillators operate in the anti-phased condition, is stable. Then the analytical method is extended to a multi-element array of the general case. Based on the operation mode, the arrangement of array elements is modified, where slot antennas are connected at a right angle, for

obtaining power combination in the substrate direction. The proposed arrayed oscillator is fabricated and verified the odd-mode operation by measuring polarization characteristics. Coherent power combination in arrayed oscillators is also validated by oscillation frequency and output power measurements.

# 4.2 Theoretical derivation of operation modes for RTD arrayed oscillators

### 4.2.1. Single RTD oscillator

Before entering the analysis for RTD arrayed oscillator, the oscillation condition is derived for a single RTD oscillator with the simplified structure as displayed in Fig.4.2.1. The single RTD oscillator can be represented by a one-port network loaded by the RTD effective NDC $-G_{\mathrm{RTD}}$, where the one-port network accounts for the antenna structure and RTD capacitance. Given the admittance of the one-port network viewed from the RTD is $Y_{\mathrm{ant}}$. The voltage dropped on the port and current flowing through the port are $v_{\mathrm{osc}}$, and $i_{\mathrm{osc}}$, respectively. One obtains $i_{\mathrm{osc}} = \mathrm{v}_{\mathrm{osc}} \cdot Y_{\mathrm{ant}}$, and $i_{\mathrm{osc}} = v_{\mathrm{osc}} \cdot G_{\mathrm{RTD}}$. Thus, the circuit equation for the single oscillator can be derived as

$$(Y_{\mathrm{ANT}} - G_{\mathrm{RTD}}) \cdot v_{\mathrm{osc}} = 0. \tag{4.1}$$

From the circuit equation, the oscillation condition can be derived as $Y_{ANT} - G_{RTD} = 0$. Separating that condition for the real part and imaginary part, one obtains $\mathrm{Re}[Y_{\mathrm{ANT}}] = G_{\mathrm{RTD}}$ and $\mathrm{Im}[Y_{\mathrm{ANT}}] = 0$. The former condition gives the negative conductance of RTD required for oscillation, while the latter gives the oscillation frequency.

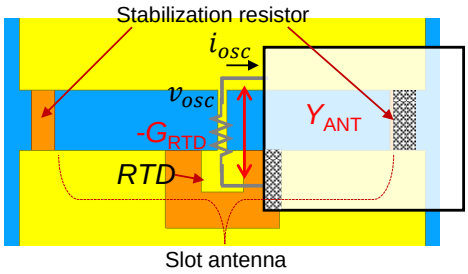


Fig. 4.2.1 Single structure-simplified RTD THz oscillator.

### 4.2.2. Two-element arrayed oscillator

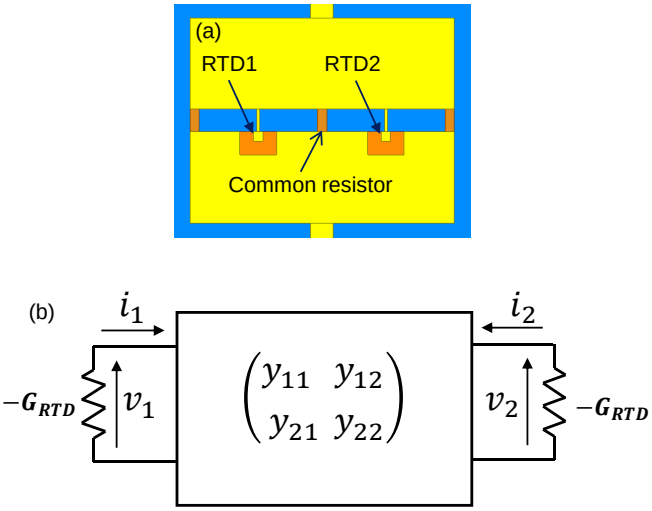


Fig. 4.2.2.1(a) Two-element RTD arrayed oscillator based on structure-simplified RTD oscillator. (b) Two-port network representation of (a).

Here, possible operation modes of a two-element arrayed oscillator are derived. The device structure and circuit model for the two-element array are shown in Fig.4.2.2.1(a, b). The arrayed oscillator is constructed based on the structure-simplified RTD oscillator. Each element includes an RTD, a slot antenna, and stabilization resistors. The arrayed elements are coupled to each other via a common stabilization resistor. Considering each

RTD as a port, the arrayed oscillator can be treated as a two-port network. All RTDs are assumed to be the same and have the same effective negative conductance $-G_{\mathrm{RTD}}$.

Given the voltage drops and flowing currents as $v_1$, $i_1$ for RTD1, and $v_2$, $i_2$ for RTD2, respectively, the relations between voltages and currents at the port are given by

$$\begin{pmatrix} i_1 \\ i_2 \end{pmatrix} = \begin{pmatrix} y_{11} & y_{12} \\ y_{21} & y_{22} \end{pmatrix} \begin{pmatrix} v_1 \\ v_2 \end{pmatrix}, \tag{4.2.1}$$

$$\begin{pmatrix} i_1 \\ i_2 \end{pmatrix} = \begin{pmatrix} G_{\mathrm{RTD}} v_1 \\ G_{\mathrm{RTD}} v_2 \end{pmatrix}. \tag{4.2.2}$$

The first component of the right term in Eq. (4.2.1) is called the Y matrix of the two-element arrayed oscillator, which represents the two-port network including the antenna structure and RTD capacitances as illustrated in Fig. 4.2.2.1(b).

From Eq. (4.2.1) and (4.2.2), one can obtain

$$\begin{pmatrix} y_{11} - G_{\mathrm{RTD}} & y_{12} \\ y_{21} & y_{22} - G_{\mathrm{RTD}} \end{pmatrix} \begin{pmatrix} v_1 \\ v_2 \end{pmatrix} = 0 \tag{4.2.3}$$

The condition that $v_1$ and $v_2$ have non-zero solution is given by

$$\begin{vmatrix} y_{11} - G_{\mathrm{RTD}} & y_{12} \\ y_{21} & y_{22} - G_{\mathrm{RTD}} \end{vmatrix} = 0 \tag{4.2.4}$$

Given that $\gamma_1$ and $\gamma_2$ are eigenvalues of the Y matrix, the above condition happens if

$$G_{\mathrm{RTD}} = \gamma_1 \text{ or } \gamma_2 \tag{4.2.5}$$

Assuming the array is symmetrical, one obtains $y_{11} = y_{22}$ and $y_{12} = y_{21}$. Two eigenvalues of the Y matrix of the two-element array are $\gamma_1 = y_{11} + y_{12}$ and $\gamma_1 = y_{11} - y_{12}$, respectively. Thus, one can derive the two eigenvectors corresponding to the eigenvalues $\gamma_1$ and $\gamma_2$ are $(v_1, v_2) = (1, 1)$ and $(v_1, v_2) = (1, -1)$, respectively.

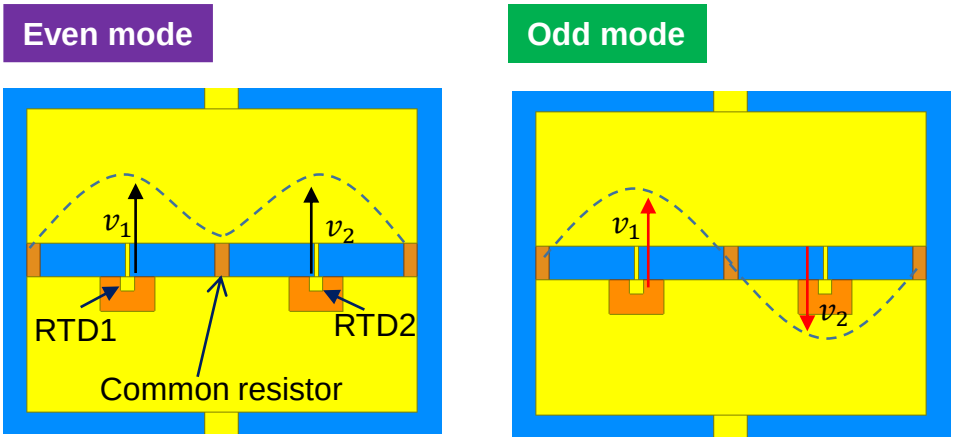


Fig. 4.2.2.2 Illustration of possible operation modes for two-element RTD arrayed oscillator.

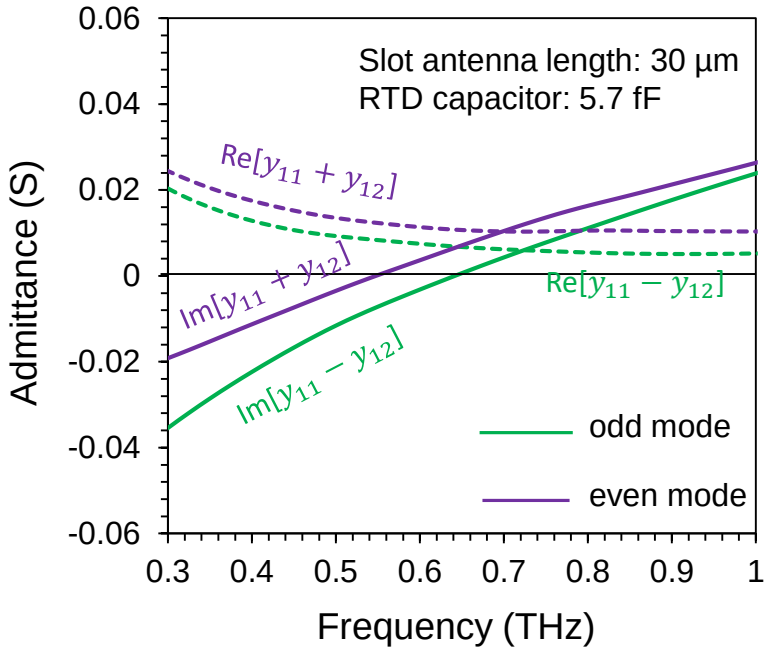


Fig. 4.2.2.3 Illustration of possible operation modes for two-element RTD arrayed oscillator.

Hence, there are two possible operation modes for a two-element arrayed oscillator. The operation mode that corresponds to the eigenvalue $\gamma_1$ is the even mode ($v_1 = v_2$), and that of $\gamma_2$ is the odd mode ($v_1 = v_2$). The illustration of the even mode and odd mode operation is shown in Fig. 4.2.2.3. In the even mode operation, two RTDs have the same phase, while they are anti-phased in the odd mode operation.

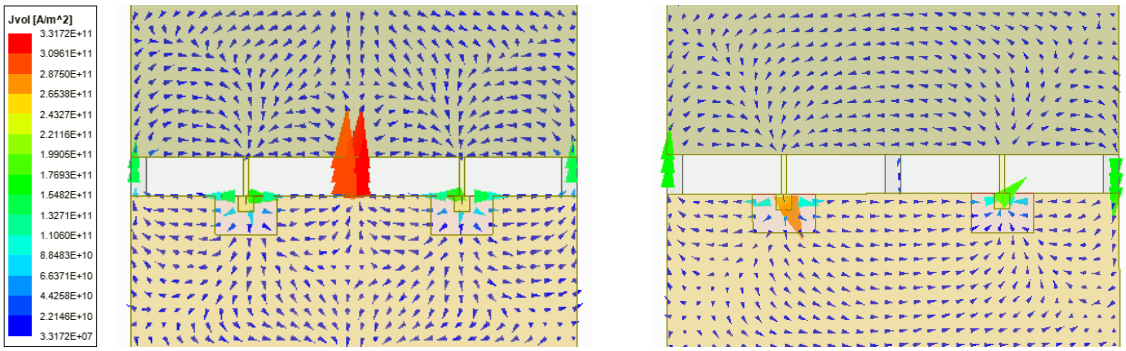


Fig. 4.2.2.4 Illustration of possible operation modes for two-element RTD arrayed oscillator.

Similar to the single oscillator case, separating into the real and imaginary parts for Eq. (4.2.5) under symmetric condition, the oscillation condition is rewritten as $G_{\mathrm{RTD}} =$ Re[$y_{11}$ + $y_{12}$] and Im[$y_{11}$ + $y_{12}$] = 0 for the even mode, and $G_{\mathrm{RTD}} =$ Re[$y_{11}$ - $y_{12}$] and Im[$y_{11}$ - $y_{12}$] = 0 for the odd mode. The condition for the real part gives the NDC of RTD required for the oscillation as well as the output power, while the imaginary part gives the oscillation frequency. The oscillation voltage for the mode with a smaller real part of the eigenvalue will grow rapidly and reach the steady state faster than other modes. Therefore, the mode selectivity is obtained and can be evaluated by the real part of eigenvalues.

The oscillating amplitude $V = |v_1| = |v_2| = \sqrt{\frac{4}{3b}(a - G_{ANT})}$ is obtained similarly to that for the single oscillator, where $G_{ANT}$ = Re[$y_{11}$ + $y_{12}$] for the even mode and $G_{ANT}$ = Re[$y_{11}$ - $y_{12}$] for the odd mode. Thus the total power put by RTDs into the antenna array is obtained as

$$P_{total} = \frac{1}{2}G_{rad}|v_1|^2 + \frac{1}{2}G_{rad}|v_2|^2 = G_{rad}V^2 \quad (4.2.6)$$

and $$P_{total} = \frac{4}{3b}G_{rad}(a - Re[y_{11} + y_{12}]) \text{ for the even mode,} \quad (4.2.7)$$

$$P_{total} = \frac{4}{3b}G_{rad}(a - Re[y_{11} - y_{12}]) \text{ for the odd mode,} \quad (4.2.8)$$

respectively.

One can easily understand which mode will oscillate by calculating the eigenvalues of the Y matrix of the two-element arrayed oscillator. Fig.4.2.2.3 shows an example of eigenvalues of the Y matrix of the two-element arrayed oscillator shown in Fig.2(a). The Y parameters of the two-element arrayed oscillator were obtained using a 3D electromagnetic simulator (Ansys HFSS). The length of each slot antenna was 30 μm. That antenna length was the same as that of the single RTD oscillators fabricated in the primary experiment discussed in Chapter 2. The RTD capacitances were ~5.7 fF.

From Fig.4.2.2.3, it is evident that the real part of the odd mode is smaller than that of the even mode. Hence, according to the above discussion, the odd mode can oscillate more easily. That conclusion, from the physics point of view, is reasonable. This is because, in the even mode, currents flowing through the common resistor caused by the two RTDs are in-phased, resulting in a high loss in the common resistor. In the contrast, in the odd mode operation, these currents are anti-phased, resulting in a very small current flowing through the common resistor. The loss in the common resistor in the odd mode, therefore, is small, making the odd mode operation stable. The current distributions for

the even mode and odd mode are displayed in Fig.4.2.2.4, which clearly shows that the current flowing through the common resistor under the odd mode operation is much smaller than that of the even mode. In the other words, in the odd mode operation, this can be also called push-pull mode, a virtual short condition is obtained at a point midway between two elements.

Unfortunately, odd mode operation seems undesirable for a linearly arranged two-element arrayed oscillator. The reason is that, for RTD oscillators employing a slot antenna as the radiator, output power radiation is obtained in the substrate direction due to the high reflective index of the substrate. However, in the odd mode operation, the electric fields from two RTDs cancel each other in the far field. As a result, just merely small output power radiates in the substrate direction. The structure for extracting output power under the odd mode operation is proposed in section 4.3.

### 4.2.3. *N*-element arrayed oscillator

The analytical method of the two-element array can be extended to the general case of the *N-th* multi-element array. In the *N*-element array, considering each RTD as a port as in the two-element array case, the arrayed oscillator is treated as an *N*-port network as displayed in Fig.4.3.3.1. All RTDs are assumed to be the same and have an effective negative conductance $-G_{\mathrm{RTD}}$. Given the voltage dropped on the *n-th* port and the current flowing into the *n-th* port are $v_n$, $i_n$, respectively, the relations between voltages and currents at the ports are given by

$$\begin{pmatrix} i_1 \\ \vdots \\ i_N \end{pmatrix} = \begin{pmatrix} y_{11} & \cdots & y_{1N} \\ \vdots & \ddots & \vdots \\ y_{N1} & \cdots & y_{NN} \end{pmatrix} \begin{pmatrix} v_1 \\ \vdots \\ v_N \end{pmatrix} \tag{4.2.3.1}$$

$$\begin{pmatrix} i_1 \\ \vdots \\ i_N \end{pmatrix} = \begin{pmatrix} G_{RTD} v_1 \\ \vdots \\ G_{RTD} v_N \end{pmatrix} \tag{4.2.3.2}$$

The $N \times N$ component in the right part of Eq.(4.2.3.1) is the Y matrix of the arrayed oscillator. From Eq. (4.2.3.1) and (4.2.3.2), we obtain

$$\begin{pmatrix} y_{11} - G_{RTD} & \cdots & y_{1N} \\ \vdots & \ddots & \vdots \\ y_{N1} \cdots & & y_{NN} - G_{RTD} \end{pmatrix} \begin{pmatrix} v_1 \\ \vdots \\ v_N \end{pmatrix} = 0 \tag{4.2.3.3}$$

The condition that $v_1,\ v_2, \ldots,\ v_N$ have non-zero solution is given by

$$\begin{vmatrix} y_{11} - G_{RTD} & \cdots & y_{1N} \\ \vdots & \ddots & \vdots \\ y_{N1} \cdots & & y_{NN} - G_{RTD} \end{vmatrix} = 0 \tag{4.2.3.4}$$

Given that $\gamma_1,\ \gamma_2, \ldots,\ \gamma_N$ are eigenvalues of the Y matrix. The condition of Eq.(4.2.3.4) happens if

$$G_{RTD} = \gamma_n \tag{4.2.3.5}$$

Where *n* is one of the $\overline{1, N}$. Eq.(6) is the oscillation condition of any element in the array, and can be separated into two conditions for real and imaginary parts as Re[$\gamma_n$] = $G_{RTD}$ and Im[$\gamma_n$] = 0. Similar to the condition for the single RTD oscillator, the real part condition gives the negative conductance of RTD required for oscillation, while the imaginary part gives the oscillation frequency. Each eigenvalue corresponds to a specific eigenvector $(v_1,\ v_2, \ldots,\ v_n)$ that is a possible operation mode of the arrayed oscillator. Thus, for an *N*-element arrayed oscillator, *N* possible operation modes exist. Moreover, similar to the mode selectivity in the two-element array, among the *N* possible oscillation modes, the mode with the smallest Re[$\gamma_n$] is considered to oscillate easily.

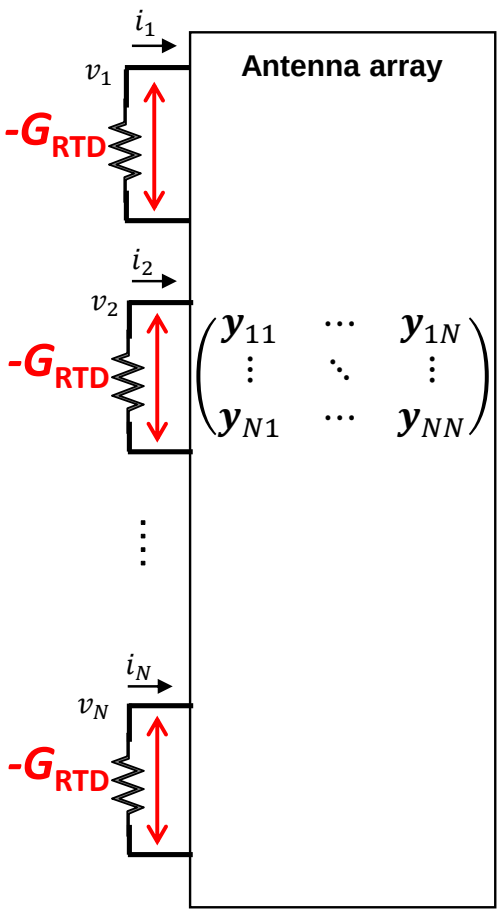


Fig.4.2.3.1. General model of *N*-element RTD arrayed oscillator.

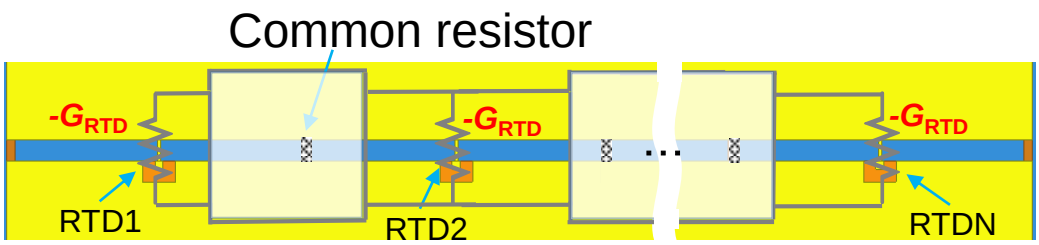


Fig.4.2.3.2. Linearly-arranged *N*-element RTD arrayed oscillator based on structure-simplified RTD oscillator.

Fig.4.2.3.2 shows the schematic structure of the linearly-arranged *N*-element arrayed oscillator coupled to each other via a common stabilization resistor. In this structure,

because the coupling strengths between adjacent elements are much stronger than that of every other element, the coupling parameters except for adjacent coupling are negligible. Assuming the symmetric condition, the Y matrix will be simply expressed as

$$Y=\begin{pmatrix} y_{11} & y_{12} & 0 & \cdots & 0 \\ y_{12} & y_{11} & y_{12} & \ddots & \vdots \\ 0 & y_{12} & \ddots & \ddots & 0 \\ \vdots & \ddots & \ddots & \ddots & y_{12} \\ 0 & \cdots & 0 & y_{12} & y_{11} \end{pmatrix} \tag{4.2.3.1}$$

The eigenvalues and eigenvectors of this type of Y matrix are well-known and can be obtained as

$$\gamma_L = y_{11} + 2y_{12}\cos\left(\frac{L}{N+1}\pi\right), L = 1,2,\dots N. \tag{4.2.3.2}$$

$$v_n^{(L)} = \sin\left(\frac{nL}{N+1}\pi\right),\ n = 1,2,\dots N. \tag{4.2.3.2}$$

These $N$ operation modes correspond to standing waves for the fixed end condition as shown in Fig. 4.2.3.3. From the standing waves, a virtual short condition is satisfied for common resistors in mode $L = N$, and this operation mode is considered to be stable due to small loss. However, the mode separation, i.e. difference of $\mathrm{Re}[\gamma_L]$ between each eigenmode, will be smaller in the multi-element case than that in the two-element case, therefore further investigation on the mode selectivity from theory and experiment is required.

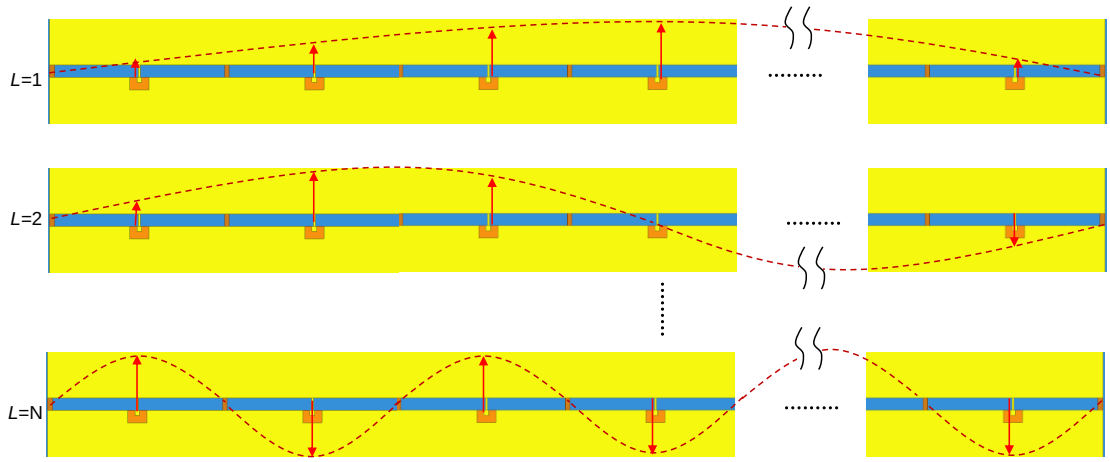


Fig.4.2.3.3. Operation modes in a linearly-arranged *N*-element RTD arrayed oscillator.

# 4.3 Proposal of two-element arrayed oscillator with a right angle arrangement for power combination

The question of how to employ the odd mode operation effectively for power combination is the motivation for the idea of an array configuration using a right-angle arrangement between slots. In the case of a two-element array, two slots are arranged in a right-angle connection as shown in Fig. 4.3.1(a). To investigate the stable operation mode, the calculation of eigenvalues for the proposed two-element arrayed oscillator were conducted. The obtained results are similar to the above calculations shown in Fig.4.2.2.3 for the linearly arranged two-element arrayed oscillator. Those calculations confirmed that the odd mode oscillates more easily than the even mode as expected. The principle of power combination in the odd mode operation is explained as follows. Because vectors electric field in the two slots are perpendicular as illustrated in Fig.4.3.1 (b), they do not cancel each other. The vector total electric field $E_{total}$ is obtained as the sum of these two vectors. Therefore, the combined output power in the substrate direction will be obtained.

Moreover, the proposed arrayed oscillator also allows verifying its operation mode by measuring the polarization characteristic which will be discussed later in the experimental result section.

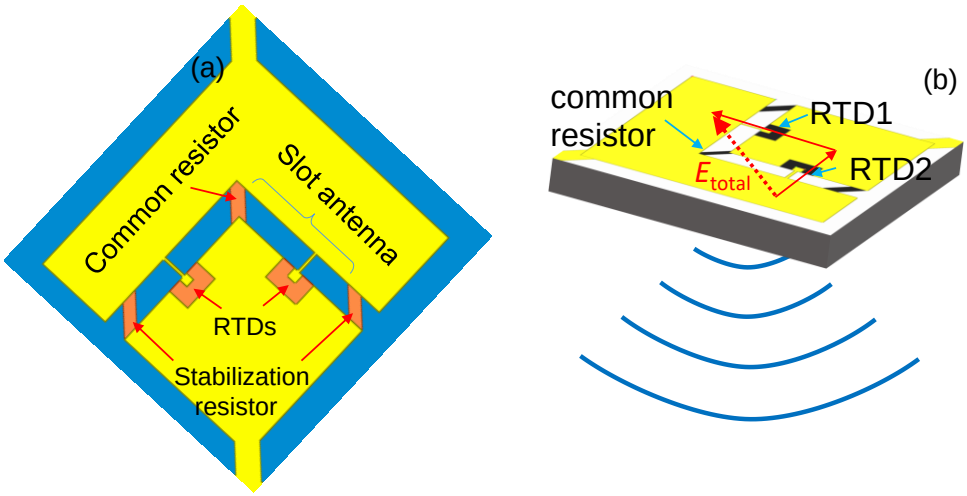


Fig.4.3.1. (a) Two-element arrayed oscillator with center-fed slots and right angle connection, (b) electric field illustration in the odd mode operation of the proposed two-element arrayed oscillator.

Fig.4.3.2 illustrates the current density distribution in the proposed two-element arrayed oscillator operating in the odd mode. In this case, two RTDs are out of phase, and the currents caused by these two RTDs flow through the common resistor in opposite directions. Thus, they cancel each other, resulting in a very small net current flowing through the common resistor. Hence, the loss in the common resistor is small, leading to a stable operation of the odd mode. Additionally, because the current flowing through the common resistor is small, one can make the common resistor narrow. In that case, the total DC current consumption can be significantly reduced, which could be very useful if the structure is expanded into a massive array.

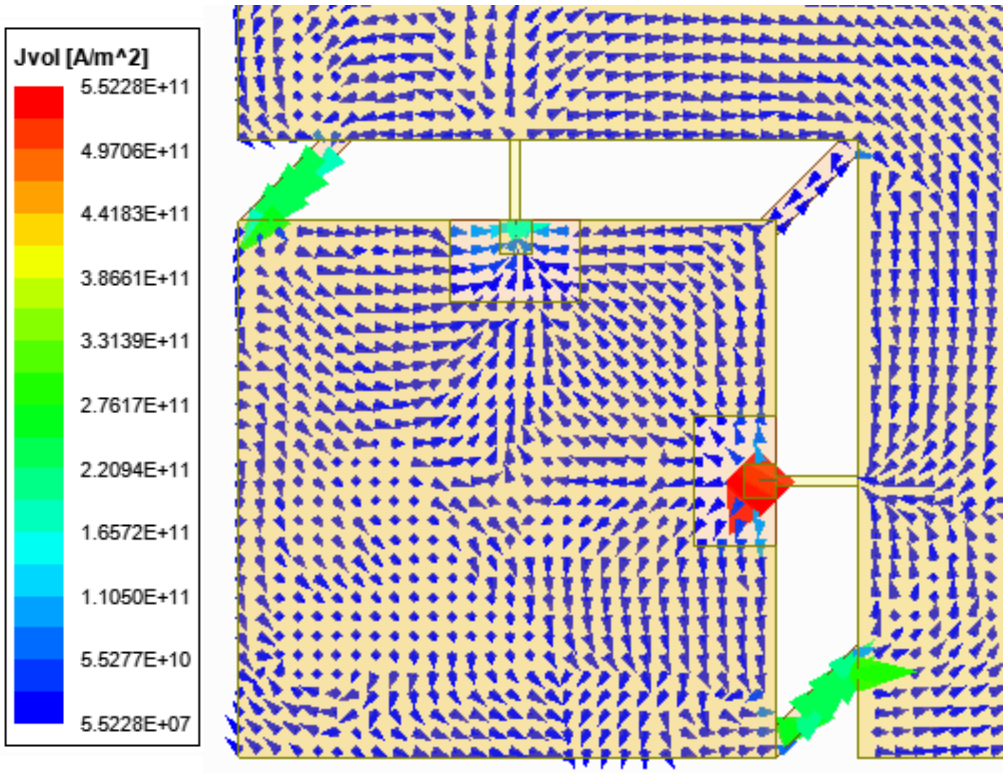


Fig.4.3.2. Current density distribution in the two-element arrayed oscillator with a right angle connection in the odd mode operation.

In the proposed two-element arrayed oscillator. Two array elements are coupled via a common resistor, realizing a strong coupling between array elements. As a result, a coherent oscillation can be obtained owing to mutual injection locking between two array elements. Below the locking range of the proposed arrayed oscillator is analyzed.

The locking range of the proposed arrayed oscillator is calculated as [17]

$$\frac{\omega_1-\omega_2}{\omega_0} \leq 2\varepsilon|k_r| \tag{4.3.1}$$

Where, $\omega_1$, $\omega_2$ are free running frequency of array elements. $\omega_0$ is the average frequency between $\omega_1$ and $\omega_2$. $\varepsilon$ is defined as

$$\varepsilon = \omega_0 L(a - G_L)/2 \tag{4.3.2}$$

$k_r$ is the real part of the coupling strength $k$ and is defined as

$$k_r = -Re[y_{12}]/(a - G_L) \tag{4.3.3}$$

Substituting into Eq. (4.3.1) we obtain

$$\frac{\omega_1 - \omega_2}{\omega_0} \leq 2\varepsilon|k_r| = \omega_0 L \cdot |Re[y_{12}]| \tag{4.3.4}$$

In the above formulas, $L$ and $G_L$ are the inductance and conductance of the antenna structure, respectively. Those parameters can be extracted from the HFSS simulation of the antenna structure. In Chapter 2, for the slot antenna of 30 μm in length, the slot inductance $L$ ~ 9.5 pH. For the arrayed configuration shown in Fig.4.3.1, HFSS simulation gives $Re[y_{12}] \approx$ 3.8 mS at 500 GHz. Thus, at 500 GHz we obtain

$$\frac{\omega_1 - \omega_2}{\omega_0} \leq 0.113$$

At 500 GHz range, the locking range in terms of free running difference, therefore, is $\Delta f = |f_1 - f_2| \approx 56$ GHz which is 11 % of the center frequency. Similarly, it can be estimated that at 600 GHz, those figures are 71 GHz and 11.8 %, respectively.

To investigate the distribution of free-running frequency, an experiment, in which 111 single structure-simplified RTD oscillators having the same design were fabricated, was conducted. The oscillation frequencies of fabricated devices were measured. The histogram of measured oscillation frequencies is displayed in Fig. 4.3.3.

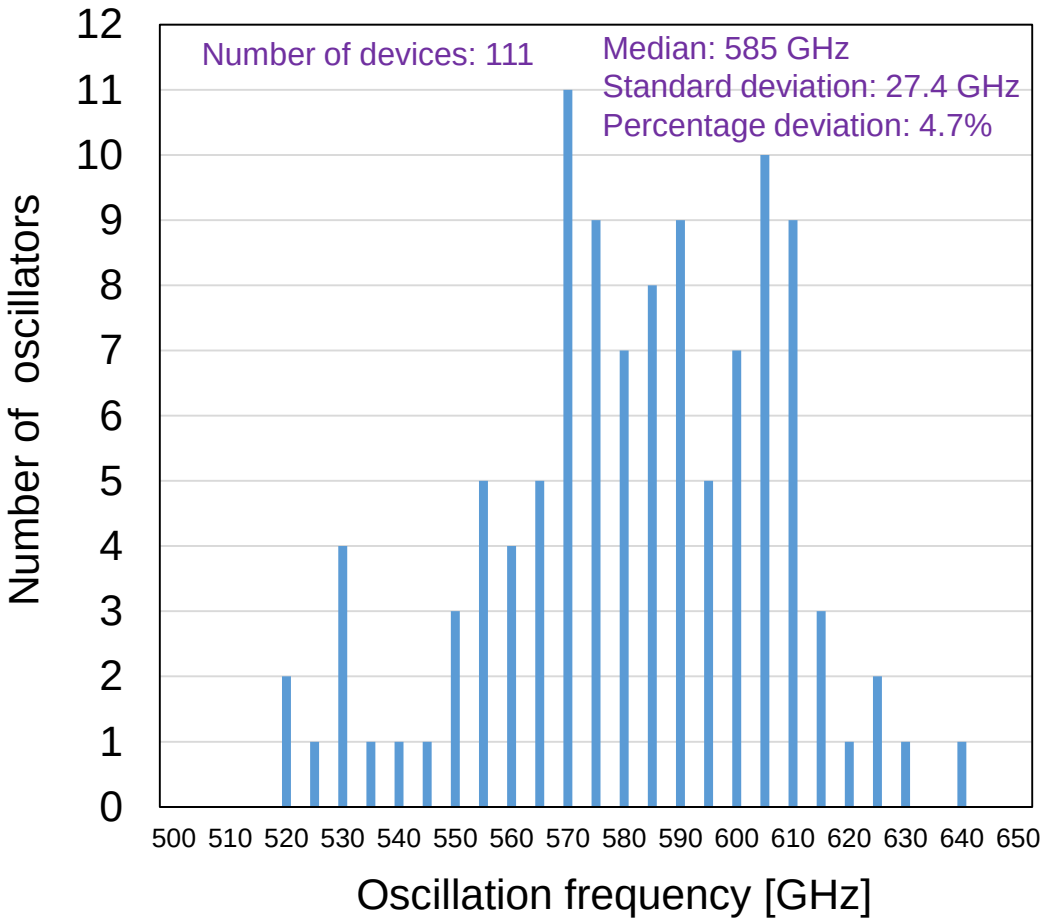


Fig.4.3.3. Histogram of measured oscillation frequencies of 111 single RTD oscillators having the same design.

From the measured result shown in Fig. 4.3.3, it is estimated that the mean and standard deviation of oscillation frequencies are 585 GHz and 27.5 GHz, respectively. Therefore, the oscillation frequency variation is ~ 4.7%. Although in the university condition, the variance of oscillation frequencies strongly depends on the experimenter, this result shows that it is possible to achieve mutual injection locking between array elements with our fabrication process.

# 4.4 Experimental results and discussions

Resistor-coupled two-element arrayed oscillators, which employ center-fed slots, for coherent power combination were fabricated and evaluated. These devices were fabricated using the same simple fabrication process as that of single oscillators described in Chapter 2.

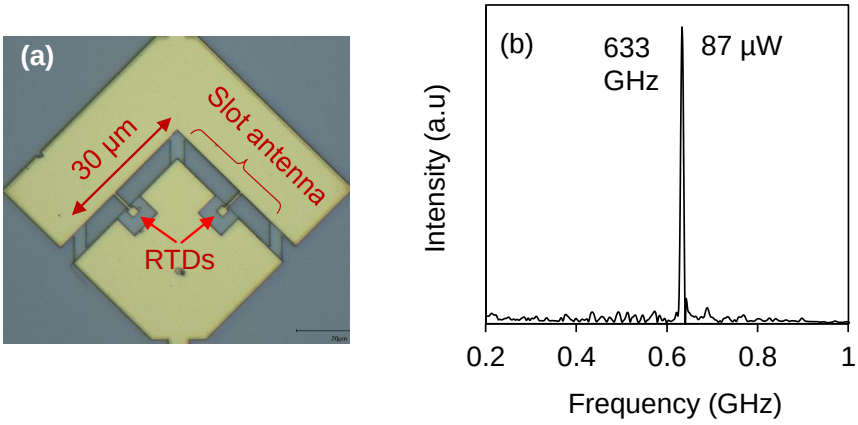


Fig. 4.4.1. (a) Microphotograph of a fabricated device. (b) Oscillation spectrum of a fabricated two-element arrayed oscillator.

The microphotograph of a fabricated device is shown in Fig.4.4.1(a). The slot length is 30 μm. The peak current density $J_p$, peak-to-valley current ratio (PVCR), and voltage width $\Delta V$ of RTD used for this experiment are 12 mA/μm$^2$, 2.5, and 0.4 V, respectively. Fabricated devices were characterized by measurements of oscillation frequency, output power, and polarization. The oscillation frequency was measured using the FTIR method. Fig.4.4.1(b) shows the oscillation spectrum of a fabricated arrayed device oscillating at 633 GHz. A single peak was observed in the oscillation spectra, confirming that the coherent oscillation was obtained. A single peak in the oscillation spectra was also

observed for other fabricated arrayed devices. As mentioned above, coherent oscillation was achieved owing to mutual injection locking. It should be noted that the advantage of this array configuration is the relatively simple coupling part, which is just the common resistor.

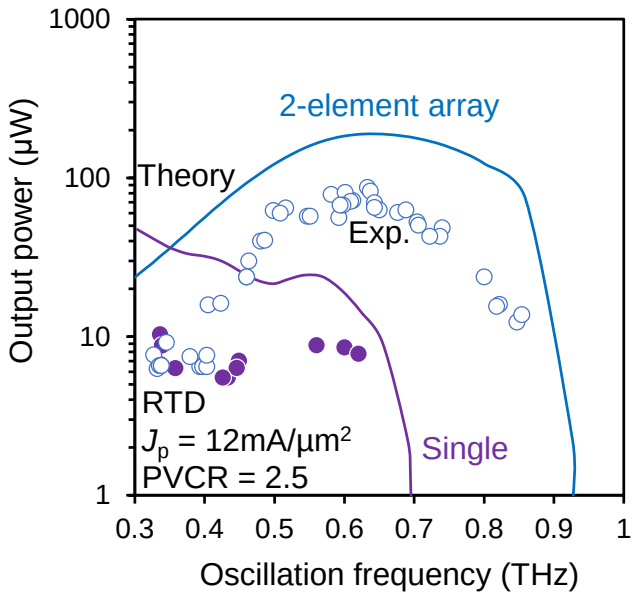


Fig.4.4.2. Output power as a function of oscillation frequency of single oscillators and two-element arrayed oscillators employing center-fed slots in a right angle connection.

Because most of the output power radiates into the substrate direction. The output power was measured using the same method described in Chapter 2. Fig.4.4.2 shows the output power as a function of oscillation frequency for single and arrayed RTD oscillators. The dotted and solid curves show the theoretical calculation of radiated output power for single and arrayed RTD oscillators, respectively. The tendency of experimental results agreed well with theoretical calculations for both single and arrayed devices. The enhancement of output power of arrayed devices compared to that of single devices was

observed. Measured output powers were ~ 10 μW for single oscillators. While the figures were several tens μW for arrayed oscillators. The highest radiated output power of 87 μW at 633 GHz was obtained for a fabricated arrayed oscillator.

The interesting phenomenon observed here is that output power of two-element arrayed oscillator is greater than double that of single oscillator. That can be explained as follows. As mentioned above in the previous section, in the odd mode operation due to the very small net current flowing through the common resistor, the loss in the common resistor is small. As a result, the total loss of the antenna structure of an arrayed device is smaller than that of single oscillator, hence one element of the arrayed device can deliver an output power greater than that of the single oscillator. Consequently, output power of a two-element arrayed device can be more than two times that of a single oscillator. One can also see the frequency limit of the two-element arrayed oscillator being greater than that of the single oscillator. This is another piece of evidence suggesting that the two-element arrayed oscillator operating in the odd-mode has a smaller conduction loss compared to that of the single oscillator. Because the arrayed oscillators have the same layer structure as that of single simplified RTD oscillators. Arrayed devices were fabricated using the same simple fabrication process for single simplified RTD oscillators, which was significantly simplified compared to that of conventional RTD oscillators.

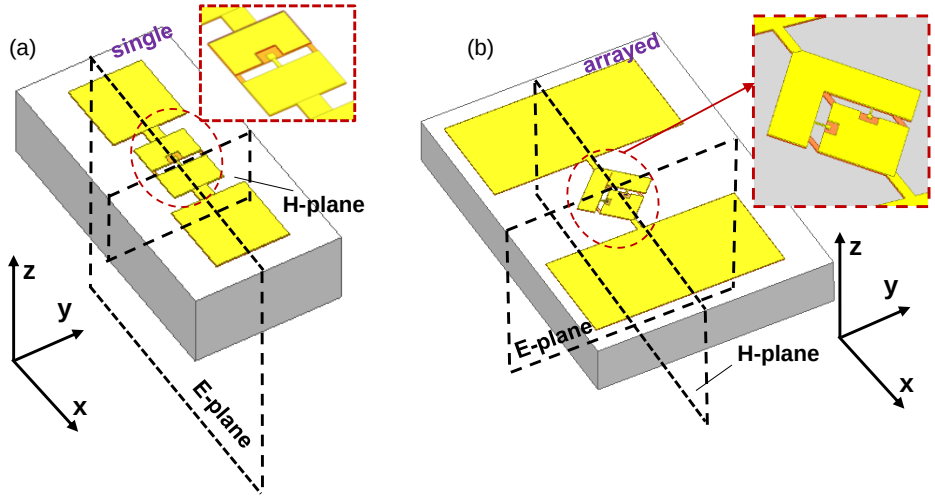


Fig.4.4.3. Definition of E-plane and H-plane for (a) single oscillator and (b) two-element arrayed oscillator.

Fig. 4.4.4 show a comparison of simulated radiation patterns at 600 GHz between single and arrayed oscillators in the E-plane and H-plane, respectively. The definition of E-plane and H-plane for the single oscillator and two-element arrayed oscillator are illustrated in Fig.4.4.3. It is found that the arrayed oscillator has greater peak directivity compared to that of single one. That improvement is attributed to the constructive summation of radiation patterns of array elements. Moreover, two symmetrical main lobes deviated from the broadside were observed in the radiation pattern in the E-plane of the single device as shown in Fig. 4.4.4(a). That was caused by the leaky waves from the slot antenna along the bias pads [4.18]. Those lobes were not observed for the arrayed device. The reason is that the lines connecting the bias pads and slot antenna lying in the plane including the common resistor. In the odd-mode operation, the electric field in that plane is, therefore, very small, resulting in very small leaky waves from the slot antennas to the bias pads.

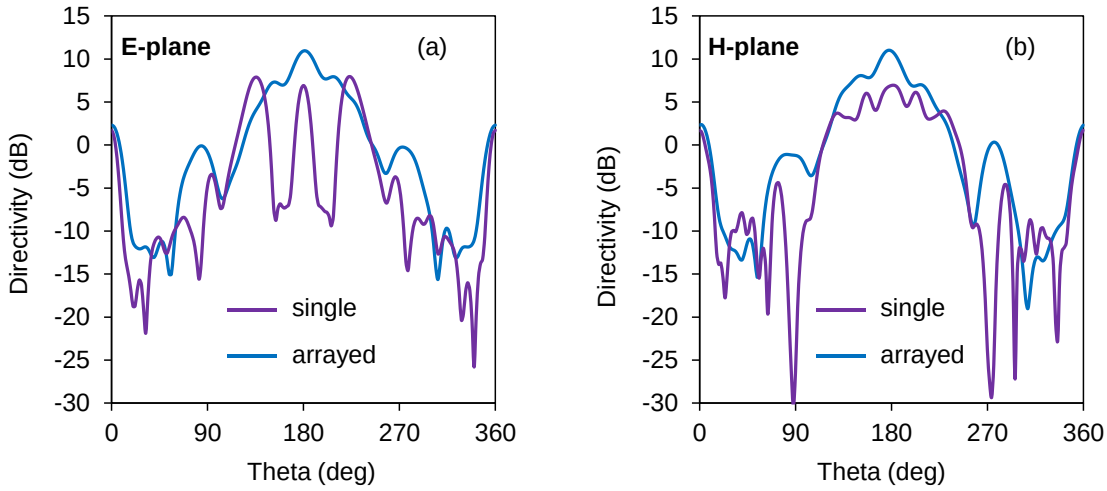


Fig.4.4.4. Comparison of simulated radiation patterns between single and two-element arrayed oscillators.

In a collaboration of our group with a research group from Adelaide University, we improved the radiation pattern of the single RTD oscillator by employing a series-fed-patch design in the bias circuit [4.19].

To experimentally validate the operation mode of fabricated arrayed oscillators, polarization measurements were conducted for single and arrayed oscillators. Knowing the direction of the vector total electric field of the arrayed device, one can understand the phase relationship between two RTDs of the two-element arrayed device, and consequently the operation mode. The polarization measurement setup is relatively similar to that of output power measurement. However, the difference is that in front of the polarization-independent detector, a wire grid polarizer was inserted. The polarizer blocks THz waves having the vector electric field parallel to the wire grid direction, whereas it allows THz waves having the vector electric field perpendicular to the wire grid direction to pass through. During polarization measurement, the RTD chip (single

oscillator or two-element arrayed oscillator) was placed at the center of the hemispherical silicon lens. The directions of single and arrayed devices are illustrated in Fig.4.4.5. The wire grid polarizer was rotated during the measurement.

Fig.4.4.6 shows normalized power intensity recorded by the power meter as a function of rotation angle for single and arrayed devices. There is a $90^0$ difference in the polarization characteristics between the single and two-element arrayed devices. That means, with the directions of single and arrayed devices as shown in Fig.4.4.5, the vector electric field of the single device is perpendicular to that of the two-element arrayed device. That can happen only if two RTDs of the arrayed device are anti-phased. In another word, the operation mode of the arrayed device is odd-mode which agrees well with the above theoretical derivations.

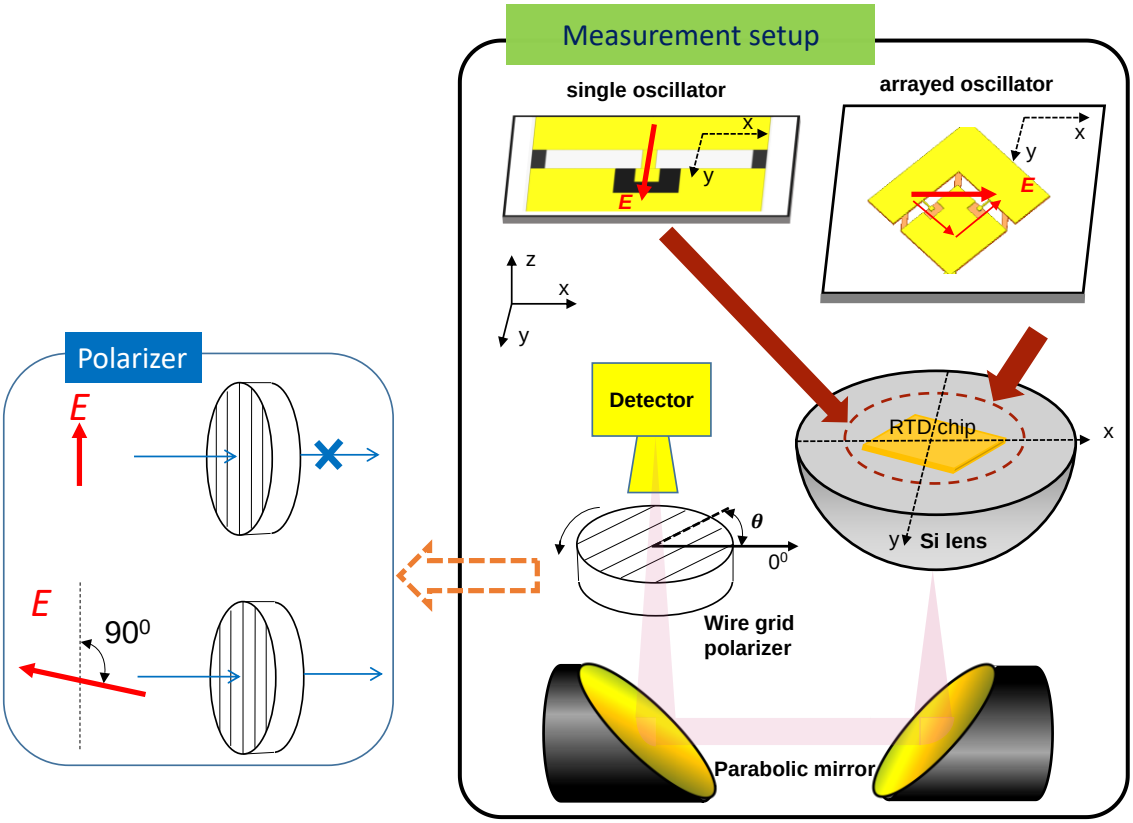


Fig.4.4.5. Measurement setup of the polarization measurement.

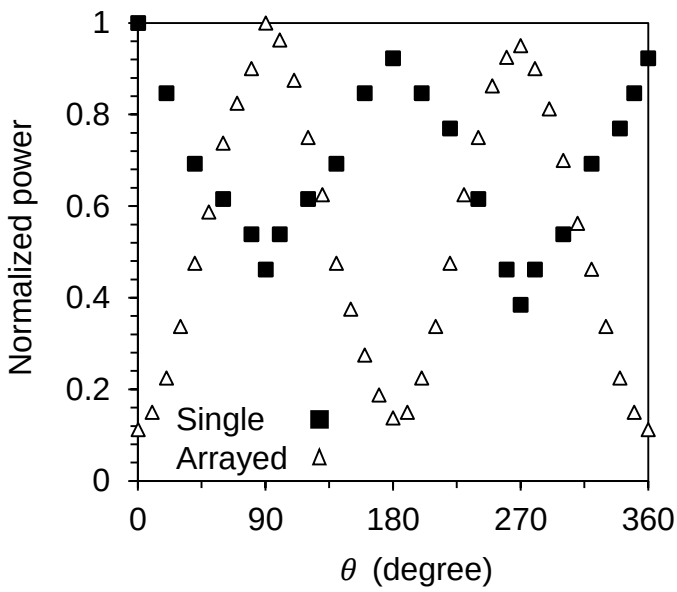


Fig.4.4.6. Measured polarization characteristics

# 4.4 Conclusions

A theoretical model to analyze the operation modes of RTD arrayed oscillators was presented. Then, two-element arrayed RTD oscillators for coherent power combination based on structure-simplified RTD oscillators were proposed and validated. In the proposed arrayed oscillator, the resistor-coupled method was proposed. It is revealed that in the resistor-coupled arrayed RTD oscillators, the odd mode operation is easy to oscillate and stable. That was confirmed by measuring polarization characteristics. Additionally, power combination was obtained by arranging slot antennas in a right-angle connection. Coherent oscillation was achieved owing to mutual injection locking because two elements are coupled to each other via a common resistor. Coherent power combination was verified by oscillation frequency and output power measurements. Odd mode operation was confirmed by measuring polarization characteristics.

# Chapter 5

# Arrayed RTD oscillators based on simplified structure for high output power and high frequency

# 5.1 Introduction

In Chapter 3, structure dependence of single structure-simplified RTD oscillator was investigated. Structures for high oscillation frequency and high output power were revealed. Utilizing a short slot antenna, the highest oscillation frequency of 956 GHz was obtained with an optimized antenna length of 15 μm. In addition to this, by using an offset-fed structure, owing to the increase in the radiation conductance relatively high output power of ~ 220 μW at 500 GHz was obtained.

Then, in Chapter 4, resistor-coupled arrayed RTD oscillators were proposed based on the structure-simplified RTD oscillators. It was found that the odd mode operation, where two adjacent array elements work in anti-phased condition, is stable owing to low loss in the common resistors. Moreover, the angled arrangement of slot antennas was also presented for coherent power combination. The proposed arrayed oscillator operation was validated by experimental results. In the proposed arrayed oscillator, slot antennas with the center-fed structure were employed. The highest output power of 87 μW at 633 GHz was obtained.

In this chapter, the achievements of Chapter 3 and Chapter 4 are combined for higher oscillation frequency and higher output power. In the experiment, the highest oscillation frequency of 1.16 THz was achieved by utilizing an arrayed RTD oscillator employing a short slot antenna. For output power, the highest output power of 766 μW was achieved with a two-element arrayed oscillator employing offset-fed slot antennas that were connected at an angle of $180^0$.

# 5.2 Arrayed RTD oscillator based on simplified structure for high frequency

In Chapter 3, the highest measured oscillation frequency of the single RTD oscillator was 956 GHz, which was achieved with a slot antenna length of 15 μm. Further increase in oscillation frequency is limited by conduction loss of stabilization resistors which form slot antenna. In Chapter 4, a two-element arrayed RTD oscillator was proposed based on the structure-simplified RTD oscillator. Two array elements are coupled with a common stabilization resistor for coherent operation. For resistor-coupled arrayed oscillators odd mode operation, in which two RTDs oscillate in anti-phase condition, is stable to guarantee a low loss in the common resistor. In odd mode operation, for extracting output power in the substrate direction two slot antennas were arranged in a right angle connection. Additionally, because the total AC current flowing through the common resistor was canceled due to the odd-mode operation, the conduction loss of the common resistor becomes small. Therefore, one can employ smaller RTD mesas with maintaining the oscillation condition in the arrayed device, and thus, a higher frequency oscillation can be achieved.

In this section of this chapter, an increase in the oscillation frequency is demonstrated owing to the reduction in the conduction loss, taking the advantage of the odd-mode operation in the resistor-coupled arrayed RTD oscillator.

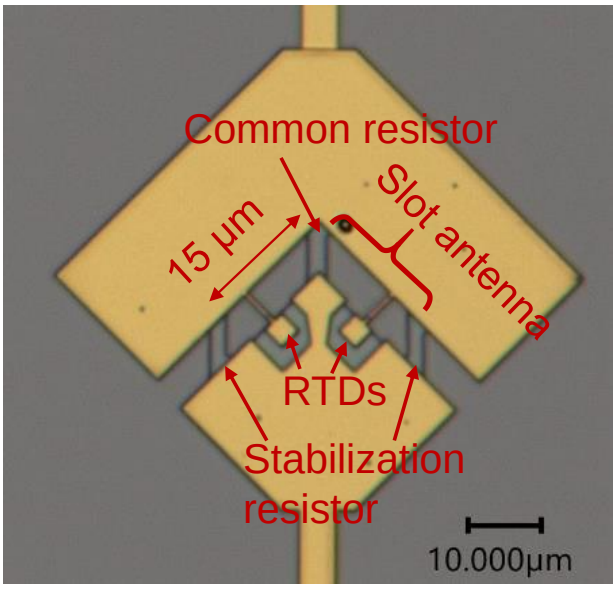


Fig.5.2.1. Microphotograph of a fabricated device.

Fig. 5.2.1 shows the micrograph of a fabricated device. Two RTD mesas were incorporated into the centers of slot antennas, which are connected at a right angle for power combination in the substrate direction. Slot antennas are 15 μm in length. In Chapter 3, the highest oscillation frequency of 956 GHz was achieved by a single oscillator with such antenna length. Two array elements are mutually coupled through the common resistor for coherent oscillation. Similar to the arrayed oscillators in Chapter 4, devices in this experiment were also fabricated using the simple fabrication process described in Chapter 2.

The odd-mode operation of this arrayed RTD oscillator was validated by calculating the admittance of eigenvalues and observing the current distribution, similar to arrayed oscillators investigated in Chapter 4. Fig.5.2.2 shows the comparison of the conduction loss between the single oscillator and the two-element arrayed oscillator (operating in the odd mode) with the same antenna length. It can be seen that the arrayed oscillator operating in the odd mode has a smaller conduction loss for the reason discussed before.

Hence, a higher oscillation frequency limit could be achieved in the arrayed oscillator [5.1-5.3].

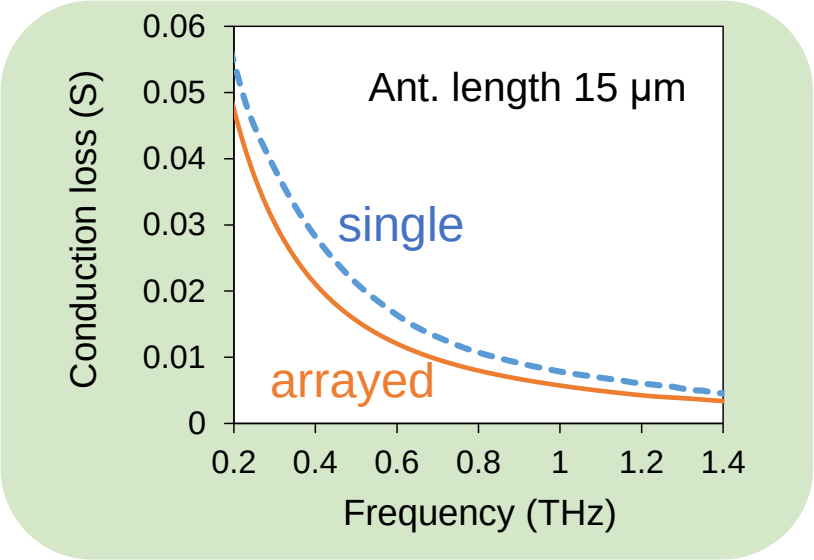


Fig.5.2.2. Conduction loss of single and arrayed oscillators.

The fabricated devices were characterized by measuring oscillation frequency and output power using the same methods as described in Chapter 2. Fig. 5.2.3 shows experimental results. A theoretical curve is also shown. In experimental radiated powers, the transmission loss as THz waves travel a distance of ~20 cm from the RTD chip to the detector was taken into account. The tendency of experiments was roughly agreed with the theoretical curve. The highest oscillation frequency was successfully increased up to 1.16 THz which was 200 GHz higher than that was achieved from the single oscillator in Chapter 3. The oscillation spectrum of a fabricated device was displayed in Fig.5.2.4. A single peak was observed, implying the coherent oscillation in the fabricated device.

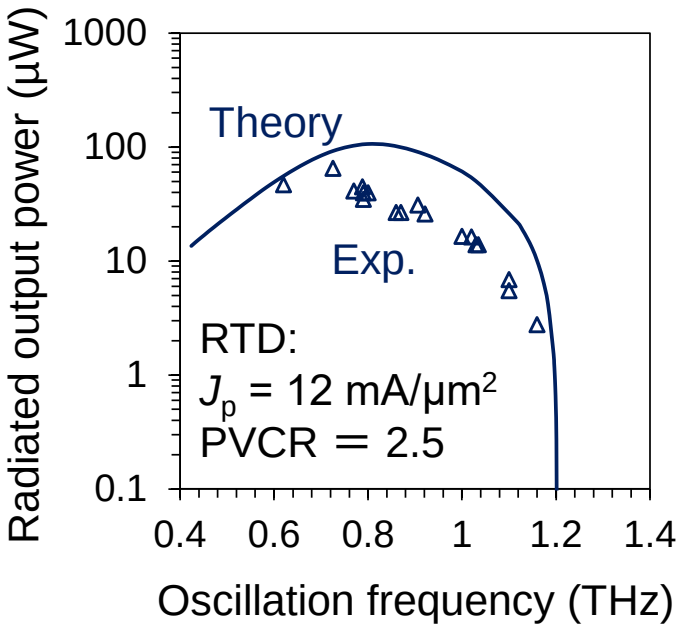


Fig.5.2.3. Output power as a function of oscillation frequency for two-element arrayed oscillator employing short slots.

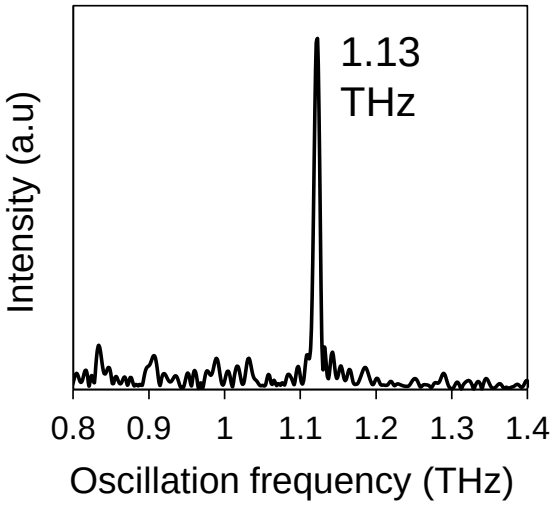


Fig.5.2.4. Oscillation spectrum of a fabricated two-element arrayed oscillator employing short slots.

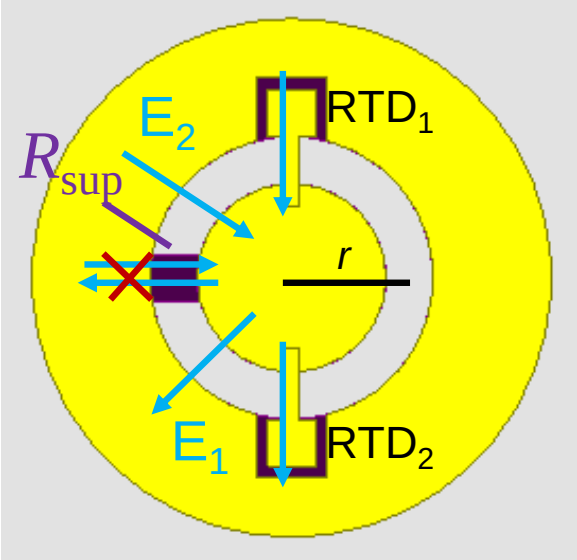


Fig.5.2.5. Improved simplified RTD oscillator

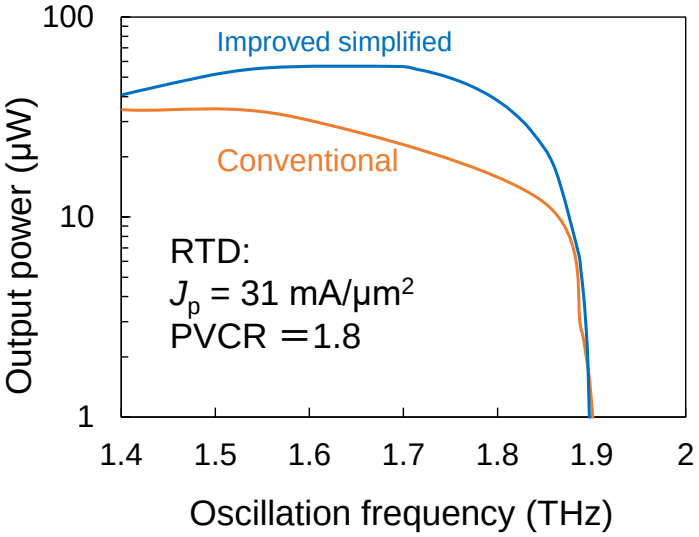


Fig.5.2.6. Calculated oscillation characteristics of the improved simplified RTD oscillator and conventional RTD oscillator. The radius *r* of the ring slot and the length of the conventional slot are 4 μm and 12.5 μm, respectively.

The simplified structure can be further optimized as shown in Fig. 5.2.5. In this structure, a ring slot is used instead of the linear slots. By doing that, just one common

resistor is required. In the odd mode operation, AC currents through the common resistor caused by two RTDs cancel each other, resulting in a very small net current, and consequently very small loss in the common resistor. Thus, the loss contributed by the common resistor vanished. Hence the simplified structure can exhibit performance comparable to the conventional one as shown in Fig. 5.2.6.

# 5.3 Arrayed RTD oscillator based on simplified structure for high output power

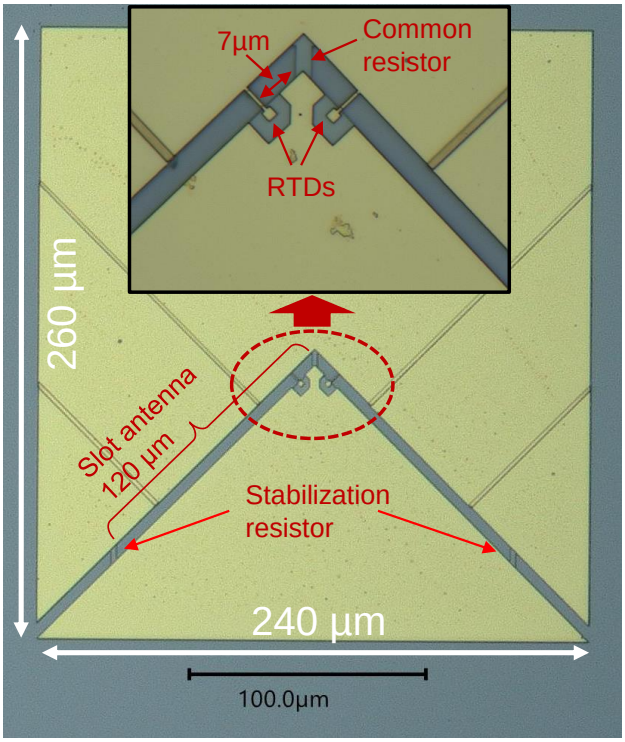


Fig.5.3.1. Two-element arrayed oscillator employing offset-fed slots in a right angle connection.

In chapter 3, it was found that an offset-fed slot is effective for high radiation conductance and consequently high output power [5.4]. Additionally, in chapter 4, coherent power combination was obtained with an array configuration employing center-fed slots, which were arranged in a right-angle connection for extracting power-combined radiation in the substrate direction. In this section of this chapter, improved designs for high output power are proposed, replacing center-fed slots with offset-fed ones. Because each array element employing an offset-fed slot is capable of delivering higher output power, higher combined output power is expected for two-element arrayed oscillators employing offset-fed slots.

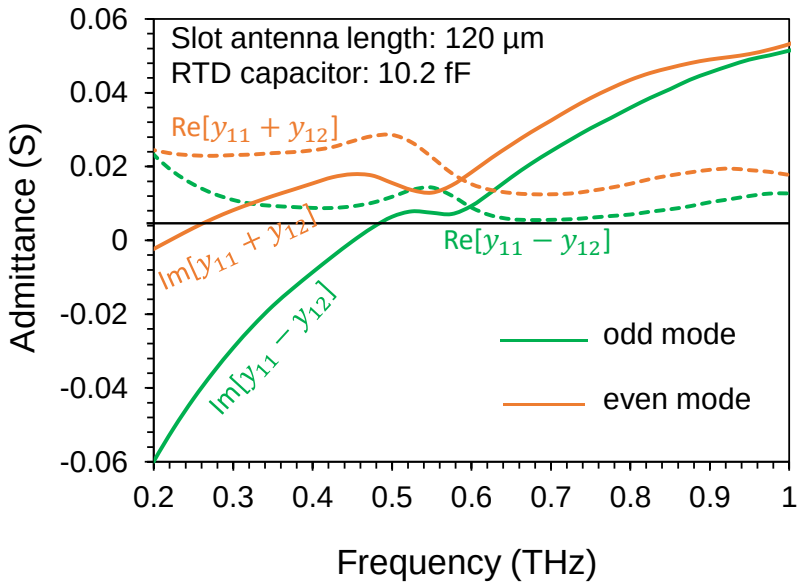


Fig.5.3.2. Calculated eigenvalues (real part and imaginary part) of a two-element arrayed employing offset-fed slots in a right angle connection.

Fig.5.3.1 shows the microphotograph of a fabricated two-element arrayed oscillator employing offset-fed slots. Two slot antennas are connected at a right angle for extracting

output power in the substrate direction in the odd mode operation. The odd mode operation of the proposed arrayed oscillator is discussed below. The slot length is 120 μm. Each RTD was shifted 53 μm from the center of the corresponding slot into the side close to the common resistor.

The odd mode should be the operation mode of this arrayed oscillator to guarantee a small total current flowing through the common resistor, and consequently low loss in the common resistor. That argument is supported by an example of eigenvalues calculated for a two-element arrayed oscillator operating at ~ 450 GHz as shown in Fig.5.3.2. One can see the eigenvalue corresponded to the odd mode has a smaller real part, therefore, the odd mode operation will take place as expected.

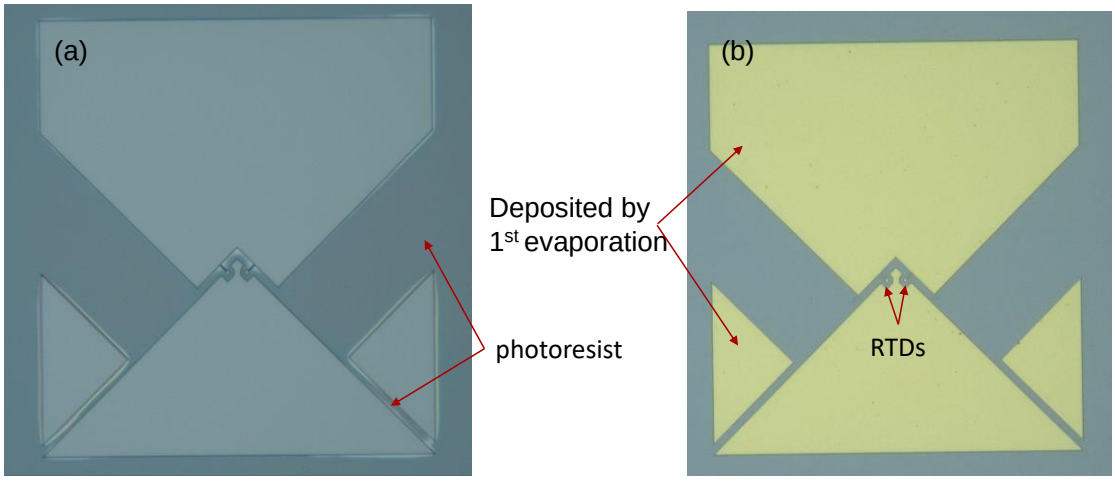


Fig.5.3.3. (a) Device pattern after 1st electron beam exposure. (b) Microphotograph of device electrodes after 1st evaporation and lift-off.

The proposed arrayed oscillators were fabricated using a slightly modified fabrication process compared to that of previously fabricated devices. The modified point is that device electrodes were deposited using twice metal evaporation. In this structure, device

electrodes were formed partly which is different from previously fabricated oscillators, where all electrodes were formed all at once. The reason for that is given later.

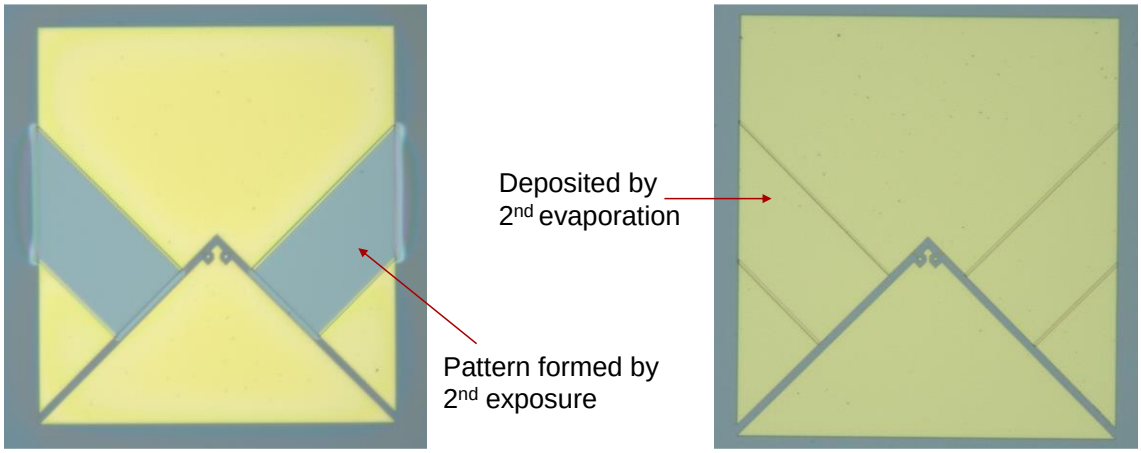


Fig.5.3.4. (a) Pattern of 2nd electron beam exposure. (b) Microphotograph of device electrodes after 2nd evaporation and lift-off.

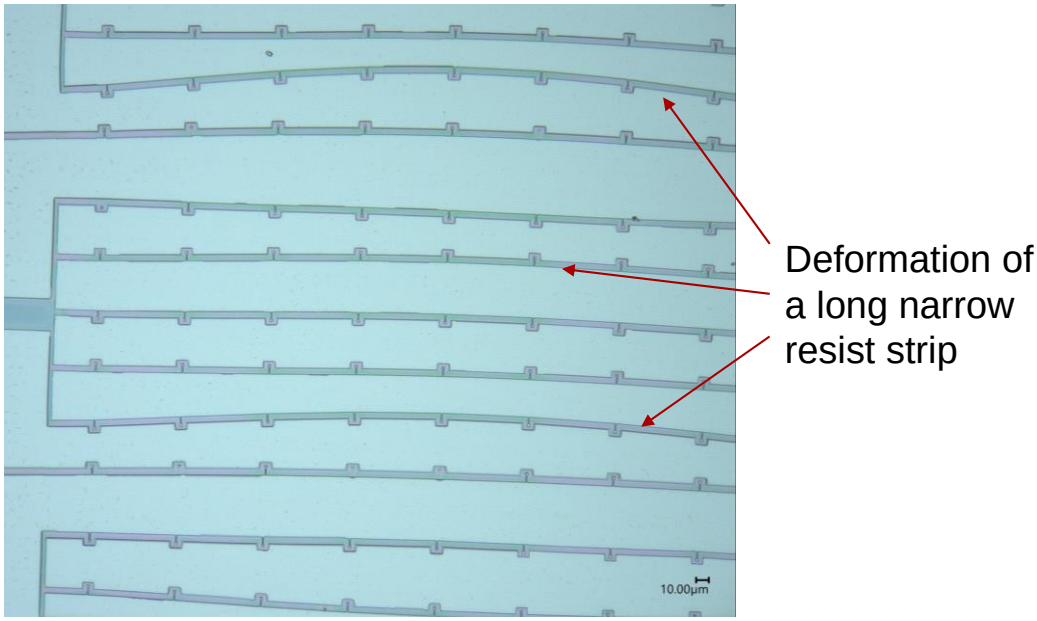


Fig.5.3.5. An example of deformation of a long narrow resist strip.

At first, device patterning was partly formed by the first electron beam exposure followed by resist development as illustrated in Fig.5.3.3(a). After that, part of the device electrodes was obtained by vacuum evaporation followed by lift-off as shown in Fig.5.3.3(b). The remaining part of the device electrodes was then deposited using second electron beam exposure followed by second evaporation as illustrated in Fig.5.3.4(a, b).

The reason two steps of electrode deposition are required is as follows. If the device pattern is formed by just one electron beam exposure, after the development process, a very long narrow strip of resist remains in the position where slot antennas will be formed later. However, unfortunately, such a long narrow resist strip easily gets deformed. An example of deformation of a long narrow resist strip is shown in Fig.5.3.5. This issue probably can also be addressed by using another type of photoresist for electron beam exposure such as PMMA rather than resist composition of ZEP and PMGI.

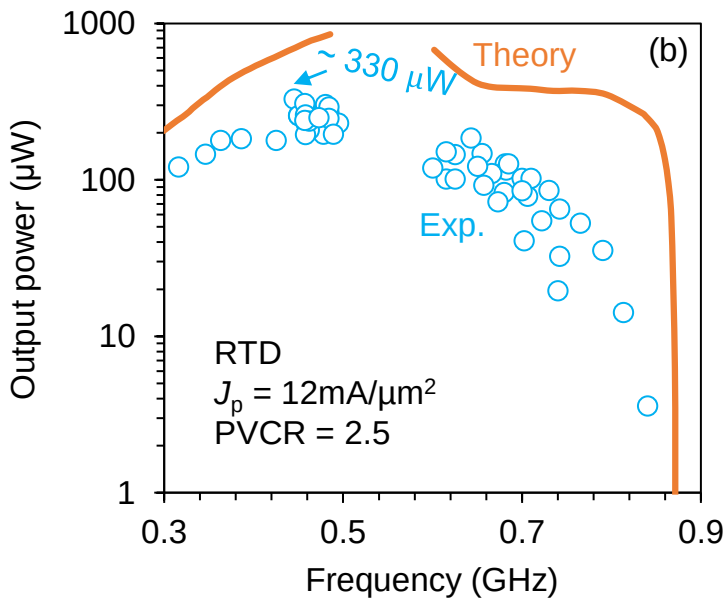


Fig.5.3.6. Output power as a function of oscillation frequency of two-element arrayed oscillators employing offset-fed slots in a right angle connection.

Oscillation frequency and output power of fabricated oscillators employing offset-fed slots were measured. Coherent power combination was obtained from 300 GHz up to 850 GHz. The highest detected power of 126 μW at 445 GH was obtained, such detected power corresponds to the highest radiated output power of 330 μW. Radiated output power as a function of oscillation frequency is shown in Fig.5.3.6. At ~650 GHz, the radiated output power was ~ 200 μW. Although measured powers were lower than calculated ones, the tendency of measured results agreed well with theoretical calculations.

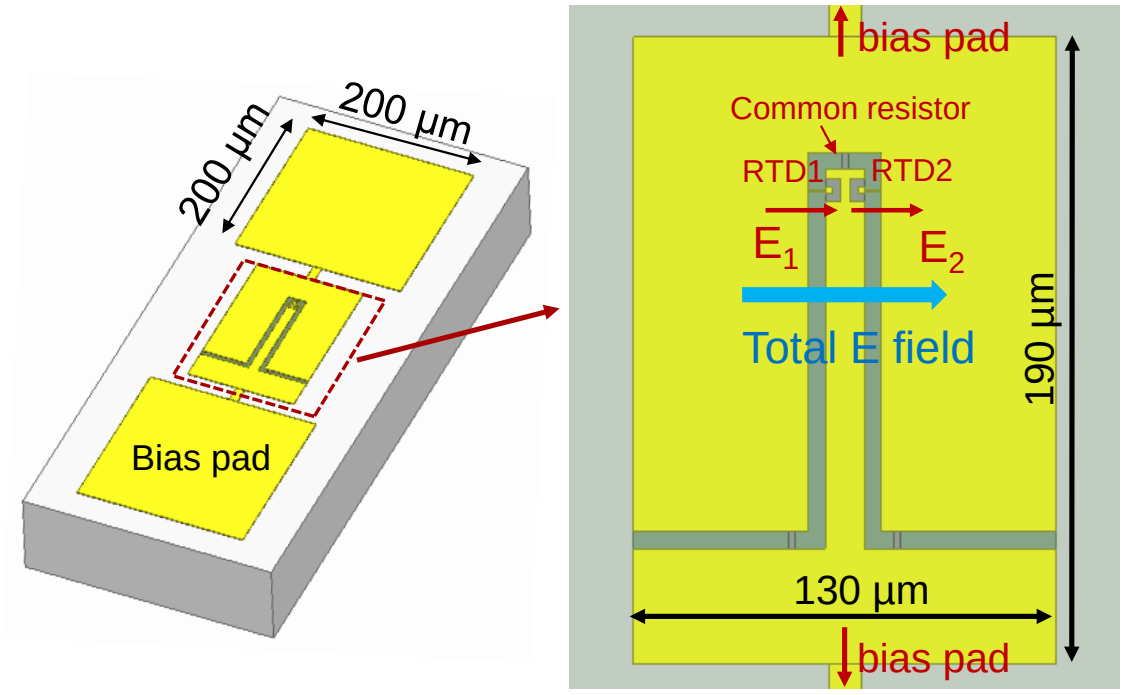


Fig.5.3.7. Two-element arrayed oscillator with $180^0$ angled connection.

In the structure shown in Fig.5.3.1, two slots are connected at an angle of $90^0$ that still has not been optimized yet. Additionally, for the biasing purpose, electrodes were made

relatively large. However, large electrodes around slots antennas degrade radiation efficiency. Therefore, I proposed an improved design as shown in Fig.5.3.7.

In this structure, two slots are connected by an angle of $180^0$. In the odd mode operation, the vectors electric field caused by RTDs have the same direction as shown in Fig.5.3.7. The vector total electric field, therefore, has amplitude greater than that of the one in the structure with $90^0$ angled connection shown above. That results in a more directive radiation pattern, which is highly desired for THz applications. Radiation patterns at 600 GHz of two-element arrayed oscillators employing offset-fed slots are shown in Fig.5.3.9. As expected, the arrayed oscillator with $180^0$ angled connection has a radiation pattern more directive compared to that of the one with $90^0$ angled connection.

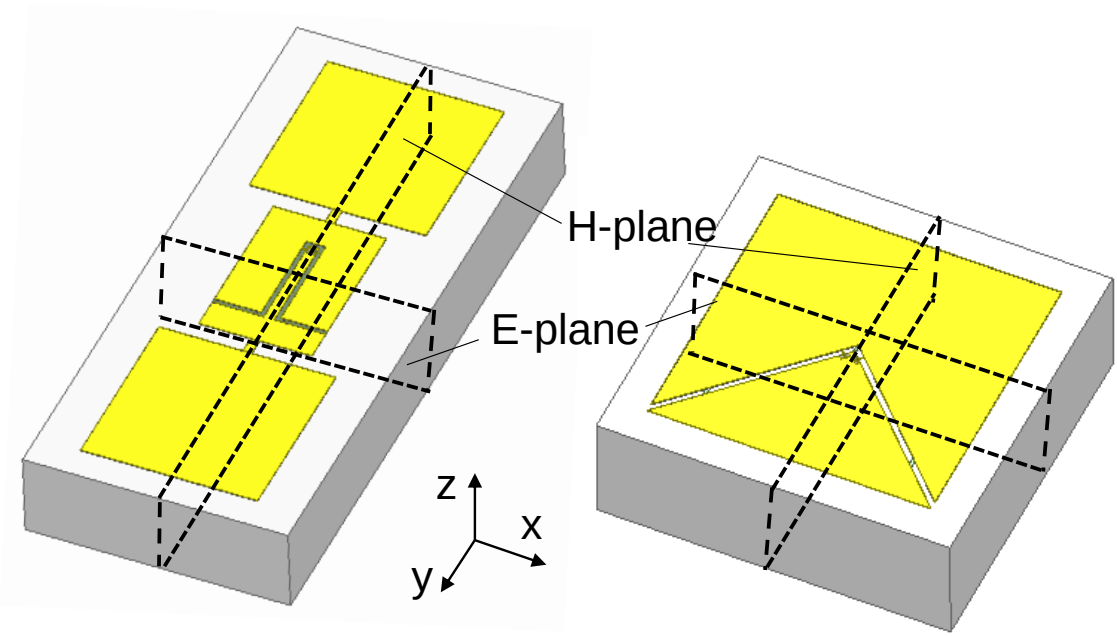


Fig.5.3.8. Definition of E-plane and H-plane of two-element arrayed oscillators employing offset-fed slots.

Additionally, lower loss in the common resistor was also obtained in the arrayed oscillator with $180^0$ angled connection. That can be explained by observing current distributions as shown in Fig.5.3.10. Because the vectors electric field are perpendicular in the arrayed oscillator with $90^0$ angled connection, they do not cancel each other at the common resistor. While in the arrayed oscillator with $180^0$ angled connection, the vectors electric field cancel each other at the common resistor, resulting in smaller AC current flowing through the common resistor and lower loss.

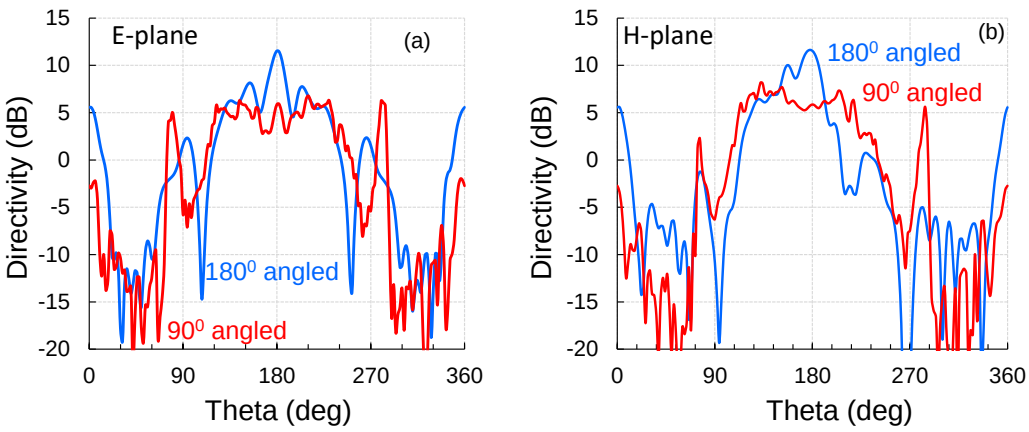


Fig.5.3.9. Radiation patterns of two-element arrayed oscillators employing offset-fed slots.

Moreover, by making electrodes around slot antennas smaller, radiation efficiency of the new design is improved as shown in Fig.5.3.11.

Owing to lower loss in the common resistor and higher radiation efficiency, the two-element arrayed oscillator with $180^0$ angled arrangement of slot antennas exhibits higher output power than that of the one with $90^0$ angled arrangement. Output power of the improved structure is shown in Fig.5.3.12.

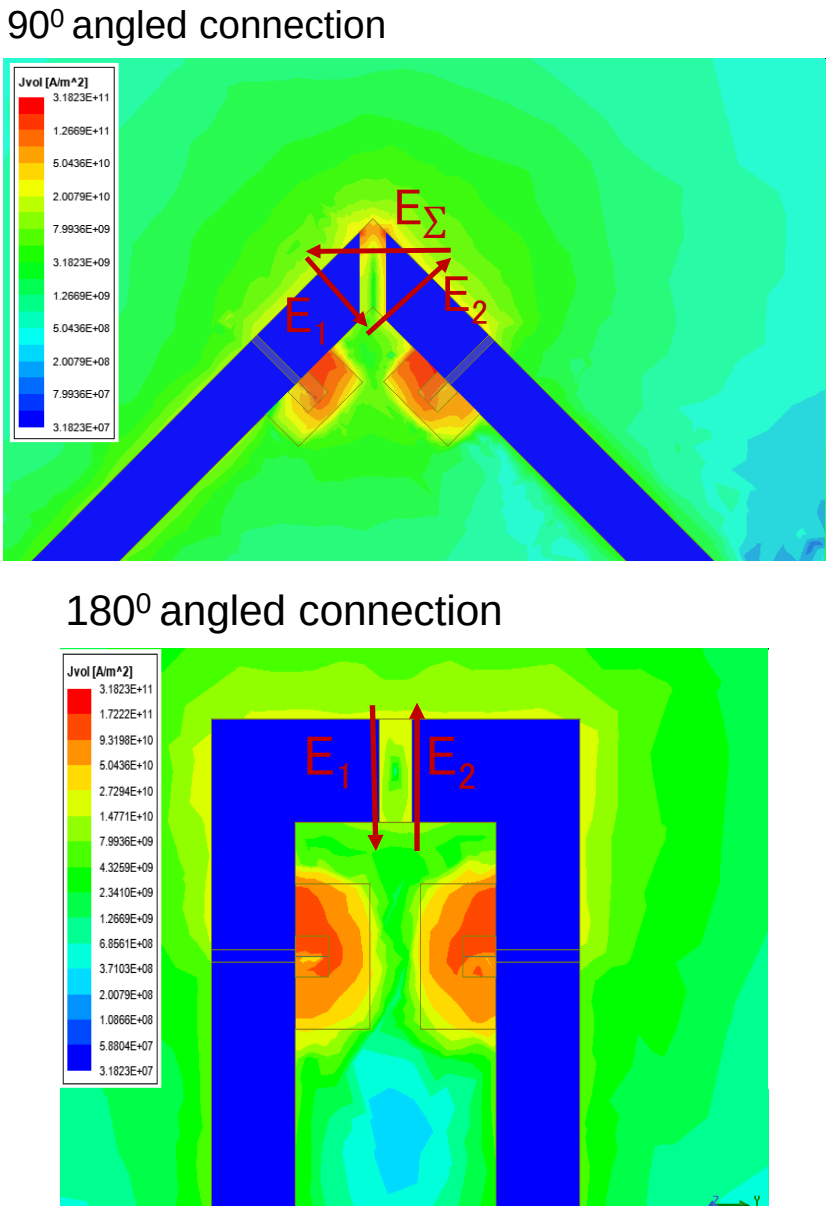


Fig.5.3.10. Current distribution in the common resistor for arrayed oscillators with angled connection of $90^0$ (a) and $180^0$ (b).

In the experiment, relatively high output powers of 766 μW at 530 GHz and 300 μW at 700 GHz were achieved. The highest output power achieved by two-element arrayed oscillators is more than double the highest one achieved by a single oscillator employing an offset-fed slot described in Chapter 3. This suggests an advantage of the resistor-

coupled arrayed oscillators operating in the odd-mode. It is believed the output power can still be enhanced by using RTDs with higher peak current density and PVCR as illustrated by the orange curve.

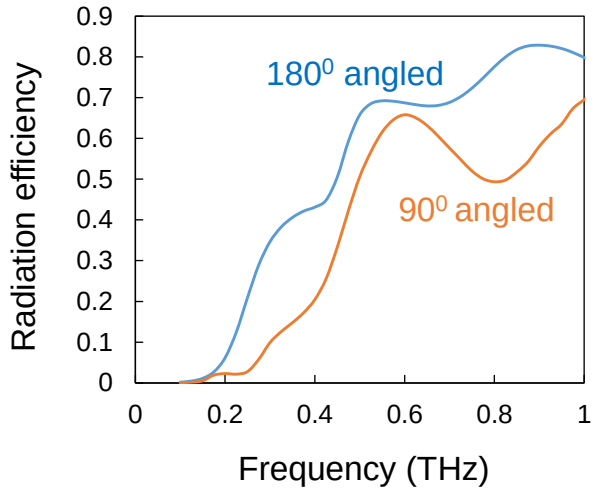


Fig.5.3.11. Radiation efficiency of arrayed oscillators employing offset-fed slots.

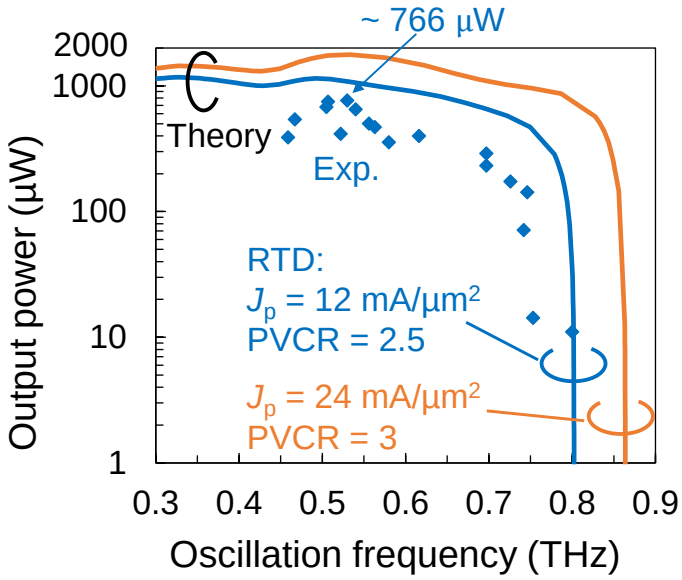


Fig.5.3.12. Output power as a function of oscillation frequency for two-element arrayed oscillator employing offset-fed slots arranged in $180^0$ connection.

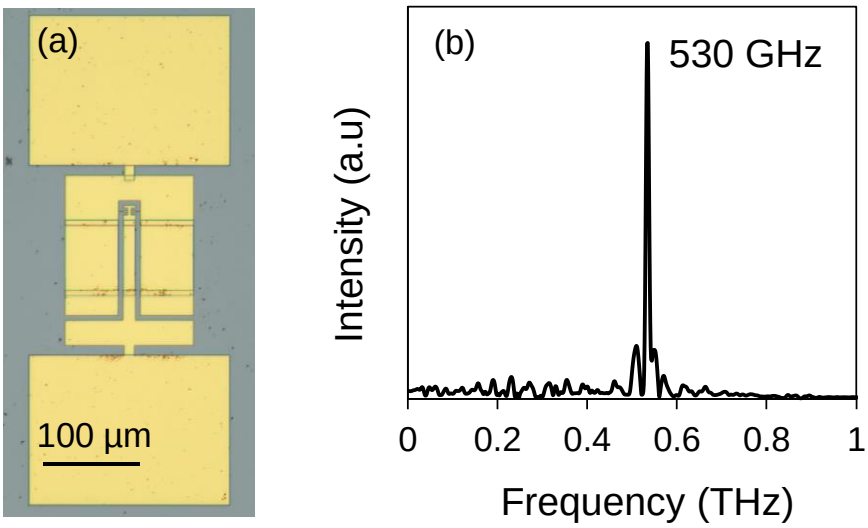


Fig.5.3.13. (a) Microphotograph of a fabricated device and (b) oscillation spectrum of a fabricated device.

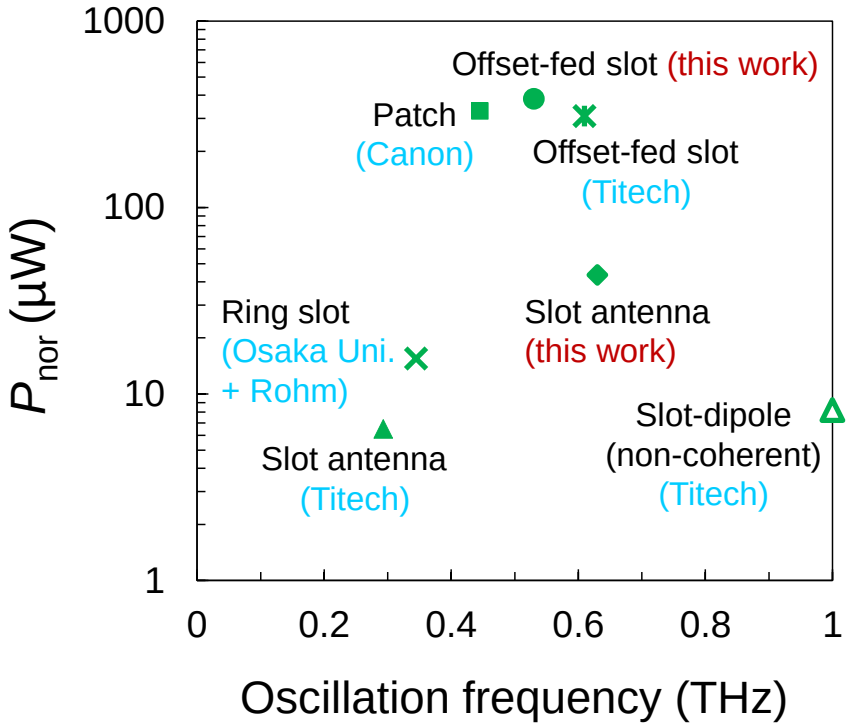


Fig.5.3.14. Normalized output power per one element.

Along with increasing the number of array elements, increasing the power that one array element can deliver is also crucial for an effective power combination. A summary of normalized power per one element for various reported arrayed oscillators is shown below in Fig.5.3.14. The normalized output power per one element is defined as

$$P_{\mathrm{nor}} = \frac{P_{\mathrm{out-arrayed}}}{N} \tag{5.3.1}$$

where $N$ is the number of array elements.

It is found that the simplified structure proposed in this study is capable of delivering comparable $P_{\mathrm{nor}}$ as that of other common structures. That can be achieved because the loss caused by stabilization resistors $R_{\mathrm{sup}}$ is mitigated in arrayed configurations.

A promising application of THz waves is high-data-rate short-range wireless communications such as kiosk-downloader as illustrated in Fig. 5.3.15.

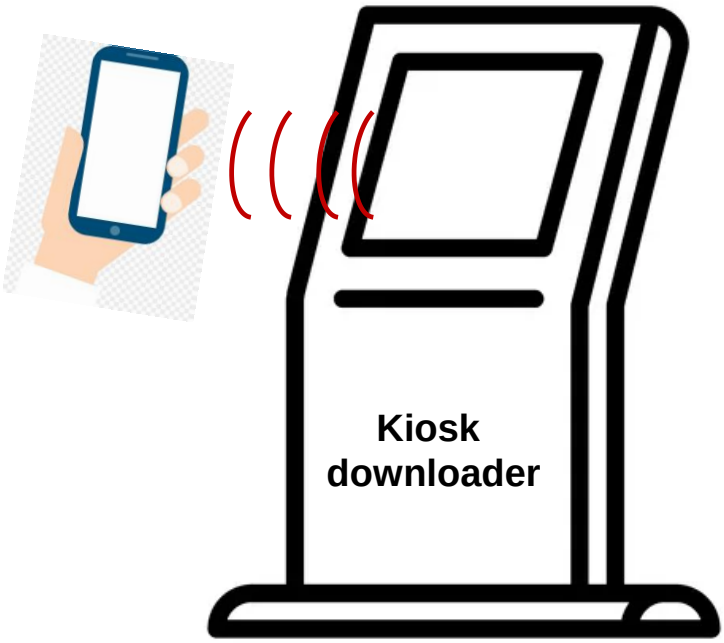


Fig.5.3.15. High-data-rate kiosk downloader.

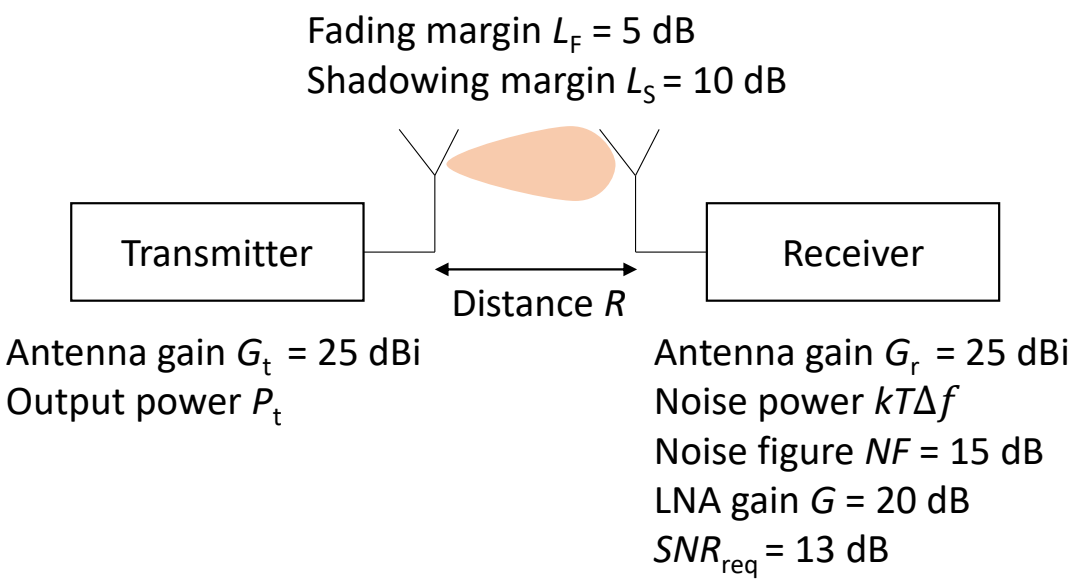


Fig.5.3.16. Model used for estimating the transmission rate.

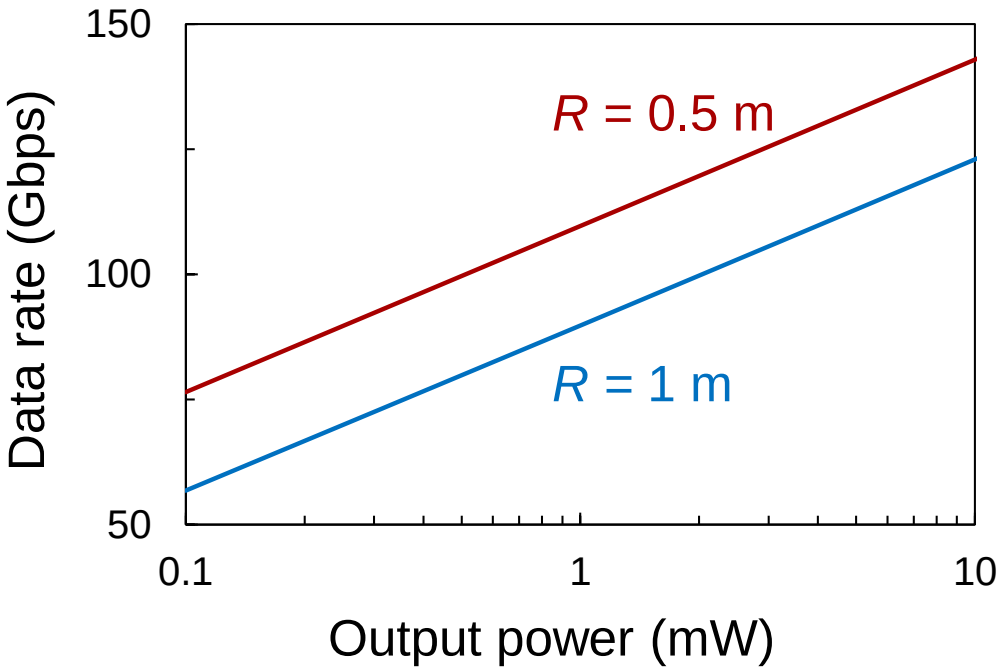


Fig.5.3.17. Estimated transmission rate.

To estimate if the achieved output power is sufficient for wireless communications, the model as shown in Fig.5.3.16 is considered. Where $G_t$ and $G_r$ are the antenna gain of the transceiver and receiver, respectively. $P_t$ and $R$ are the output power of the transceiver, and transmission distance, respectively. $T$ is the absolute temperature, $k$ is Boltzmann's constant, and $\Delta f$ is the bandwidth. The fading margin and shadowing margin are 5 and 10 dB, respectively. $NF$ is the noise figure of the receiver. The required $SNR_{req}$ is 13 dB. Assuming the bandwidth is ~ 10 GHz at 500 GHz. The calculated data rate as a function of the transmitted power is shown in Fig.5.3.17. It is clear that the achieved output powers in this study are sufficient for wireless communications. It is estimated that a high data rate of 90 and 110 Gbps can be achieved with an output power of 0.8 mW at 500 GHz for the transmission distance of 1 and 0.5 m, respectively.

Before ending this chapter, a summary of characteristics of the proposed simplified structure is given in Table 5.1.

In general, the simplified structure exhibits several advantages such as easy extension into array configurations, easy realization of stable operation mode, large locking range, simple fabrication process, and quick application implementation. Although there is a disadvantage of additional loss caused by stabilization resistor $R_{sup}$ in the single simplified structure, it is worth noting that disadvantages caused by stabilization resistors are vanished in resistor-coupled arrayed oscillators, allowing the simplified structure to achieve high power and high oscillation frequency operation.

Table. 5.1. Summary of characteristics.

| **Characteristics** | | 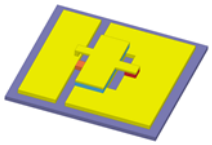 | 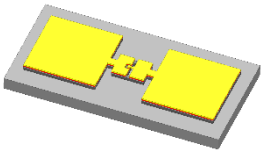 |
|---|---|---|---|
| Single | $G_{loss}$ | $(R_s + R_b)/\omega^2 L_{slot}^2$ | $(R_{sup} + R_s + R_b)/\omega^2 L_{slot}^2$ |
| Arrayed | $G_{loss}$ | $(R_s + R_b)/\omega^2 L_{slot}^2$ | $(R_s + R_b)/\omega^2 L_{slot}^2$ |
| | Extension into array | Complex | Easy |
| | Stable operation mode realization | Difficult | Easy |
| | Locking range | Narrow (few GHz) | Large (several tens GHz) |
| Fabrication process (time) | | Complex (2 moths) | Simple (2 weeks) |
| Application implementation | | Slow | Quick |

$R_s$: resistance along the periphery of the slot.

$R_b$: resistance of the air-bridge.

# 5.4 Conclusions

In this Chapter, achievements obtained from Chapter 3 and Chapter 4 were combined to further increase oscillation frequency and output power of the structure-simplified RTD oscillator. The two-element arrayed oscillator employing short slot antennas was presented for high oscillation frequency by taking advantage of low conduction loss of odd mode operation in a resistor-coupled arrayed oscillator. Oscillation frequency was successfully enhanced up to 1.16 THz that is 200 GHz higher than that was achieved from single structure-simplified RTD oscillator. In addition to this, by adopting offset-fed slots, resistor-coupled array configurations were proposed for high

output power operation. The output power was first increased up to 330 μW at 445 GHz and 200 μW at 650 GHz with an arrayed oscillator employing offset-fed slots that were connected in a right angle. Coherent power combination was also achieved from 300 GHz up to 850 GHz. Then by optimizing structure, the output power reached 766 μW at 530 GHz and 300 μW at 700 GHz by using arrayed oscillator employing offset-fed slots that were connected in an angle of $180^0$. The optimized structure also exhibits a more directive radiation pattern.

# Chapter 6
# Conclusions

This thesis studied novel RTD THz oscillators having a simplified structure. The proposed RTD THz oscillators have the advantage of short fabrication time. In addition to this, various resistor-coupled array configurations based on the structure-simplified RTD oscillator, in which the operation mode can be identified easily, were also proposed for coherent power combination.

Chapter 1 introduced THz waves and their fundamental properties. Various promising applications of THz waves such as high data rate wireless communications, high-resolution imaging, spectroscopy, and sensing were also briefly reviewed. After that, candidates for THz sources were introduced, emphasizing RTD oscillators. Common RTD oscillators have complex a fabrication process mainly because of the existence of metal-insulator-metal (MIM) capacitors. Additionally, due to the existence of many possible operation modes in arrayed RTD oscillators, it is difficult to understand their operation. Thus, the first purpose of the thesis is to realize RTD THz oscillators without MIM capacitors for easy fabrication. Another purpose is to realize resistor-coupled arrayed RTD oscillators for coherent power combination, in which the operation mode can be identified easily.

Chapter 2 discussed the conventional RTD oscillator, its operation principle, and fabrication process. After that, the structure-simplified RTD THz oscillator, in which MIM capacitors were eliminated, was proposed. The operation principle of the structure-

simplified RTD THz oscillator was explained by equivalent circuits. In the experiment, the proposed structure-simplified RTD oscillator was fabricated successfully and oscillation frequencies from 400 GHz to 740 GHz were obtained. Measured output powers were ~ 10 μW up to 600 GHz. The proposed oscillator was fabricated using a fabrication process significantly simplified compared to that of other common RTD oscillators.

In Chapter 3, structure optimization for high output power and high frequency of the proposed RTD oscillator is carried out. Offset-fed slots combined with coplanar stripline antennas are applied to the structure-simplified RTD oscillator to obtain high radiation conductance. Owing to high radiation conductance high output power is expected. In the experiment, the highest output power of 220 μW at 500 GHz was achieved. In addition to this, an optimally short slot antenna is investigated to achieve higher oscillation frequency. By using a short antenna length of 15 μm, the highest oscillation frequency of 956 GHz was obtained.

Chapter 4 investigated an array configuration for coherent power combination based on the structure-simplified RTD THz oscillator. In this chapter, resistor-coupled arrayed oscillators are presented. It is simple to identify the operation mode in a resistor-coupled arrayed oscillator. It is found that in a two-element arrayed RTD oscillator, the odd-mode operation, where two RTDs are anti-phased, is stable. However, in odd-mode operation, a linearly arranged two-element arrayed oscillator exhibits very small output power in the substrate direction because electric fields caused by two RTDs cancel each other. Thus, an angled connection of slot antennas was proposed for coherent power combination in the odd-mode operation. Arrayed elements are mutually injection-locked via the common resistor. The locking range was theoretically estimated ~56 GHz at the 500 GHz range

and ~70 GHz at the 600 GHz range. In an experiment, it is found that an oscillation frequency variation of less than 5 % could be obtained. Such a small variation is sufficient for the operation of the proposed arrayed RTD oscillators. The proposed two-element arrayed oscillator was fabricated and characterized. Output power measurement showed that the power combination was obtained. Additionally, a single peak was observed in the oscillation spectrum of fabricated devices, proving coherent power combination was achieved owing to mutual injection locking. The odd-mode operation was also validated by polarization measurement. The proposed array configuration can be expanded into a large-scale arrayed oscillator for coherent power combination.

In chapter 5, the results of chapter 3 and chapter 4 were combined for achieving higher output power and oscillation frequency. Two-element arrayed RTD oscillators employing offset-fed slots were proposed for high output power operation. Relatively high measured output powers of 766 μW at 530 GHz and 300 μW at 700 GHz were obtained. In addition to this, in odd-mode operation, AC currents caused by two RTDs cancel each other, resulting in a low loss in the common resistor connecting two adjacent elements. This leads to the reduction of the conduction loss which was confirmed by calculation. Thus, arrayed oscillator operating in the odd-mode can reach a higher oscillation frequency limit than that of a single oscillator having the same parameters. Therefore, two-element arrayed oscillators with a slot length of 15 μm were analyzed and fabricated. An oscillation frequency increase was achieved by the reduction in the conduction loss in the odd-mode operation. This time, the highest oscillation frequency reached 1.16 THz. That is 200 GHz higher than that obtained with the single oscillator. Theoretical calculations reveal that by further structure optimization, oscillation frequency limit of close to 2 THz can be obtained by structure-simplified arrayed RTD oscillator.

From this study, structure-simplified RTD oscillators have shown the sufficient capability for THz applications owing to high frequency and high power operation, as well as their simple fabrication process.

# Acknowledgement

Firstly, I would like to express my sincere gratitude to my supervisor Prof. Safumi Suzuki for his enthusiastic guidance and continuous support during my four years in Suzuki Lab. His encouragement gave me the confidence to pursue this difficult but interesting research field. I got a lot of knowledge in THz devices and microfabrication from discussions with him. I am also grateful to him for carefully revising my academic papers and presentation slides. Please accept my deepest gratitude.

I would like to sincerely thank Prof. Masahiro Asada so much for his discussion during weekly seminars. It is my great honor to receive advice from a big name in THz RTD such as him. He laid a strong theoretical foundation that is extremely helpful to study arrayed RTD oscillators.

I am so grateful to Prof. Fumio Koyama, Prof. Yasuyuki Miyamoto, Prof. Hitoshi Wakabayashi, Prof. Masahiro Watanabe, and Prof. Koichi Maezawa for serving as the referees of my thesis defense. Their valuable comments were instrumental for me to complete this thesis.

I really appreciated Dr. Adrian Dobroiu, Dr. Hiroki Tanaka, and Dr. Xiongbin Yu for their support in calculation, fabrication and evaluation of my RTD devices.

I would have not been able to fabricate my RTD devices without the help of students from Asada Lab and Suzuki Lab. So I would like to say special thanks to Yusei Suzuki and Feifan Han for teaching me using clean room facilities. I am so impressed by your efforts in doing experiments. I want to acknowledge the help from Tsuneyu Namba in calculating the eigenvalues of arrayed oscillators as well. I also thank other students from Asada Lab and Suzuki Lab including Mikhail Bezhko, Kazunori Kobayashi, Hidenari Fujikata, Shota Iino, Keiji Kozaka, Tetsuya Miyagawa, Tang Zhenling, Kosuke Aoki,

Yuma Matsushita, Akira Ishikawa, Kazumasa Kito, Shuo Li, Li Yaquion, Shoei Endo, Takumi Shimura, Yang Mingxuan, and Taichi Sato. I had funny chats with students from Asada and Suzuki labs after doing experiments together. Four meaningful years in Suzuki Lab will be a memorable chapter of my life.

I am indebted to members from Nishiyama Lab, Miyamoto Lab, and Shoji Lab for sharing and maintaining clean room facilities. Please continue to use those facilities effectively and achieve great results.

Mr. Shigeo Tamura and Mr. Kenji Morita have continuously maintained electron beam and photomaskless lithography equipment. I would like to thank you so much for taking the time to do this.

I am so grateful to the secretaries Emi Takada, Asako Suzuki, and Hitomi Matsumura for their support on paper works. We have tried to communicate despite language barriers.

I also would like to thank Dr. Fanqui Meng, Dr. Withawat Withayachumnankul, and Stephen Li for giving me a chance to join their collaboration studies.

I couldn't have done it without the encouragement from my master's course supervisor Dr. Luong Duy Manh. He strongly supported me during my scholarship application and introduced me to Suzuki Lab.

I always appreciate the Japan Ministry of Education, Culture, Sport, Science and Technology (MEXT) for granting a scholarship during my study in Japan. I also would like to thank the Embassy of Japan in Vietnam for recommending the scholarship.

I want to say special thanks to my family, my wife, and my kids for their affection and their strong support during my difficult time in research.

Finally, I would like to dedicate this work to my beloved daddy.

# References

## Chapter 1

[1.1] M. Tonouchi, “Cutting-edge terahertz technology,” Nat. Photonics, vol. 1, pp. 97-105, 2007.

[1.2] P. H. Siegel, “Terahertz Technology,” *IEEE Microwave Theory and Technique*, vol. 50, pp. 910-928, 2002.

[1.3] P. H. Siegel, “Terahertz Technology: An overview,” *International Journal of High Speed Electronics and Systems*, vol. 13, no.2, pp. 351-394, 2003.

[1.4] T. Nagatsuma, “Teraherthz technologies: present and future,” *IEICE Electron. Express*, Vol.8, no. 14, 1127-1142, 2011.

[1.5] T. Robin, C. Bouye, and J. Cochard, “Terahertz applications: trends and challenges,” *Proc. of SPIE*, vol. 8985, 898512, 2014.

[1.6] T. Hochrein, “Markets, Availability, Notice, and Technical Performance of Terahertz Systems: Historic Development, Present, and Trend,” *J. Infrared Milli. Terahz. Waves*, vol. 36, 235-254, 2015.

[1.7] N. Kida, T. Miyamoto, and H. Okamoto, “Emission of Terahertz Electromagnetic Waves: A New Spectroscopic Method to Investigate Physical Properties of Solids,” *J. Phys. Soc. Jpn.,* vol. 91, Art. No. 112001, 2022.

[1.8] S. W. Smye1, J. M. Chamberlain, A. J. Fitzgerald, and E Berry, “The interaction

between Terahertz radiation and biological tissue," *Phys. Med. Biol.*, vol. 46, R101-R112, 2001.

[1.9] L. Zhao, Y. H. Hao, and R. Y. Peng, "Advances in the biological effects of terahertz wave radiation," *Military Med Res.*, vol. 1, Art. No. 26, 2014.

[1.10] A. Batra, J. Barowski, D. Damayanov, M. Wiemerler, I. Rolfes, T. Schultze, J. C. Balzer, D. Gohringer, and T. Kaiser, "Short-range SAR imaging from GHz to THz waves," *IEEE J. Microwaves.*, vol. 1, no. 2, pp. 574-585, 2021.

[1.11] T. Nagatsuma, K. Oogimoto, Y. Inubushi, and J. Hirokawa, "Practical considerations of terahertz communications for short distance applications," *Nano Communication Network.*, vol. 10, pp. 1-12, 2016.

[1.12] G. Li, R. V. Mikhaylovskiy, K. A. Grishunin, J. D. Costa, T. Rasing, and A. V. Kimel, "Laser induced THz emission from femtosecond photocurrents in Co/ ZnO/Pt and Co/Cu/Pt multilayers," *Journal of Physics D: Applied Physics.*, vol. 51, Art. No. 134001, 2018.

[1.13] M. C. Beard, G. M. Turner, and C. A. Schmuttenmaer, "Terahertz Spectroscopy," *J. Phys. Chem. B*, vol. 106, pp.7146-7159, 2002.

[1.14] D. Clery, "Brainstorming their way to an imaging revolution," *Science*, vol. 297, 763, 2002.

[1.15] K. Kawase, "Terahertz Imaging," *Optics & Photonics News*, vol. 35, 2004.

[1.16] A. Dobroiu, M. Yamashita, Y. N. Oshima, Y. Morita, C. Otani, and K. Kawase,

"Terahertz imaging system based on a backward-wave oscillator," *Appl. Opt*., vol. 43, no. 30, 5637, 2004.

[1.17] H. J. Song, and T. Nagatsuma, "Present and Future of Terahertz Communications," *IEEE Trans. On Terahertz Science and Technol*., vol. 1, no. 1, 256, 2011.

[1.18] S. Koening, D. L. Diaz, J. Antes, F. Boes, R. Henneberger, A. Leuther, A. Tessman, R. Schmogrow, D. Hillerkuss, R. Palmer, T. Zwick, C. Koos, W. Freude, O. Ambacher, J. Leuthold, and I. Kakkfass, "Wireless sub-THz communication system with high data rate," *Nature Photon*., 275, 2013.

[1.19] E. McCune and Q. Diduck, "4096-QAM Microwave Transmitter Providing Efficiency Exceeding 50% and EVM Below 1%," *2019 14th European Microwave Integrated Circuits Conference (EuMIC)*, 2019, pp. 342-345, Paris, France, Sep. 2019.

[1.20] A. Hirata, T. Kosugi, H. Takahashi, R. Yamaguchi, F. Nakajima, T. Furuta, H. Ito, H. Sugahara, Y. Sato, T. Nagatsuma, "120-GHz-band millimeter-wave photonic wireless link for 10-Gb/s data transmission," *IEEE Trans. Microwave Theory Technol*. vol. 54, pp. 1937–1944, 2006.

[1.21] T. Nagatsuma, H. Ito, and T. Ishibashi, "High-power RF photodiodes and their applications," *Lasers & Photon*. Rev. vol. 3, no. 1-2, pp. 123–137, 2009.

[1.22] S. Koenig, F. Boes, D. Lopez-Diaz, J. Antes, R. Henneberger, R. Schmogrow, D. Hillerkuss, R. Palmer, T. Zwick, C. Koos, W. Freude, O. Ambacher, I. Kallfass, and J. Leuthold,"100 Gbit/s wireless link with mm-wave photonics," *2013 Optical Fiber*

*Communication Conference and Exposition and the National Fiber Optic Engineers Conference (OFC/NFOEC)*. CA, USA, March, 2013.

[1.23] X. Li, Z. Dong, J. Yu, N. Chi, Y. Shao, and G. K. Chang, "Fiber-wireless transmission system of 108 Gb⁄s data over 80 km fiber and 2 × 2 multiple-input multiple-output wireless links at 100 GHz W-band frequency," *Optics Letters,* vol. 37, no. 24, pp. 5106–5108, 2012.

[1.24] T. Nagatsuma, Y. Fujita, Y. Yasuda, Y. Kanai, S. Hisatake, M. Fujiwara, and J. Kani, "Real-time 100-Gbit/s QPSK Transmission Using Photonics-based 300-GHz-band Wireless Link," *2016 IEEE International Topical Meeting on Microwave Photonics (MWP)*. CA, USA, Dec. 2016.

[1.25] V. K. Chinni, P. Latzel, M. Zégaoui, C. Coinon, X. Wallart, E. Peytavit, J.F. Lampin, K. Engenhardt, P. Szriftgiser, M. Zaknoune, and G. Ducournau, "Real-time 100-Gbit/s QPSK Transmission Using Photonics-based 300-GHz-band Wireless Link," *Elec. Letters,* vol.54, no.10, pp. 638-640, 2018.

[1.26] S. Jia , X. Pang, O. Ozolins , X. Yu , H. Hu, J. Yu, P. Guan, F. D. Ros, S. Popov, G. Jacobsen, M. Galili, T. Morioka, D. Zibar, and L. K. Oxenløwe, "0.4 THz photonic-wireless link with 106 Gb/s single channel bitrate," *J. Lightwave Technology*, vol. 36, no. 2, pp. 610-616, 2018.

[1.27] X. Yu, S. Jia, H. Hu, M. Galili, T. Morioka, P. U. Jepsen, and L. K. Oxenløwe, "0.4 THz photonic-wireless link with 106 Gb/s single channel bitrate," *APL Photon*., vol. 1,

no. 8, Art. no. 0 81301,2016.

[1.28] A. Hirata, R. Yamaguchi, T. Kosugi, H. Takahashi, K. Murata, T. Nagatsuma, "10 Gbit/s wireless link using InP HEMT MMICs for generating 120- GHz-band millimeter-wave signal," *IEEE Trans Microw Theory Tech*, vol.57, no.5, pp. 1102-1109, 2009.

[1.29] P. Rodriguez-Vazquez, J. Grzyb, B. Heinemann, U.R. Pfeiffer, "A QPSK 110 Gb/s polarization-diversityMIMO wireless link with a 220–255 GHz tunable LO in a SiGe HBT technology," *IEEE Trans Microw Theory Tech*, vol.68, no.9, pp. 1102-1109, 2009.

[1.30] J. Antes, S. Koenig, D. Lopez-Diaz, F. Boes, A. Tessmann, R. Henneberger, O. Ambacher, T. Zwick, I. Kallfass, "Transmission of an 8-PSK modulated 30 Gbit/s signal using an MMIC-based 240 GHz wireless link," *IEEE MTT-S International Microwave Symposium Digest (MTT)*, Seattle, USA, Ju., 2013.

[1.31] H. Hamada, T. Fujimura, I. Abdo, K. Okada, H. J. Song, H. Sugiyama, H. Matsuzaki, and H. Nosaka, "300-GHz, 100-Gb/s InP-HEMT wireless transceiver using a 300-GHz fundamental mixer," *2018 IEEE/MTT-S International Microwave Symposium*, Philadelphia, USA, Jun., 2018.

[1.32] D. Fritsche, P. Stärke, C. Carta, F. Ellinger, "A low-power SiGe BiCMOS 190 GHz transceiver chipset with demonstrated data rates up to 50 Gbit/s using on-chip antennas," *IEEE Trans Microw Theory Tech*, vol.65, no. 9, 2017.

[1.33] S. Lee, T. Yoshida, S. Amakawa, S. Hara, A. Kasamatsu, "An 80 Gb/s 300 GHz-band single-chip CMOS transceiver," *IEEE International Solid-State Circuits*

*Conference—(ISSCC)*, San Francisco, Feb., 2019.

[1.34] M. H. Eissa, A. Malignaggi, R. Wang, M. Elkhouly, K. Schmalz, A. C. Ulusoy, "Wideband 240 GHz transmitter and receiver in BiCMOS technology with 25 Gbit/s data rate," *IEEE J Solid State Circuits,* vol. 53, no. 9 *(2018),* pp. 2532-2542, 2019.

[1.35] P. Rodríguez-Vázquez, J. Grzyb, B. Heinemann, U.R. Pfeiffer, "A 16-QAM 100 Gb/s 1M wireless link with an EVM of 17% at 230 GHz in an SiGe technology," *IEEE Microw Wirel Compon Lett,* vol. 29, no. 4 *(2018),* pp. 297-299, 2019.

[1.36] J. Wang, A. S, S. Ahearne, and E. Wasige, "1080P HD video transmission using RTD transmitter," *14th U.K.- Europe-China Workshop Millimetre-Waves Terahertz Technol.*, 2021.

[1.37] N. Oshima, K. Hashimoto, S. Suzuki, and M. Asada, "Wireless data transmission of 34 Gbit/s at a 500-GHz range using resonant-tunneling-diode terahertz oscillator," *IEEE Microw Wirel Compon Lett,* Electron. Lett., vol. 52, no. 22, pp. 1897–1898, 2016.

[1.38] N. Oshima, K. Hashimoto, S. Suzuki, and M. Asada, "Terahertz wireless data transmission with frequency and polarization division multiplexing using resonant-tunneling-diode oscillators," *IEEE Trans. THz Sci. Tech-nol*., vol. 7, no. 5, pp. 593–598, 2017.

[1.39] X. Yu, R. Yamada, J. Kim, M. Fujita, and T. Nagatsuma, "Integrated circuits using photonic-crystal slab waveguides and resonant tunneling diodes for terahertz communication," *Progress in Electromagnetics Research Symposium (PIERS)*, pp. 599–

605, Toyama, Japan, 2018.

[1.40] S. Iwamatsu, N. Nishigami, Y. Nishida, M. Fujita, and T. Nagatsuma, “Broadband terahertz resonant tunnelling diode transmitter integrated with coplanar-waveguide-fed slot-ring antenna,” *Electron. Lett*., vol. 57, no. 25, pp. 1001–1003, 2021,

[1.41] S. Diebold, K. Nishio, Y. Nishida, J.-Y. Kim, K. Tsuruda, T. Mukai, M. Fujita, and T. Nagatsuma, “High-speed error-free wireless data transmission using a terahertz resonant tunnelling diode transmitter and receiver,” *Electron. Lett*., vol. 52, no. 24, pp. 1999–2001, 2016.

[1.42] D. M. Mittleman, “Twenty years of terahertz imaging,” *Opt. Express*, vol. 26, pp. 9417–9431, 2018.

[1.43] B. B. Hu, and M. C. Nuss, “Imaging with terahertz waves,” *Opt. Lett.*, vol. 20, no. 16, pp. 1716–1718, 1995.

[1.44] D. M. Mittleman, S. Hunsche, L. Boivin, and M. C. Nuss, “T-ray tomography,” *Opt. Lett*. vol. 22, no. 12, pp. 904–906, 1997.

[1.45] M Herrmann, M Tani, M Watanabe, and K Sakai, “Terahertz imaging of objects in powders,” *IEE Proceedings-Optoelectronics*, vol. 149, no. 3, pp. 116–120, 2002.

[1.46] G. Ok, H. J. Kim, H. S. Chun, and S.-W. Choi, “Foreign-body detection in dry food using continuous sub-terahertz wave imaging,” *Food control*, vol. 42, pp. 284–289, 2014.

[1.47] Y. Jiang, H. Ge, and Y. Zhang, “Detection of foreign bodies in grain with terahertz reflection imaging,” *Optik*, vol. 181, pp. 1130–1138, 2019.

[1.48] G. Ok, K. Park, M.-C. Lim, H.-J. Jang, and S.-W. Choi, “140-ghz subwavelength transmission imaging for foreign body inspection in food products,” *Journal of Food Engineering*, vol. 221, pp. 124–131, 2018.

[1.49] G.-J. Kim, J.-I. Kim, S.-G. Jeon, J. Kim, K.-K. Park, and C.-H. Oh, “Enhanced continuous-wave terahertz imaging with a horn antenna for food inspection,” *J. Infrared, Millimeter, and Terahertz Waves*, vol. 33, no. 6, pp. 657–664, 2012.

[1.50] G. Ok, K. Park, H. S. Chun, H.-J. Chang, N. Lee, and S.-W. Choi, “High-performance sub-terahertz transmission imaging system for food inspection,” *Biomedical optics express*, vol. 6, no. 5, pp. 1929–1941, 2015.

[1.51] Y. Lee, S. Choi, S. Han, D. Woo, and H. S. Chun, “Detection of foreign bodies in foods using continuous wave terahertz imaging,” *J. food protection*, vol. 75, no. 1, pp. 179–183, 2012.

[1.52] G. Ok, H. J. Shin, M.-C. Lim, and S.-W. Choi, “Large-scan-area sub-terahertz imaging system for nondestructive food quality inspection,” *Food Control*, vol. 96, pp. 383–389, 2019.

[1.53] K. Kawase, Y. Ogawa, Y. Watanabe, and H. Inoue, “Non-destructive terahertz imaging of illicit drugs using spectral fingerprints,” *Opt. Express*, vol. 11, pp. 2549–2554, 2003.

[1.54] M. Lu, J. Shen, N. Li, Y. Zhang, and C. Zhang, “Detection and identification of illicit drugs using terahertz imaging,” *J. Appl. Phys.*, vol. 100, Art. no. 103104, 2006.

[1.55] M. Kato, S. R. Tripathi, K. Murate, K. Imayama, K. Kawase, "Non-destructive drug inspection in covering materials using a terahertz spectral imaging system with injection-seeded terahertz parametric generation and detection," *Opt. Epress*, vol. 63, pp. 6425-6432, 2016.

[1.56] A. V. Shchepetilnikov, P. A. Gusiskhin, V. M. Muravev, G. E. Tsydynzhapov, Y. A. Nevfyodov, A. A. Dremin, I. V. Kukushkin, "New ultra-fast sub-terahertz linear scanner for postal security screening," *J. Infrared Millim. Terahertz Waves,* vol.41, pp. 655-664, 2020.

[1.57] J. F. Federici, B. Schulkin, F. Huang, D. Gary, R. Barat, F. Oliveira, and D. Zimdars, "THz imaging and sensing for security applications-explosives, weapons and drugs" *Semicond. Sci. Technol*, vol. 20, Art. no. S266, 2005.

[1.58] N. Palka, M. Szustakowski, M. Kowalski, T. Trzcinski, R. Ryniec, M. Piszcek, W. Ciurapinski, M. Zyckowski, P. Zagrajek, J. Wrobel, "THz spectroscopy and imaging in security Applications" *2012 19th International Conference on Microwaves, Radar & Wireless Communications*, Warsaw Poland, Jul. 2012.

[1.59] S. R. Shahrir, M. B. M. Mokhar, N. F. Zakaria, N. J. Juhari, "A brief overview of detectors used for terahertz imaging systems" *AIP Conference Proceedings*, 2203, 020020 2020.

[1.60] S. R. Shahrir, M. B. M. Mokhar, N. F. Zakaria, N. J. Juhari, "A brief overview of detectors used for terahertz imaging systems" *AIP Conference Proceedings*, 2203,

020020 2020.

[1.61] K. Kamburoğlu, B. Karagöz, H. Altan, and Doĝukan Özen, "An ex vivo comparative study of occlusal and proximal caries using terahertz and X-ray imaging" *Dentomaxillofac Radiol*, vol. 48, no. 2, 2018.

[1.62] S. Fan, B. S. Y. Ung, E.P. J. Parrott, V. P. Wallace, and E. P.-MacPherson, "*In vivo* terahertz reflection imaging of human scars during and after the healing process" *J. Biophotonics*, vol. 10, no. 9, pp. 1143-1151, 2017.

[1.63]N. Born, D. Behringer, S. Liepelt, S. Beyer, M. Schwerdtfeger, B. Ziegenhagen, M. Koch, "Monitoring plant drought stress response using terahertz time-domain spectroscopy," *Plant Physiol.*, vol. 164, no. 4, pp. 1571-1577, 2014.

[1.64] T. Chen, Z. Li, X. Yin, F. Hu, C. Hu, "Discrimination of genetically modified sugar beets based on terahertz spectroscopy," *Spectrochim. Acta Part A Mol. Biomol. Spectrosc*, vol. 153, pp. 586-590, 2016.

[1.65] M. Chen, X. Lijuan, "A preliminary study of aflatoxin B1 detection in peanut oil by terahertz time-domain spectroscopy," *Trans. ASABE*, vol. 57, no.6, pp. 1793-1799, 2014.

[1.66] Z. Chen, Z. Zhang, R. Zhu, Y. Xiang, Y. Yang, and P.B. Harrington, "Application of terahertz time-domain spectroscopy combined with chemometrics to quantitative analysis of imidacloprid in rice samples," *J. Quant. Spectrosc. Radiat. Transfer*, vol. 167, no.6, pp. 1-9, 2015.

[1.67] X. Wu, Y. Dai, L. Wang, Y. Peng, L. Lu, Y. Zhu, Y. Shi, and S. Zhuang "Diagnosis of methylglyoxal in blood by using far-infrared spectroscopy and o-phenylenediamine derivation," *Biomed Opt Express*, vol. 11, no. 2, pp. 963-970, 2020.

[1.68] A. Markelz, A. Roitberg, E. J. Heilweil "Pulsed terahertz spectroscopy of DNA, bovine serum albumin and collagen between 0.1 and 2.0 THz," *Chem Phys Lett*, vol. 320, no. 1-2, pp. 42-48, 2000.

[1.69] I. Al-Naib, "Biomedical sensing with conductively coupled terahertz metamaterial resonators," *IEEE Journal of Selected Topics in Quantum Electronics*, vol. 23, no. 4, Art. no. 16512256, 2016.

[1.70] P. F.-X. Neumaier, K. Schmalz, J. Borngräber, R. Wylde, and H.-W. Hübers, "Terahertz gas-phase spectroscopy: chemometrics for security and medical applications," *Analyst*, vol. 140, no. 4, pp. 213-222, 2015.

[1.71] T. Katagiri, T. Suzuki, Y. Matsuura, "terahertz gas spectroscopy using hollow-optical fiber gas cell," *Opt. Eng*, vol. 57, Art. no. 054104, 2018.

[1.72] B. You, J.-Y. Lu, "Sensitivity analysis of multilayer microporous polymer structures for terahertz volatile gas sensing," *Opt. Epress*, vol. 25, pp. 5651-5661, 2017.

[1.73] D. W. Van der Weide, J. Murakowski, and F. Keilmann "Gas-absorption spectroscopy with electronic terahertz techniques," *IEEE Trans. Microw. Theory Tech.*, vol. 48, pp. 740-743, 2000.

[1.74] J. Chen, K. Nitta, X. Zhao, T. Mizuno, T. Minamikawa, F. Hindle, Z.

Zheng, T. Yasui “Adaptive-sampling near-Doppler-limited terahertz dual-comb spectroscopy with a free-running single-cavity fiber laser,” *Adv. Photon.*, vol. 2, no. 3, Art. no. 036004, 2020.

[1.75] M. O. AlNabooda, R. M. Shubair, N. R. Rishani, and G. Aldabbagh “Terahertz spectroscopy and imaging for the detection and identification of illicit drugs,” *2017 sensors networks smart and emerging technologies (SENSET).*, Beirut, Lebanon, Sep. 2017.

[1.76] A. G. Davies, A. D. Burnett, W. Fan, E. H. Linfield and J. E. Cunningham, "Terahertz spectroscopy of explosives and drugs", *Materials today*, vol. 11, no. 3, pp. 18-26, 2008.

[1.77] N. Shimizu, H. J. Song, Y. C. Kado, T. Furuta, A. Wakatsuki, Y. Muramoto, “Gas Detection Using Terahertz Waves,” *NTT Tech. Rev.*, vol. 7, pp. 1–6, 2009.

[1.78] C. Cao, Z. Zhang, X. Zhao, and T. Zhang, “Terahertz spectroscopy and machine learning algorithm for non-destructive evaluation of protein conformation,” *Optical and Quantum Electronics*, vol. 52, Art. no. 225, 2020.

[1.79] H. Park and J.-H. Son, “Machine learning techniques for thz imaging and time-domain spectroscopy,” *Sensors*, vol. 21, no. 4, 2021.

[1.80] A. Ren, A. Zahid, A. Zoha, S. A. Shah, M. A. Imran, A. Alomainy, and A. H. Abbasi, “Machine learning driven approach towards the quality assessment of fresh fruits using non-invasive sensing,” *IEEE Sensors J.*, vol. 20, pp. 2075–2083, 2020.

[1.81] B. A. Knyazev G. N. Kulipanov, and N. A. Vinokurov, “Novosibirsk terahertz free electron laser: instrumentation development and experimental achievements,” *Meas. Sci. Technol*., vol. 21, Art. no. 054017, 2010.

[1.82] M. A. Demyanenko, D. G. Esaev, B. A. Knyazev, G. N. Kulipanov, and N. A. Vinokurov, “Imaging with a 90frames/s microbolometer focal plane array and high-power terahertz free electron laser,” *Appl. Phy. Lett.*, vol. 92, Art. no. 131116, 2008.

[1.83] G. Dodel, “On the history of far-infrared (FIR) gas lasers: Thirty-five years of research and application,” *Infrared Physics & Technology.*, vol. 40, no. 3, pp. 127-139, 2008.

[1.84] T. Idehara, T. Saito, I. Ogawa, S. Mitsudo, Y. Tatematsu, L. Agusu, H. Mori, and S. Kobayashi, “Development of terahertz FU CW Gyrotron series for DNP,” *Appl. Magn. Reson.*, vol. 34, pp. 265–275, 2008.

[1.85] V. L. Bratman, Y. K. Kalynov, and V. N. Manuilov, “Large-orbit gyrotron operation in the terahertz frequency range,” *Phys. Rev. Lett.*, vol. 102, Art. no. 1245101, 2009.

[1.86] M. Mineo, and C. Paoli, “Corrugated rectangular waveguide tunable backward wave oscillator for terahertz applications,” *IEEE Trans. Electron Devices.*, vol. 57, no. 6, pp. 1481-1484, 2010.

[1.87] X. Xu, Y. Wei, F. Shen, H. Yin, J. Xu, Y. Gong, and W. Wang, “A watt-class 1-THz backward-wave oscillator based on sine waveguide,” *Phys. Plasmas.*, vol. 19, Art. no. 013113, 2012.

[1.88] W. He, C. R. Donaldson, L. Zhang, K. Ronald, P. McElhinney, and A. W. Cross, "High power wideband gyrotron backward wave oscillator operating towards the terahertz region," *Phys. Rev. Lett.*, vol. 110, Art. no. 165101, 2013.

[1.89] T. Ishibashi, T. Furuta, H. Fushimi, S. Kodama, H. Ito, T. Nagatsuma, N. Shimizu, and Y. Miyamoto, "InP/InGaAs Uni-Traveling-Carrier Photodiodes," *IEICE Trans. Electron*., vol. E83-C, no. 6, 2000.

[1.90] H. Ito, F. Nakajima, T. Furuta, and T. Ishibashi, "Continuous THz-wave generation using antenna-integrated uni-traveling-carrier photodiodes," *Semicon. Sci. Technol*., vol. 20, pp. S191-S198, 2005.

[1.91] B. S. Williams, "Terahertz quantum-cascade lasers," *Nature Photonics*, vol. 1, pp. 517-525, 2007.

[1.92] B. Wen, and D. Banm, "High-temperature terahertz quantum cascade lasers," *Progress in Quantum Electronics*, vol. 80, Art. no. 100363, 2021.

[1.93]R. Köhler, A. Tredicucci, F. Beltram, H.E. Beere, E.H. Linfield, A.G. Davies, D.A . Ritchie, R.C. Iotti, F. Rossi, "Terahertz semiconductor-heterostructure laser," *Nature*, vol. 417, pp. 156-159, 2002.

[1.94] W. S. Vitiello, and A. Tredicucci, "Physics and technology of Terahertz quantum cascade lasers," *Advances in Physics: X*, vol. 6, Art. no. 1893809, 2021.

[1.95] L. Schrottke, X. Lü, G. Rozas, K. Biermann, and H. T. Grahn, "Terahertz GaAs/AlAs quantum-cascade lasers," *Appl. Phys. Lett*. vol. 108, Art. no. 102102, 2016.

[1.96] L. Bosco, M. Franckie, G. Scalari, M. Beck, A. Wacker, and J. Faist, “Thermoelectrically cooled THz quantum cascade laser operating up to 210 K,” *Appl. Phys. Lett*. vol. 115, Art. no. 010610, 2019.

[1.97] S. Kumar, Q. Hu, and J. L. Reno, “186 K operation of terahertz quantum-cascade lasers based on a diagonal design,” *Appl. Phys. Lett*. vol. 94, Art. no. 131105, 2009.

[1.98] S. G. Razavipour, E. Dupont, S. Fathololoumi, C. W. I. Chan, M. Lindskog, Z. R. Wasilewski, G. Aers, S. R. Laframboise, A. Wacker, Q. Hu, D. Ban, and H. C. Liu, “An indirectly pumped terahertz quantum cascade laser with low injection coupling strength operating above 150 K,” *J. Appl. Phys*. vol. 113, Art. no. 203107, 2013.

[1.99] M. A. Belkin, F. Capasso, F. Xie, A. Belyanin, M. Fischer, A. Wittmann, and J. Faist, “Room temperature terahertz quantum cascade laser source based on intracavity difference-frequency generation,” *Appl. Phys. Lett*. vol. 92, Art. no. 201101, 2008.

[1.100] M. A. Belkin and F. Capasso, "New frontiers in quantum cascade lasers: high performance room temperature terahertz sources", *Physica Scripta*, vol. 90, no. 11, Art. no. 118002, 2015.

[1.101] K. Fujita, S. Jung, Y. Jiang, J. H. Kim, A. Nakanishi, A. Ito, et al., "Recent progress in terahertz difference-frequency quantum cascade laser sources", *Nanophotonics*, vol. 7, no. 11, pp. 1795-1817, 2018.

[1.102] K. Fujita, S. Hayashi, A. Ito, M. Hitaka and T. Dougakiuchi, "Sub-terahertz and

terahertz generation in long-wavelength quantum cascade lasers", *Nanophotonics*, vol. 8, no. 12, pp. 2235-2241, 2019.

[1.103] T. A. Midford, and R. L. Bernick R L, “mm-wave CW Impatt diodes and oscillators”, *IEEE Trasn. On MTT*, vol. 27, pp. 483-491, 1979.

[1.104] T.T. Fong, and H. J. Kuno, “mm-wave pulsed Impatt sources,” *IEEE Trans. On MTT*, vol. 27, pp. 492-499, 1979.

[1.105] H. Eisele, “355 GHz oscillator with GaAs TUNNETT diode,” *Electron. Lett.*, vol. 41, no. 6, pp. 1-2, 2005.

[1.106] J. Nishizawa, P. Plotka, H. Makabe and T. Kurabayashi, “GaAs TUNNETT diodes oscillating at 430-655 GHz in CW fundamental model,” *IEEE Microwave and Wireless Components Letters*, vol. 15, pp. 597-599, 2005.

[1.107] J. Nishizawa, P. Potka, T. Kurabayashi and H. Makabe, “706-GHz GaAs CW fundamental-mode TUNNETT diodes fabricated with molecular layer epitaxy,” *Phys. Stat. Sol.(c),* vol. 5, no. 9, pp. 2802-2804, 2008.

[1.108] H. Eisele, A. Rydberg, and G. I. Haddad, “Recent advances in the performance of InP Gunn devices and GaAs TUNNETT diodes for the 100–300-GHz frequency range and above,” *IEEE Trans. Microwave Theory and Technique,* vol. 48, no. 4, pp. 626-631, 2000.

[1.109] H. Eisele “High performance InP Gunn devices with 34 mW at 193 GHz,” *IEEE Trans. Microwave Theory and Technique,* vol. 48, no. 4, pp. 626-631, 2000.

[1.110] J. Yun, D. Yoon, H. Kim and J.-S. Rieh, "300-GHz InP HBT oscillators based on common-base cross-coupled topology", *IEEE Trans. Microw. Theory Techn.*, vol. 62, no. 12, pp. 3053-3064, 2014.

[1.111] J. Yun, J. Kim and J.-S. Rieh, "A 280-GHz 10-dBm signal source based on InP HBT technology", *IEEE Microw. Wireless Compon. Lett.*, vol. 27, no. 2, pp. 159-161, 2017.

[1.112] J. Yun, J. Kim, D. Yoon and J.-S. Rieh, "645-GHz InP heterojunction bipolar transistor harmonic oscillator", *Electron. Lett.*, vol. 53, no. 22, pp. 1475-1477, 2017.

[1.113] M. Urteaga, M. Seo, J. Hacker, Z. Griffith, A. Young, R. Pierson, P. Rowell , A. Skalare, V. Jain, E. Lobisser, and M.J.W. Rodwell, "InP HBTs for THz frequency integrated circuits", *IEEE conference on Indium Phosphide and Related Mater (IPRM)*, Berlin, Germany, May 2011.

[1.114] P. Hillger, J. Grzyb, R. Lachner, U. Pfeiffer, "An antenna-coupled 0.49 THz SiGe HBT source for active illumination in terahertz imaging applications", *the 10th European Microwave Integrated Circuits Conference (EuMIC)*, Paris, France, 2015.

[1.115] Z. Hu, M. Kaynak, and R. Han, “High-Power Radiation at 1 THz in Silicon: A Fully Scalable Array Using a Multi-Functional Radiating Mesh Structure,” *IEEE J. Solid-state Circuits*, vol. 53, no. 5, pp. 1313-1327, 2018.

[1.116] W. R. Deal, X. B. Mei, V. Radisic, K. Leong, S. Sarkozy, B. Gorospe, J. Lee, P. H. Liu, W. Yoshida, J. Zhou, M. Lange, J. Uyeda, and R. Lai, “Demonstration of a 0.48

THz amplifier module using InP HEMT transistors," *IEEE Microwave and Wireless Components Letters*, vol. 20, no. 5, pp. 289- 291, 2010.

[1.117] X. Mei, W. Yoshida, M. Lange, J. Lee, J. Zhou, P.-H. Liu, K. Leong, A. Zamora, J. Padilla, S. Sarkozy, R. Lai, and W. R. Deal, "First Demonstration of Amplification at 1 THz Using 25-nm InP High Electron Mobility Transistor Process," *IEEE Electron Device Letters*, vol. 36, no. 4, pp. 327-329, 2015.

[1.118] R. Izumi, S. Suzuki and M. Asada, "1.98 THz resonant-tunneling-diode oscillator with reduced conduction loss by thick antenna electrode," *The 42nd Int. Conf. on Infrared, Millimeter, and Terahertz Waves (IRMMW-THz)*, Cancun, Mexico, 2017.

[1.119] M. Bezhko, S. Suzuki, and M. Asada, "Frequency increase in resonant-tunneling diode cavity-type terahertz oscillator by simulation-based structure optimization," *Jpn. J. Appl. Phys.* vol. 59, Art. no. 032004, 2020.

[1.120] M. Asada, and S. Suzuki, "Terahertz Emitter Using Resonant-Tunneling Diode and Applications," *Sensors,* vol. 21, Art. no. 1384, 2021.

[1.121] M. Feiginov, "Frequency limitations of resonant-tunnelling diodes in sub-THz and THz oscillators and detectors," *J. Infrared Milli. Terahz Waves*, vol. 40, pp. 365–394, 2019.

[1.122] R. Tsu and L. Esaki, "Tunneling in a finite superlattice," *Appl. Phy. Lett.*, vol. 22, no. 11, p. 562-564, 1973.

[1.123] E. R. Brown, "Oscillations up to 712 GHz in InAs/AlSb resonant-tunneling

diodes," *Appl. Phys. Lett*. vol. 58, Art. no. 2291, 1991.

[1.124] S. Suzuki, A. Teranishi, K. Hinata, M. Asada, H. Sugiyama, and H. Yokoyama, "Fundamental Oscillation of up to 831 GHz in GaInAs/AlAs Resonant Tunneling Diode," *Appl. Phys. Express,* vol. 2, Art. no. 054501, 2009.

[1.125] S. Suzuki, M. Asada, A. Teranishi, H. Sugiyama, and H. Yokoyama, "Fundamental oscillation of resonant tunneling diodes above 1 THz at room temperature," *Appl. Phys. Lett.,* vol. 97, Art. no. 054501, 2010.

[1.126] H. Kanaya, H. Shibayama, R. Sogabe, S. Suzuki, and M. Asada, "Fundamental Oscillation up to 1.31 THz in Resonant Tunneling Diodes with Thin Well and Barriers," *Appl. Phys. Express,* vol.5, Art. no. 124101, 2012.

[1.127] M. Feiginov, H. Kanaya, S. Suzuki, and M. Asada, "1.46 THz RTD oscillators with strong back injection from collector," *Appl. Phys. Lett.,* vol. 104, Art. no. 243509, 2014.

[1.128] T. Maekawa, H. Kanaya, S. Suzuki, M. Asada, "Frequency increase in terahertz oscillation of resonant tunnelling diode up to 1.55 THz by reduced slot-antenna length," *Appl. Phys. Lett.,* vol. 104, Art. no. 243509, 2014.

[1.129] T. Maekawa, H. Kanaya, S. Suzuki, and M. Asada, "Oscillation up to 1.92 THz in resonant tunneling diode by reduced conduction loss," *Appl. Phys. Express*, vol. 9, Art. no. 024101.

[1.130] S. Kitagawa, S. Suzuki, M. Asada, "Wide frequency-tunable resonant tunnelling

diode terahertz oscillators using varactor diodes," *Elec. Lett.,* vol. 52, no. 6, pp. 479-481, 2016.

[1.131] S. Kitagawa, S. Suzuki, M. Asada, "650-GHz resonant-tunneling-diode VCO with wide tuning range using varactor diode," *IEEE Elec. Device Lett.,* vol. 35, Art. no. 1215, 2016.

[1.132] M. Shiraishi, H. Shibayama, K. Ishigaki, S. Suzuki, M. Asada, H. Sugiyama, and H. Yokoyama, "High output power (~400 μW) oscillators at around 550 GHz using resonant tunneling diodes with graded emitter and thin barriers," *Appl. Phys. Express,* vol. 4, Art. no. 064101, 2011.

[1.133] S. Suzuki, M. Shiraishi, H. Shibayama, and M. Asada, "High-power operation of terahertz oscillators with resonant tunneling diodes using impedance-matched antennas and array configuration," *IEEE J. Selec. Topics Quantum Elec.,* vol. 19, no.1, Art. no. 8500108, 2013.

[1.134] K. Kobayashi, S. Suzuki, F. Han, H. Tanaka, H. Fujikata, and M. Asada, "Analysis of a high-power resonant-tunneling-diode terahertz oscillator integrated with a rectangular cavity resonator," *Jpn. J. Appl. Phys*., vol. 59, 050907, 2020.

[1.135] H. Fujikata, H. Tanaka, F. Han, A. Ishikawa, S. Suzuki, and M. Asada, "Terahertz oscillator using rectangular-cavity resonator and large-area RTD with heat dissipation structure," *47th International Conference on Infrared, Millimeter and Terahertz Waves (IRMMW-THz)*, Delf, Netherlands, Aug. 2022.

[1.136] K. Kasagi, S. Suzuki and M. Asada, "Large-scale array of resonant-tunneling-diode terahertz oscillators for high output power at 1 THz", *J. Appl. Phys.*, vol. 125, no. 15, Art. no. 151601, 2019.

[1.137] Y. Koyama, Y. Kitazawa, K. Yukimasa, T. Uchida, T. Yoshioka, K. Fujimoto, et al., "A high-power terahertz source over 10 mW at 0.45 THz using an active antenna array with integrated patch antennas and resonant-tunneling diodes", *IEEE Trans. Terahertz Sci. Technol.*, vol. 12, no. 5, pp. 510-519, 2022.

[1.138] S. Iwamatsu, Y. Nishida, M. Fujita, and T. Nagatsuma, “Terahertz coherent oscillator integrated with slot-ring antenna using two resonant tunneling diodes,” *Appl. Phys. Express*, vol. 14, Art. no. 034001, 2021.

[1.139] A. Dobroiu, K. Asama, S. Suzuki, M. Asada, and H. Ito, "Three-dimensional terahertz imaging using an amplitude-modulated resonant-tunneling-diode oscillator,” 2021 *46th Int. Conf. on Infrared, Millimeter, and Terahertz Waves (IRMMW-THz)*, Chengdu, China, Sep. 2021.

[1.140] L. Yi, Y. Nishida, T. Sagisaka, R. Kaname, R. Mizuno, M. Fujita, and T. Nagatsuma, "Towards practical terahertz imaging system with compact continuous wave transceiver,” *J. Light. Technol.*, vol. 39, pp. 7850-7861, 2021.

[1.141] A. Dobroiu, Y. Shirajawa, S. Suzuki, M. Asada, and H. Ito, "Subcarrier frequency-modulated continuous-wave radar in the terahertz range based on a resonant-tunneling-diode oscillator," *Sensors,* vol. 20, Nov. 2020, Art. no. 6848, 2020.

[1.142] A. Alkhalidi, K. Alharbi, J. Wang, E. Wasige, "A compact terahertz source technology for automotive radar and other applications," *2018 19th Int. Radar Sym.*, Jun. 2018.

[1.143] S. Kitagawa, M. Mizuno, S. Saito, K. Ogino, S. Suzuki, and M. Asada, “Frequency-tunable resonant-tunneling-diode terahertz oscillators applied to absorbance measurement,” *Jpn. J. Appl. Phys.,* vol. 56, Art. no. 058002, 2017.

[1.144] M. Kim, J. Lee, J. Lee, and K. Yang, "A 675 GHz differential oscillator based on a resonant tunneling diode," *IEEE Trans. THz Sci. Technol*., vol. 6, no. 3, pp. 510–512, 2016.

[1.145] J. Lee, M. Kim, and K. Yang, "A 1.52 THz RTD triple-push oscillator with a μW -level output power," IEEE Trans. THz Sci. Technol., vol. 6, no. 2, pp. 336–340, 2016.

[1.146] J. Lee, M. Kim, and J. Lee, "692 GHz high-efficiency compact-size InP based fundamental RTD oscillator," *IEEE Trans. Terahertz Sci. Technol*., vol. 11, no. 6, pp. 716–719, 2021.

[1.147] A. Al-Khalidi, K. H. Alharbi, J. Wang, R. Moraiu, L. Wang, A. Khalid, J. Feigueiredo, and E. Wasige, "Resonant Tunneling Diode Terahertz Sources with up to 1 mW Output Power in the J-Band," *IEEE Trans. Terahertz Sci. Technol*., vol. 10, no. 2, pp. 150-157, 2020.

[1.148] H. Jalili, and O. Momeni, "A 0.46-THz 25-Element Scalable and Wideband Radiator Array With Optimized Lens Integration in 65-nm CMOS," *IEEE J. Solid-State*

*Circuits*, vol. 55, no. 9, pp. 2387-2400, 2020.

[1.149] K. Guo, Y. Zhang, and P. Reynaert, "A 0.53-THz subharmonic injection locked phased array with 63-μw radiated power in 40-nm CMOS," *IEEE J. Solid-State Circuits*, vol. 54, no. 2, pp. 380-391, 2018.

[1.150] Y. Yang, O. D. Gurbuz, and G. M. Rebeiz, "An eight-element 370–410-GHz phased-array transmitter in 45-nm CMOS SOI with peak EIRP of 8–8.5 dBm," *IEEE Trans. Micro. Theory and Techniques*, vol. 64, no. 12, pp.4241-4249, 2016.

[1.151] Y. Tousi, and E. Afshari, "A high-power and scalable 2-D phased array for terahertz CMOS integrated systems," *IEEE J. Solid-State Circuits*, vol 50, no 2. Pp. 597-609, 2015.

[1.152] K. Sengupta, A. Hajimiri, "A 0.28 THz power-generation and beamsteering array in CMOS based on distributed active radiators," *IEEE J. Solid-State Circuits*, vol. 47, no. 12, pp. 3013-3031, 2012.

[1.153] R. Han, E. Afshari, "A CMOS high-power broadband 260-GHz radiator array for spectroscopy," *IEEE J. Solid-State Circuits*, vol 48, no. 12, pp. 3090-3104, 2013.

[1.154] S. Jameson, E. Halpern, and E. Socher, "A 300GHz wirelessly locked 2x3 array radiating 5.4dBm with 5.1% DC-to-RF efficiency in 65nm CMOS," *2016 ISSCC*, Feb. 2015.

[1.155] N. Buadana, S. Jameson, and E. Socher, "A 280GHz +9dBm TRP dense 2D multi port radiator in 65nm CMOS," *2018 IEEE RFIC*, Jun. 2018.

[1.156] L. Gao, H. Zhou, K. M. Shum, C. H. Chan, "A 482GHz 2-D Scalable and Wideband Radiator Array," *IEEE Microwave and Wireless Components Letters*, vol. 31, no. 9, pp. 1090-1093, 2021.

[1.157] G. Guimaraes, and P. Reynaert, "A 660-to-676GHz 4×2 oscillator-radiator array with intrinsic frequency-filtering feedback for harmonic power boost achieving 7.4dBm EIRP in 40nm CMOS," *2020 IEEE ISSCC*, Feb. 2020.

[1.158] K. Guo, P. Reynaert, "A 0.59THz Beam-Steerable Coherent Radiator Array with 1mW Radiated Power and 24.1dBm EIRP in 40nm CMOS," *2020 IEEE ISSCC*, Feb. 2020.

[1.159] H. Saeidi, S. Venkatesh, C. R. Chappidi, T. Sharma, C. Zhu, and K. Sengupta, "A 4×4 Distributed Multi-Layer Oscillator Network for Harmonic Injection and THz Beamforming with 14dBm EIRP at 416GHz in a Lensless 65nm CMOS IC," *2020 IEEE ISSCC*, Feb. 2020.

[1.160] Y. Tousi, Y. M. Tousi, O. Momeni, and E. Afshari, "A 283-to-296 GHz VCO with 0.76 mW peak output power in 65 nm CMOS," *2012 IEEE ISSCC*, Feb. 2012.

[1.161] J. Sharma, and H. Krishnaswamy, "216- and 316-GHz 45-nm SOI CMOS signal sources based on a maximum-gain ring oscillator topology," *IEEE Trans. Microwave Theory and Techniques*, vol. 61, no. 1, pp. 492-504, 2013.

[1.162] N. Landsberg, E. Socher, "240 GHz and 272 GHz Fundamental VCOs Using 32 nm CMOS Technology," *IEEE Trans. Microwave and Theory and Techniques*, vol. 61, no 12, pp. 4461-4471, 2013.

[1.163] M. Adnan, and E. Afshari, "A 247-to-263.5 GHz VCO with 2.6 mW peak output power and 1.14% DC-to-RF efficiency in 65 nm bulk CMOS," *2014 IEEE ISSCC*, Feb. 2014.

[1.164] R. Kananizadeh, and O. Momeni, "High-Power and High-Efficiency Millimeter-Wave Harmonic Oscillator Design, Exploiting Harmonic Positive Feedback in CMOS," *IEEE Trans. Microwave Theory and Techniques*, vol. 65, no. 10, pp. 3922-3936, 2017.

[1.165] H. Wang, J. Chen, J. T. S. Do, H. Rashtian, and X. Liu, "High-Efficiency Millimeter-Wave Single-Ended and Differential Fundamental Oscillators in CMOS," *IEEE J. Solid-State Circuits*, vol. 53. no. 8, pp. 2151-2163, 2018.

[1.166] H. Jalili, and O. Momeni, "A 230-GHz High-Power and Wideband Coupled Standing Wave VCO in 65-nm CMOS," *IEEE J. Solid-State Circuits*, vol. 55. no. 3, pp.547-556, 2020.

[1.167] Y. Shu, Y. Shu, H. J. Qian, X. Luo, "A 169.6-GHz Low Phase Noise and Wideband Hybrid Mode-Switching Push–Push Oscillator," *IEEE Trans. Microwave Theory and Techniques*, vol. 67, no. 7, pp. 2769-2781, 2019.

[1.168] H. Jalili, O. Momeni, "A 219-to-238-GHz Coupled Standing-Wave VCO with 3.4-dBm Peak Output Power in 65nm CMOS," *2019 IEEE CICC*, Apr. 2019.

[1.169] T. Chi, H. Wang, M. Y. Huang, F. F. Dai, and H. Wang, "A bidirectional lens-free digital-bits-in/-out 0.57mm2 Terahertz nano-radio in CMOS with 49.3mW peak power consumption supporting 50cm Internet-of-Things communication," *2017 IEEE CICC*,

Apr. 2017.

[1.170] R. Kananizadeh, and O.Momeni, "Second-Harmonic Power Generation Limits in Harmonic Oscillators," *IEEE J. Solid -State Circuits*, vol.53. no.11, pp. 3217-3231, 2018.

[1.171] A. H.M. Ashirazi, A.Nikpaik, S. Mirabbasi, and S. Shekahr, "A quad-core-coupled triple-push 295-to

301 GHz source with 1.25 mW peak output power in 65nm CMOS using slow-wave effect," *2016 IEEE RFIC*, May 2016.

[1.172] A. Nikpaik, A. H. M. Shirazi, A. Nabavi, S. Mirabbasi, and S. Shekhar,"A 219-to-231 GHz Frequency-Multiplier-Based VCO with ~3% Peak DC-to-RF Efficiency in 65-nm CMOS," *IEEE J. Solid-State Circuits*, vol.53, no.2, pp. 389-403, 2018.

[1.173] O. Momeni, and E. Afshari, "High power terahertz and millimeter-wave oscillator design: A systematic approach," *IEEE J. Solid-State Circuits,* vol.46, no.3, pp. 583-597, 2011.

[1.174] H. Koo, C.Y. Kim, and S. Hong, "Design and analysis of 239 GHz CMOS push-push transformer-based VCO with high efficiency and wide tuning range," *IEEE Trans. Circuits and Sysytems I: Regular Papers*, vol.62, no.7, pp. 1883-1893, 2015.

[1.175] J. Grzyb, Y. Zhao, U. R. Pfeiffer, "A 288-GHz lens-integrated balanced triple-push source in a 65-nm CMOS technology," *IEEE J. Solid-State Circuits*, vol.48, no.7, 2013.

[1.176] S. Jameson, and E. Socher, "High efficiency 293 GHz radiating source in 65 nm

CMOS," *IEEE Microwave and Wireless Components Letters*, vol.24, no.7, pp. 463-465, 2014.

[1.177] Z. Wang, P.Y. Chiang, P. Nazari, C.C. Wang, Z. Chen, and P. Heydari, "A CMOS 210-GHz fundamental transceiver with OOK modulation," *IEEE J. Solid-State Circuits*, vol.49, no.3, pp. 564-580, 2014.

[1.178] Z. Chen, Z. Chen, W, Choi, and K. O. Kenneth, "610-GHz fourth harmonic signal reactively generated in a CMOS voltage controlled oscillator using differentially pumped varactors," *IEEE Solid-State Circuits Letters*, vol.3, pp. 46-49, 2020.

[1.179] G. Guimaraes, and P. Reynaert, "A 660-to-676GHz 4×2 oscillator-radiator array with intrinsic frequency-filtering feedback for harmonic power boost achieving 7.4dBm EIRP in 40nm CMOS," *2020 IEEE ISSCC*, Feb. 2020.

[1.180] D. Simic, K. Guo, and P. Reynaert, "A 420-GHz Sub-5-μm Range Resolution TX–RX Phase Imaging System in 40-nm CMOS Technology," *IEEE J. Solid-State Circuits*, vol.56, no.12, pp. 3827-3839, 2021.

[1.181] L. Gao, et.al., "A 0.68-0.72-THz 2-D Scalable Radiator Array With -3-dBm Radiated Power and 27.3-dBm EIRP in 65-nm CMOS," *IEEE J. Solid-State Circuits*, vol. 57, no. 10, 2022.

[1.182] H. Saeidi, H. S. Venkatesh, C. R. Chappidi, T. Sharma, C. Zhu, and K. Sengupta, "A 4 × 4 Steerable 14-dBm EIRP Array on CMOS at 0.41 THz with a 2-D Distributed Oscillator Network," *IEEE J. Solid-State Circuits*, vol.57, no.10, pp. 3125-3138, 2022.

[1.183] L. Gao, and C. H. Chan, "A 0.45-THz 2-D Scalable Radiator Array with 28.2-dBm EIRP Using an Elliptical Teflon Lens," *IEEE J. Solid-State Circuits*, vol.57, no.2, pp. 400-412, 2022.

[1.184] M. W. Mansha, and M. Hella, "A 7.4dBm EIRP, 20.2% DC-EIRP Efficiency 148GHz Coupled Loop Oscillator with Multi-Feed Antenna in 22nm FD-SOI," 2020 *IEEE RFIC*, Aug. 2020.

[1.185] H. Jalili, O. Momeni, "A 0.34-THz wideband wide-angle 2-D steering phased array in 0.13-μ m SiGe BiCMOS," *IEEE J. Solid-State Circuits*, vol.54. no.9, pp. 2449-2461, 2019.

[1.186] H. Jalili, and O. Momeni, "A standing-wave architecture for scalable and wideband millimeter-wave and terahertz coherent radiator arrays," *IEEE Trans. Microwave Theory and Techniques*, vol.66. no.3, pp. 1597-1609, 2018.

[1.187] R. Han, C. Jiang, A. Mostajeran, M. Emadi, H. Aghasi, H. Sherry, A. Cathelin, and E. Afshari, "A SiGe terahertz heterodyne imaging transmitter with 3.3 mW radiated power and fully-integrated phase-locked loop," *IEEE J. Solid-State Circuits*, vol.50, no.12, pp. 2935-2947, 2015.

[1.188] R. Jain, P. Hillger, J. Grzyb, and U. R. Pfeiffer, "A 0.42THz 9.2dBm 64-Pixel Source-Array SoC with Spatial Modulation Diversity for Computational Terahertz Imaging," *2020 ISSCC*, Feb. 2020.

[1.189] P. Hillger, J. Grzyb, S. Malz, B. Heinemann, and U. Pfeiffer, "A Lens-Integrated

430 GHz SiGe HBT Source with up to −6.3 dBm Radiated Power," *2017 IEEE RFIC*, Jun. 2017.

[1.190] P. Y. Chiang, O. Momeni, P. Heydari, "A 200-GHz Inductively Tuned VCO with 7-dBm," *IEEE Trans. Microwave Theory and Techniques*, vol.61, no.10, pp. 3666-3673, 2013.

[1.191] C. Jiang, A. Cathelin, and E. Afshari, "An efficient 210 GHz compact harmonic oscillator with 1.4 dBm peak output power and 10.6% tuning range in 130 nm BiCMOS," *2016 IEEE RFIC*, May 2016.

[1.192] A. Mostajeran, and E. Afshari, "An ultra-wideband harmonic radiator with a tuning range of 62 GHz (28.3%) at 220 GHz," *2017 IEEE RFIC*, Jun. 2017.

[1.193] R. Kanazizadeh, and O. Momeni, "A 190-GHz VCO with 20.7% Tuning Range Employing an Active Mode Switching Block in a 130 nm SiGe BiCMOS," *IEEE J. Solid-State Circuits*, vol.52, no. 8, pp. 2094 – 2104, 2017.

[1.194] H. Khatibi, S. Khiyabani, A. Cathelin, E. Afshari, "A 195 GHz single-transistor fundamental VCO with 15.3% DC-to-RF efficiency,4.5 mW output power, phase noise FoM of −197 dBc/Hz and 1.1% tuning range in a 55 nm SiGe process," *2017 IEEE RFIC*, Jun. 2017.

[1.195] H. Khatibi, S. Khiyabani, and E. Afshari, "An Efficient High-Power Fundamental Oscillator Above fmax/2: A Systematic Design," *IEEE Trans. Microwave Theory and Techniques*, vol.65, no.11, pp. 4176-4189, 2017.

[1.196] F. Ahmed, M. Furquan, B. Heinemann, and A. Stelzer, "0.3-THz SiGe-Based High-Efficiency Push–Push VCOs with > 1-mW Peak Output Power Employing Common-Mode Impedance Enhancement," *IEEE Trans. Microwave Theory and Techniques*, vol. 66, no. 3, pp. 1384-1398, 2018.

[1.197] M. H. Eissa, M. Eissa, A. Awny, M. Ko, K. Schmalz, M. Elkhouly, A. Malignaggi, A. C. Ulusoy, D. Kissinger, "A Compact 275 GHz Harmonic VCO with -2.6 dBm Output Power in a 130 nm SiGe Process," *IEEE Microwave and Wireless Components Letters*, vol. 27, no. 7, 2017.

[1.198] S. P. Voinigescu, A. Tomkins, E. Dacquay, P. Chevalier, J. Hasch, A. Chantre, and B. Sautreil, "A study of SiGe HBT signal sources in the 220–330-GHz range," *IEEE J. Solid-State Circuits*, vol.48, no.9, pp. 2011-2021, 2013.

[1.199] J. Grzyb, J. Grzyb, B. Heinemann, U.R. Pfeiffer, "Solid-state terahertz superresolution imaging device in 130-nm SiGe BiCMOS technology," *IEEE Trans. Microwave Tehory and Techniques*, vol. 65, no.11, pp. 4357-4372, 2017.

[1.200] J. Yun, D. Yoon, S. Jung, M. Kaynak, B. Tillack, J.S. Rieh, "Two 320 GHz signal sources based on SiGe HBT technology," *IEEE Microwave and Wireless Components Letters,* vol.25, no.3, pp. 178-180, 2015.

[1.201] P. Zhou, J. Chen, P. Yan, Z. Chen, D. Hou, and W. Hong, "A 273.5–312-GHz Signal Source with 2.3 dBm Peak Output Power in a 130-nm SiGe BiCMOS Process," *IEEE Trans. THz Sci. and Technol.*, vol. 10, no.3, pp. 260-270, 2020.

[1.202] A. Gadallah, M. H. Eissa, D. Kissinger, and A. Malignaggi, "A 250-300 GHz Frequency Multiplier-by-8 Chain in SiGe Technology," *2022 IMS*, Jun. 2022.

[1.203] S. Razavian, and A. Babakhani,"A Highly Power Efficient 2×3 PIN-Diode-Based Intercoupled THz Radiating Array at 425GHz with 18.1dBm EIRP in 90nm SiGe BiCMOS," *2022 ISSCC*, Feb. 2022.

[1.204] M. Kucharski, M. Kucharski, M. H. Eissa, A. Malignaggi, D. Wang, H. Jalli, and D. Kissinger, "D-Band Frequency Quadruplers in BiCMOS Technology," *IEEE J. Solid-State Circuits*, vol. 53, no. 9, pp. 2465-2478, 2018.

[1.205] J. Hu, M. Kaynak, R. Han, "High-power radiation at 1 THz in silicon: A fully scalable array using a multi-functional radiating mesh structure," *IEEE J. Solid-State Circuits,* vol.53, no.5, pp. 1313-1327, 2018.

[1.206] J. Kim, J. Kim. D. Yoon, H. Son, D. Kim, J. Yoo, J. Yun, H. Jalli, M. Kaynal, J. S. Rieh, "Terahertz Signal Source and Receiver Operating Near 600 GHz and Their 3-D Imaging Application," *IEEE Trans. Microwave. Theo. Tech*., vol. 69, no. 5, pp. 2762-2775, 2021.

[1.207] D. Kim, and S. Jeon, "A WR-3 Band Fundamental Voltage-Controlled Oscillator with a Wide Frequency Tuning Range and High Output Power," *IEEE transaction on Microwave theory and techniques*, vol.67, no.7, pp. 2759-2768, 2019.

[1.208] J. Yun, N. Kim, D. Yoon, H. Kim, S. Jeon, and J.S. Rieh, "A 248-262 GHz InP HBT VCO with Interesting Tuning Behavior," *IEEE Microwave and Wireless*

*Components Letters*, vol.24, no.8, pp. 560-562, 2014.

[1.209] V. Radisic, L. Samoska, W.R.Deal, X.B. Mei, W. Yoshida, P. H. Liu, J. Uyeda, A. Fung, T. Gaier, and R. Lai, "A 330-GHz MMIC oscillator module," *2008 IEEE IMSD*, Jun. 2008.

[1.210] K. Song, J. Kim, H. Son, J. Yoo, M. Cho, and J.S. Rieh, "300-GHz InP HBT Quadrature VCO with Integrated Mixer," vol.10, no.4, *IEEE Trans. THz Sci. Technol*., vol.10, no.4, pp. 419-422, 2020.

[1.211] D. Yoon, J. Yun, and J.S. Rieh, "A 310–340-GHz coupled-line voltage controlled oscillator based on 0.25-μm InP HBT technology," *IEEE Trans. THz. Sci. Technol*., vol.5, no.4, pp. 652-654, 2015.

[1.212] O. Inac, M. Uzunkol, and G. M. Rebriel, “45-nm CMOS SOI Technology Characterization for Millimeter-Wave Applications,” *IEEE Trans. THz. Sci. Technol*., vol.62, no.6, pp. 1301-1311, 2014.

[1.213] B. Heinemann, H. Rucker, R. Barth, F. Barwolf, J. Drews, G. G. Fischer, A. Fox, O. Fursenko, T. Grabolla, F. Herzel, J. Katzer, J. Korn, A. Kruger, P. Kulse, T. Lenke, M. Lisker, S. Marschmeyer, A. Scheit, D. Schmidt, M.A Schubert, A. Trusch, A. Trusch, C. Wipf, and D. Wolansky, “SiGe HBT with fx/fmax of 505 GHz/720 GHz,” *2016 IEDM*, Dec. 2016.

[1.214] H. Kanaya, T. Maekawa, S. Suzuki, and M. Asada, “Structure dependence of oscillation characteristics of resonant-tunneling-diode terahertz oscillators associated

with intrinsic and extrinsic delay times," *Jpn. J. Appl. Phys*., vol. 54, Art. no. 094103, 2015.

[1.215] R. Izumi, T. Sato, S. Suzuki, and M. Asada, "Resonant-tunneling-diode terahertz oscillator with a cylindrical cavity for high-frequency oscillation," *AIP Advances*., vol. 9, Art. no. 085020, 2019.

[1.216] P. Ourednik, T. Hackl, C. Spudat, D. T. Nguyen, and M. Feiginov, "Double-resonant-tunneling-diode patch-antenna oscillators," *Appl. Phys. Lett*. vol. 119, art.no. 263509, 2021.

[1.217] P. Ourednik, and M. Feiginov, "Double-resonant-tunneling-diode patch-antenna oscillators," *Appl. Phys. Lett*. vol. 120, art.no. 183501, 2022.

## Chapter 2

[2.1] M. Asada, and S. Suzuki, "Terahertz Emitter Using Resonant-Tunneling Diode and Applications," *Sensors,* vol. 21, Art. no. 1384, 2021.

[2.2] H. Kanaya, H. Shibayama, R. Sogabe, S. Suzuki, and M. Asada, "Fundamental Oscillation up to 1.31 THz in Resonant Tunneling Diodes with Thin Well and Barriers," *Appl. Phys. Express,* vol.5, Art. no. 124101, 2012.

[2.3] K. Kobayashi, S. Suzuki, F. Han, H. Tanaka, H. Fujikata, and M. Asada, "Analysis of a high-power resonant-tunneling-diode terahertz oscillator integrated with a

rectangular cavity resonator," *Jpn. J. Appl. Phys*., vol. 59, Art. no. 050907, 2020.

[2.4] R. Izumi, T. Sato, S. Suzuki, and M. Asada, "Resonant-tunneling-diode terahertz oscillator with a cylindrical cavity for high-frequency oscillation," *AIP Advances*., vol. 9, Art. no. 085020, 2019.

[2.5] T. Maekawa, H. Kanaya, S. Suzuki, M. Asada, "Frequency increase in terahertz oscillation of resonant tunnelling diode up to 1.55 THz by reduced slot-antenna length," *Appl. Phys. Lett.,* vol. 104, Art. no. 243509, 2014.

[2.6] T. Maekawa, H. Kanaya, S. Suzuki, and M. Asada, "Oscillation up to 1.92 THz in resonant tunneling diode by reduced conduction loss," *Appl. Phys. Express*, vol. 9, Art. no. 024101, 2016.

[2.7] H. Kanaya, "Study of Resonant-Tunneling-Diode Terahertz Oscillators for High Frequency," *Tokyo Institute of Technology, Doctor Thesis*., Dec., 2015.

[2.8] H. Kanaya, T. Maekawa, S. Suzuki, and M. Asada, "Structure dependence of oscillation characteristics of resonant-tunneling-diode terahertz oscillators associated with intrinsic and extrinsic delay times," *Jpn. J. Appl. Phys*., vol. 54, Art. no. 094103, 2015.

[2.9] M. Asada, S. Suzuki, and N. Kishimoto, "Resonant tunneling diodes for sub-terahertz and terahertz oscillators," *Jpn. J. Appl. Phys*., vol. 47, no. 6, pp. 4375-4384, 2008.

## Chapter 3

[3.1] K. Hinata, M. Shiraishi, S. Suzuki, M. Asada, H. Sugiyama, and H. Yokoyama, "Sub-terahertz resonant tunneling diode oscillators with high output power (~200μW) using offset-fed slot antenna and high current density," *Appl. Phys. Express,* vol. 3, Art. no. 014001, 2010.

[3.2] M. Shiraishi, H. Shibayama, K. Ishigaki, S. Suzuki, M. Asada, H. Sugiyama, and H. Yokoyama, "High output power (∼400 μW) oscillators at around 550 GHz using resonant tunneling diodes with graded emitter and thin barriers," *Appl. Phys. Express,* vol. 4, Art. no. 064101, 2011.

[3.3] S. Suzuki, M. Shiraishi, H. Shibayama, and M. Asada, "High-power operation of terahertz oscillators with resonant tunneling diodes using impedance-matched antennas and array configuration," *IEEE J. Selec. Topics Quantum Elec.,* vol. 19, no.1, Art. no. 8500108, 2013.

[3.4] C. P. Yue; S. S. Wong, "Physical modeling of spiral inductors on silicon," *IEEE Trans. Elec. Devices,* vol. 47, no. 3, pp. 560-568, 2000.

[3.5] X. Yu, Y. Suzuki, M. V. Ta, S. Suzuki, and M. Asada, "Highly efficient resonant tunneling diode terahertz oscillator with a split ring resonator," *IEEE Electron Device Letters,* vol. 42, no. 7, pp. 982-985, 2021.

## Chapter 4

[4.1] S. Suzuki, A. Teranishi, K. Hinata, M. Asada, H. Sugiyama, and H. Yokoyama, "Fundamental Oscillation of up to 831 GHz in GaInAs/AlAs Resonant Tunneling Diode," *Appl. Phys. Express,* vol. 2, Art. no. 054501, 2009.

[4.2] S. Suzuki, M. Asada, A. Teranishi, H. Sugiyama, and H. Yokoyama, "Fundamental oscillation of resonant tunneling diodes above 1 THz at room temperature," *Appl. Phys. Lett.,* vol. 97, Art. no. 054501, 2010.

[4.3] H. Kanaya, H. Shibayama, R. Sogabe, S. Suzuki, and M. Asada, "Fundamental Oscillation up to 1.31 THz in Resonant Tunneling Diodes with Thin Well and Barriers," *Appl. Phys. Express,* vol.5, Art. no. 124101, 2012.

[4.4] M. Feiginov, H. Kanaya, S. Suzuki, and M. Asada, "1.46 THz RTD oscillators with strong back injection from collector," *Appl. Phys. Lett.,* vol. 104, Art. no. 243509, 2014.

[4.6] T. Maekawa, H. Kanaya, S. Suzuki, M. Asada, "Frequency increase in terahertz oscillation of resonant tunnelling diode up to 1.55 THz by reduced slot-antenna length," *Appl. Phys. Lett.,* vol. 104, Art. no. 243509, 2014.

[1.7] Y. Koyama, R. Sekiguchi, and T. Ouch, "Oscillations up to 1.40 THz from resonant-tunneling-fiode-based oscillators with integrated patch antennas," *Appl. Phys. Express,* vol. 6, Art. no. 064102, 2013.

[4.8] S. Iwamatsu, Y. Nishida, M. Fujita, and T. Nagatsuma, "Terahertz coherent oscillator integrated with slot-ring antenna using two resonant tunneling diodes," *Appl. Phys.*

*Express*, vol. 14, Art. no. 034001, 2021.

[4.9] H. Kanaya, T. Maekawa, S. Suzuki, and M. Asada, “Structure dependence of oscillation characteristics of resonant-tunneling-diode terahertz oscillators associated with intrinsic and extrinsic delay times,” *Jpn. J. Appl. Phys.* vol. 54, Art. no. 094103, 2015.

[4.10] N. Shimizu, T. Waho, and T. Ishibashi, “Capacitance anomaly in the negative differential resistance region of resonant tunneling diodes,” *Jpn. J. Appl. Phys.* vol. 36, Art. no. L330, 1997.

[4.11] S. Suzuki, M. Shiraishi, H. Shibayama, and M. Asada, “High-power operation of terahertz oscillators with resonant tunneling diodes using impedance-matched antennas and array configuration,” *IEEE J. Selec. Topics Quantum Elec.,* vol. 19, no.1, Art. no. 8500108, 2013.

[4.12] F. Han, K. Kobayashi, S. Suzuki, H. Tanaka, H. Fujikata, and M. Asada, “Impedance matching in high-power resonant-tunneling-diode terahertz oscillators integrated with rectangular-cavity resonator,” *IEICE Trans. Electron.,* Vol. E104–C, no.8, 2021.

[4.13] K. Kasagi, S. Suzuki and M. Asada, "Large-scale array of resonant-tunneling-diode terahertz oscillators for high output power at 1 THz", *J. Appl. Phys.*, vol. 125, no. 15, Art. no. 151601, 2019.

[4.14] P. Ourednik, T. Hackl, C. Spudat, D. Tuan Nguyen, and M. Feiginov, “Double-

resonant-tunneling-diode patch-antenna oscillators,” *Appl. Phys. Lett*. vol. 119, Art. no. 263509, 2021.

[4.15] S. Suzuki and M. Asada, "Coherent power combination in highly integrated resonant tunneling diode oscillators with slot antenna," *Jpn. J. Appl. Phys.*, vol. 46, Art. no. L110, 2007.

[4.16] Y. Koyama, Y. Kitazawa, K. Yukimasa, T. Uchida, T. Yoshioka, K. Fujimoto, et al., "A high-power terahertz source over 10 mW at 0.45 THz using an active antenna array with integrated patch antennas and resonant-tunneling diodes", *IEEE Trans. Terahertz Sci. Technol.*, vol. 12, no. 5, pp. 510-519, 2022.

[4.17] M. Asada, and S. Suzuki, “Theoretical analysis of coupled oscillator array using resonant tunneling diodes in subterahertz and terahertz range,” *J. Appl. Phys*., vol. 103, Art. no. 124514, 2008.

[4.18] M. S. Li, S. Suzuki, C. Fumeaux, and W. Withayachumnankul, "Improving the Radiation Performance of Resonant-Tunneling Diode by Using Planar Metallic Arrays," *46th International Conference on Infrared, Millimeter and Terahertz Waves (IRMMW-THz)*, Chengdu, China, Aug. 2021.

[4.19] M. S. Li, T. V. Mai, C. Fumeaux, S. Suzuki, and W. Withayachumnankul, “Terahertz resonant-tunneling diode with series-fed patch antenna,” *submitted to IEEE Trans. Terahertz Sci. Technol.*

## Chapter 5

[5.1] M. Asada, and S. Suzuki, "Terahertz Emitter Using Resonant-Tunneling Diode and Applications," *Sensors,* vol. 21, Art. no. 1384, 2021.

[5.2] R. Izumi, T. Sato, S. Suzuki, and M. Asada, "Resonant-tunneling-diode terahertz oscillator with a cylindrical cavity for high-frequency oscillation," *AIP Advances*., vol. 9, Art. no. 085020, 2019.

[5.3] M. Bezhko, S. Suzuki, and M. Asada, "Frequency increase in resonant-tunneling diode cavity-type terahertz oscillator by simulation-based structure optimization," *Jpn. J. Appl. Phys.* vol. 59, Art. no. 032004, 2020.

[5.4] T. V. Mai, Y. Suzuki, X. Yu, S. Suzuki, and M. Asada, "Structure dependence of oscillation characteristics of structure-simplified resonant-tunneling-diode terahertz oscillator," *Appl. Phys. Express* vol. 15, Art. no. 042003, 2022.

# Appendix: Fabrication process and measurement systems

## Fabrication process

**0 Wafer preparation:**

0.1 Wafer cutting:

- Use graph squared paper and glass for alignment.
- Use surgery knife for cutting.
- Cut the wafer with a dimension of 10mm x 15mm.
- Note: mark the back side with an arrow.

0.2 Wafer cleaning

a) Cleaning by Deionized (DI) water ( >18 MΩ) , 8 times flashing in a beaker

b) 5-min ultrasonic cleaning (power 40%)

Repeat a→b 2times

Memo: If the ultra sonic power is over 50%, the wafer may be broken and if there is insufficient water in the bass of ultra sonic machine→ add DI water.

c) Cleaning by acetone and methyl to remove organic imputities

Methyl cleaning 3 times

Acetone cleaning 3 times

Acetone boiling 2 times (Temp. 130 ℃, 5 min)

Memo: Cooling by an acetone beam before pick up a beaker to avoid explosive boil

Methyl cleaning 2 times

Dry by N2 Gun

Memo: If air moisture appears on the wafer surface, repeat methyl cleaning.

**1 Device evaporation**

1.1 Resist coating

Note: Blow the wafer by a rubber blower to remove dust before coating the bottom layer resist.

Bottom layer resist: PMGI SF9

Spin coating: 2500 rpm 60sec (thickness ~650 nm).

Pre-baking: Hotplate 180°C 5 min.

Note: wait for ~ 2 minutes before coating the top layer resist.

Top layer resist: ZEP 520 Spin coating: 2000 rpm 60 sec (~500 nm).

Pre-baking: hotplate 180°C 5 min.

1.2 Electron beam (EB) exposure.

Machine: JEOL JBX6300

Exposure value: 150 $\mu C/cm^2$ @ 100 kV EB.

Exposure current: 15nA, EOS 3.

Shot pitch: 40

1.2 Resist development

- Top layer resist development.

Developer: Xylene,

Time: 3.5 min, with stirring.

Rinse by Isopropyl alcohol (IPA) 2-propanol, 15 sec, with stirring.

Note: Check the pattern by a microscope.

- Bottom layer development

Developer: MFCD-26,

Time: 15 sec, without stirring

Rinse by pure water 2 mins (2 set with 2 beakers), without stirring.

Check the pattern by a microscope.

Develop for 8-10 sec more, check the pattern by a microscope.

Stop when the undercut is clearly seen.

1.3 Surface cleaning

- O2 ashing for removing resist residues:

  Flow meter value: 50 sccm;

  Power: 50 W;

  Time: 1 min.

- Surface treatment for a good contact resistance:

  Cleaning liquid: HCL:H2O = 1:5 (<4°C, cooling by ice);

  Time: 2 min without stirring;

  dry with N2 gun blower;

  Note: Set the wafer in the chamber of the electron-beam evaporator right after surface treatment.

1.4 Evaporation of device electrodes.

Evaporator: Electron-beam evaporator (old E-gun)

Voltage: 4 kV

Degree of vacuum: < 1 x $10^{-6}$ Torr.

Materials: Ti/Pd/Au = 20/20/500 nm in this order.

Note: evacuate the chamber in the afternoon and perform evaporation in the next morning.

Check the remaining amount of materials and the crystal.

Wait for at least 5 mins for the next material.

**2 Lift-off**

Remover: ZDMAC or DMAC.

Immerse the wafer into the remove and put the beaker on the heater ($130^0$) for 4 hours.

Clean by an acetone beam and then by methanol.

Note: after lift-off check the pattern by a microscope, measure dimensions and check the thickness of the deposited metal composition.

**3 Electron beam (EB) exposure for dry-etching mask**

3.1 Resist coating

Note: Blow the wafer by a rubber blower to remove dust before coating the bottom layer resist.

Bottom layer resist: PMGI SF6

Spin coating: 3000 rpm 60sec (thickness ~350 nm).

Pre-baking: Hotplate 250℃ 5 min.

Note: wait for ~ 2 minutes before coating the top layer resist.

Top layer resist: ZEP 520 Spin coating: 2000 rpm 60 sec (~500 nm).

Pre-baking: hotplate 180℃ 5 min.

3.2 Electron beam (EB) exposure.

Machine: JEOL JBX6300

Exposure value: 150 $\mu C/cm^2$ @ 100 kV EB.

Exposure current: 15nA, EOS 3.

Shot pitch: 40

**4. Dry-etching mask formation**

Resist development

- Top layer resist development.

Developer: Xylene,

Time: 3.5 min, with stirring.

Rinse by Isopropyl alcohol (IPA) 2-propanol, 15 sec, with stirring.

Note: Check the pattern by a microscope.

- Bottom layer development

Developer: MFCD-26,

Time: 15 sec, without stirring

Rinse by pure water 2 mins (2 set with 2 beakers), without stirring.

Check the pattern by a microscope.

Develop for 8-10 sec more, check the pattern by a microscope.

Stop when a clear pattern of the resist mask is obtained.

**5. Dry-etching (Reactive ion etching-RIE)**

Model: RIE-10NR (Samco).

Mask: ZEP resist.

Etching recipe (each set):

| **Step No.** | **Step 1** | **Step 2** |
|---|---|---|
| O2 | | 30sccm |
| CH4 | 10sccm | |
| H2 | 40sccm | |
| Pressure | 6 Pa | 10 Pa |
| Power | 100W | 50W |
| Time | 2 min | 50 sec |

Dry etching by RIE for 10 sets;

Check the resist condition by a microscope;

Check the resist thickness and the etching depth by thickness measurement;

Remove the resist by ZDMAC/DMAC remover (boiling on a $130^0$ heater for 10 min);

Clean by acetone and methanol.

**6. Wet-etching**

Check the metal height and I-V characteristics of TLM pattern before etching

Etchant: H2SO4:H2O2:H2O=1:1:80 (< $3^0$)

Time: 30 sec each; total time: 7~8 mins depend

Rinse: DI water, 15 sec, 2 beakers;

Check the etching depth after each time

# Measurement systems

## 1. Oscillation frequency measurement system.

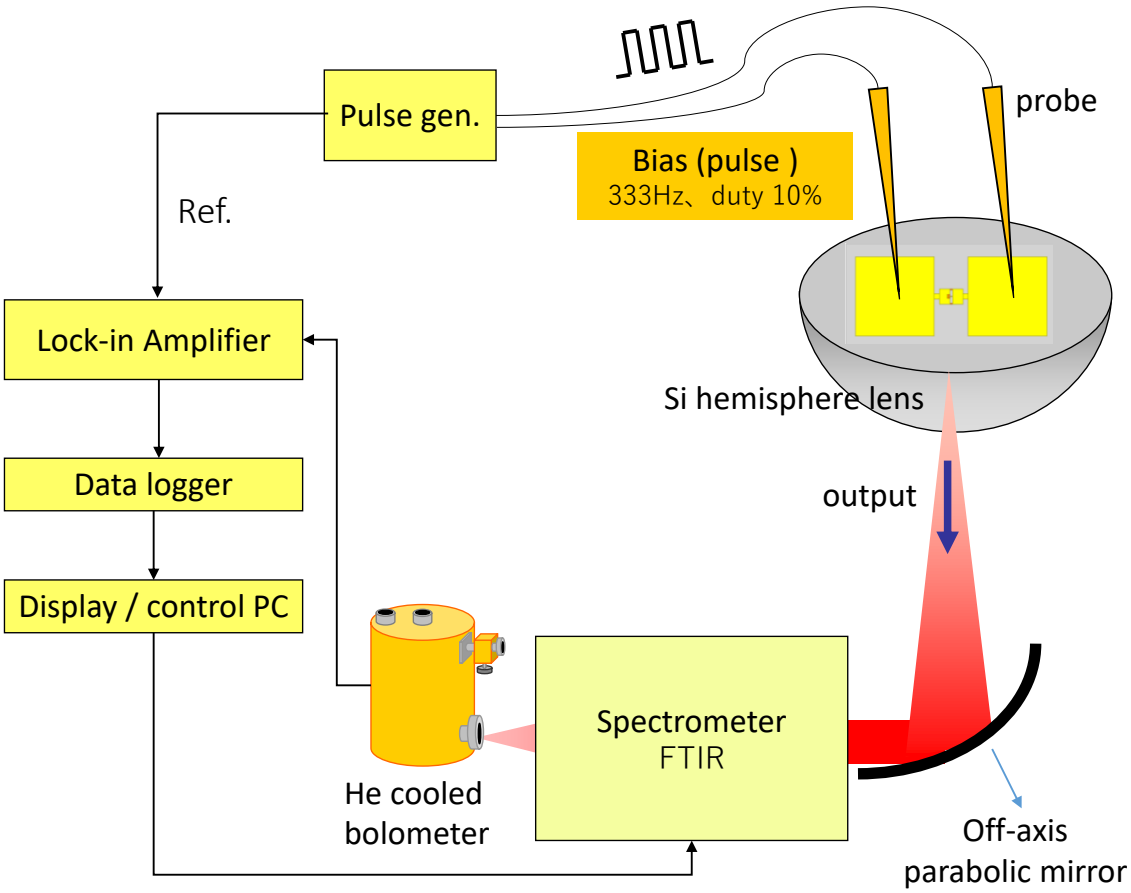


The oscillation frequency is measured using a Fourier transform infrared spectrometer (FTIR) (JASCO FARIS-1). The RTD chip is placed on a hemispherical Si lens (with a 30 mm diameter). The radiated THz wave of the RTD oscillator was collected using a parabolic mirror and converted into a collimated beam before reaching the FTIR system. The THz oscillation intensity is detected by the bolometer using the lock-in technique to reduce the surrounding noise. A moving mirror of the interferometer inside the FTIR system rapidly moves back and forth during the measurement. As a result, the detected

intensity of the THz oscillation changes with the moving mirror position due to wave interference. The THz oscillation intensity against the mirror position is called the raw data. Based on this raw data, a computer program performs the Fourier transform for obtaining the oscillation spectrum.

**2. Output power measurement system.**

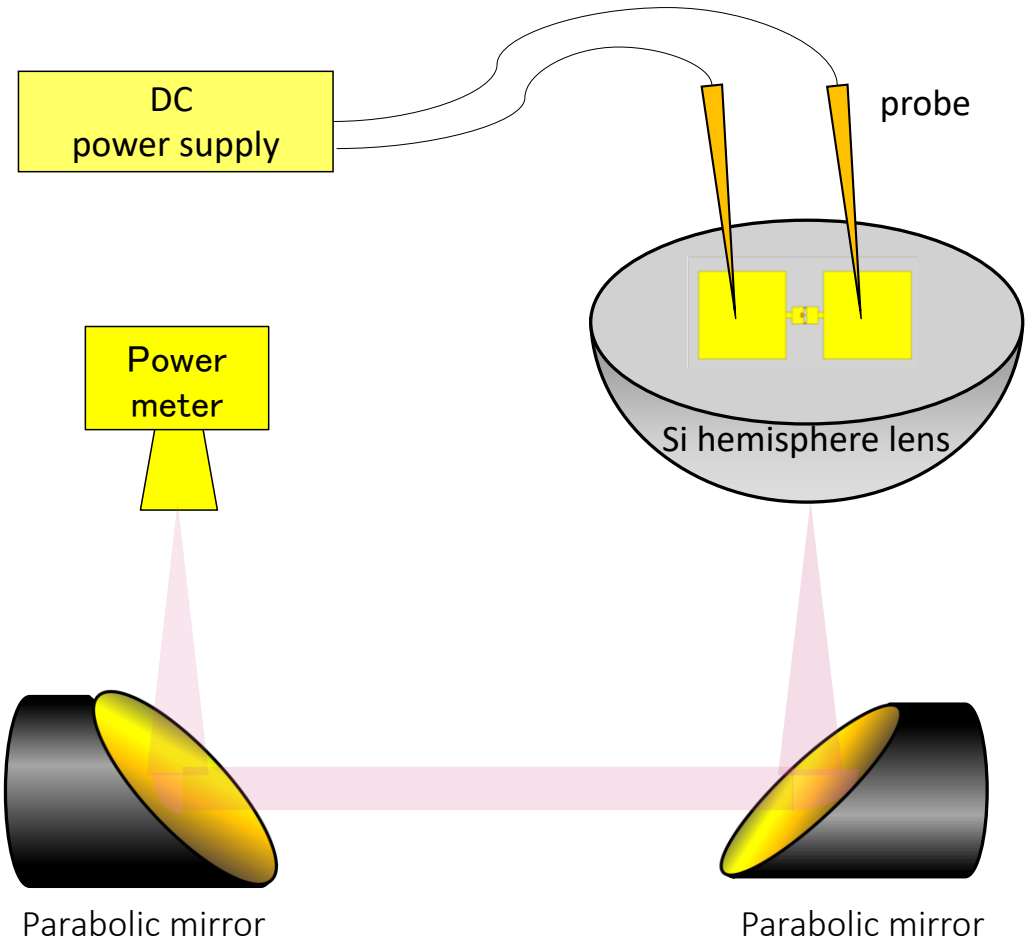


To measure the output power, the RTD chip is placed on a hemispherical Si lens (with a 30 mm diameter). The radiated THz wave of the RTD oscillator was collected using a parabolic mirror and converted into a collimated beam. The collimated THz wave was then reflected by another parabolic mirror and focused on the horn antenna of a PM5 power meter (Virginia Diodes). The measured output power was then corrected taking into account the radiation pattern of the RTD oscillator, and the Fresnel reflection loss at the interface between Si lens and the air.

# Publication list

■ **Journal papers:**

1. T. V. Mai, Y. Suzuki, X. Yu, S. Suzuki, and M. Asada, "Structure-simplified resonant tunneling diode terahertz oscillator without metal-insulator-metal capacitors," *Journal of Infrared, Millimeter, and Terahertz Waves*, vol. 41, no. 12, pp. 1498–1507, 2020.

2. T. V. Mai, Y. Suzuki, X. Yu, S. Suzuki, and M. Asada, "Structure dependence of oscillation characteristics of structure-simplified resonant-tunneling-diode terahertz oscillator," *Applied Physics Express*, vol. 15, no. 4, pp. 042003, 2022.

3. X. Yu, Y. Suzuki, T. V. Mai, S. Suzuki, and M. Asada, "Highly efficient resonant tunneling diode terahertz oscillator with a split ring resonator," *IEEE Electron Device Letters*, vol. 42, no. 7, pp. 982–985, 2021.

4. Y. Suzuki, X. Yu, T. V. Mai, S. Suzuki, and M. Asada, "Phase control of terahertz waves using injection-locked resonant tunneling diode oscillator," *IEEE Transaction on Terahertz Science and Technology*, vol. 42, no. 7, pp. 982–985, 2021.

5. M. S. Li, T. V. Mai, C. Fumeaux, S. Suzuki, and W. Withayachumnankul, "Terahertz resonant-tunneling diode with series-fed patch antenna," *IEEE Transaction on Terahertz Science and Technology*, Early access, Jan. 2023. doi:10.1109/TTHZ.2023.3239809.

6. T. V. Mai, M. Asada, T. Namba, Y. Suzuki, and S. Suzuki, "Coherent power combination in a resonant-tunneling-diode arrayed oscillator with simplified structure," submitted to *IEEE Transaction on Terahertz Science and Technology*.

■ **International conference:**

1. T. V. Mai, Y. Suzuki, S. Suzuki, and Masahiro Asada, "Novel RTD Oscillator with Simplified Structure and Fabrication Process," *the 45th International Conference on Infrared, Millimeter, and Terahertz Waves (IRMMW-THz)*, Newyork, USA, Nov. 2020.

2. T. V. Mai, Y. Suzuki, X. Yu, K. Kozaka, S. Suzuki, and Masahiro Asada, "Structure Dependence of Resonant Tunneling Diode Oscillator without Metal-Insulator-Metal Capacitors," *the 46th International Conference on Infrared, Millimeter, and Terahertz Waves (IRMMW-THz)*, Chengdu, China, Sep. 2021.

3. Y. Suzuki, T. V. Mai, X. Yu, S. Suzuki, and Masahiro Asada, "Phase Control of Injection-Locked RTD Terahertz Oscillator," *the 46th International Conference on Infrared, Millimeter, and Terahertz Waves (IRMMW-THz),* Chengdu, China, Sep. 2021.

4. X. Yu, T. Miyagawa, Y. Suzuki, T. V. Mai, S. Suzuki, and Masahiro Asada, "Perimeter Dependence of Oscillation Frequency Property of Resonant Tunneling Diode Terahertz Oscillator Using Split Ring Resonator," *the 46th International Conference on Infrared, Millimeter, and Terahertz Waves (IRMMW-THz),* Chengdu, China, Sep. 2021.

5. T. V. Mai, T. Namba, Y. Suzuki, S. Suzuki, and M. Asada, "Resonant-Tunneling-Diode Oscillator Array with Zigzag Arrangement for Terahertz Power Combination," *the 9th Russia-Japan-USA-Europe Symposium on fundamental & applied problems of Terahertz devices & technologies*, Sendai, Japan, Nov. 2021.

6. T. V. Mai, T. Namba, Y. Suzuki, S. Suzuki, and M. Asada, "Array Configuration for High Output Power in Structure-simplified Resonant-Tunneling-Diode Terahertz Oscillator," *the 3rd International Symposium on Frontiers in THz technology*, Fukui, Japan, Nov. 2022.

■ **Domestic conference:**

1. T. V. Mai, Y. Suzuki, S. Suzuki, and Masahiro Asada, "Simplification in Device Structure and Fabrication Process of RTD THz Oscillator," *the 67th JSAP Spring meeting,* Mar. 2020.

2. T. V. Mai, Y. Suzuki, S. Suzuki, and Masahiro Asada, "Frequency increase of up to 673 GHz in structure-simplified RTD oscillators with small mesa," *10p-Z24-13, the 81st JSAP Autumn meeting*, Sep. 2020.

3. T. V. Mai, Y. Suzuki, X. Yu, S. Suzuki, and Masahiro Asada, "High output powers of structure-simplified RTD oscillators with offset-fed slot and coplanar stripline antennas," *13p-N105-2, the 82nd JSAP Autumn meeting*, Sep. 2021.

4. T. V. Mai, Y. Suzuki, T. Namba, S. Suzuki, and Masahiro Asada, "Oscillation frequency increase in structure-simplified RTD oscillator with array configuration," *21p-A201-1, the 83rd JSAP Autumn meeting*, Sep. 2022.

■ **Awards:** Student Best Presentation Award.

T. V. Mai, T. Namba, Y. Suzuki, S. Suzuki, and M. Asada, "Array Configuration for High Output Power in Structure-simplified Resonant-Tunneling-Diode Terahertz Oscillator," *the 3rd International Symposium on Frontiers in THz technology*, Fukui, Japan, Nov. 2022.